

**MORPHODYNAMICS OF THE ANABRANCHING
STRUCTURES ON THE UPPER AMAZON RIVER
BASIN**

by

Christian E. Frias

BSc, National University of Engineering, Peru, 2003

MSc, University of Pittsburgh, USA, 2012

Submitted to the Graduate Faculty of
the Swanson School of Engineering in partial fulfillment
of the requirements for the degree of

Doctor of Philosophy

University of Pittsburgh

2013

UNIVERSITY OF PITTSBURGH
SWANSON SCHOOL OF ENGINEERING

This dissertation was presented

by

Christian E. Frias

It was defended on

November 25, 2013

and approved by

Jorge Abad, PhD, Assistant Professor, Department of Civil and Environmental Engineering

Xu Liang, PhD, Professor, Department of Civil and Environmental Engineering

Daniel Budny, PhD, Associate Professor, Department of Civil and Environmental
Engineering

Daniel Bain, PhD, Assistant Professor, Department of Geology and Planetary Science

Eddy Langendoen, PhD, National Sedimentation Laboratory, USDA

Dissertation Director: Jorge Abad, PhD, Assistant Professor, Department of Civil and
Environmental Engineering

MORPHODYNAMICS OF THE ANABRANCHING STRUCTURES ON THE UPPER AMAZON RIVER BASIN

Christian E. Frias, PhD

University of Pittsburgh, 2013

Recent research in numerical modeling of large rivers has focused in reproducing typical morphodynamic planform shapes. One of the typical planform shapes of large river systems is the anabranching structure, which is characterized by a main channel and several secondary channels. Although current models reproduce planform shapes very realistically, there is still a lack of data to validate such models and therefore any outcome from these predictions are questionable. To overcome this issue, an analysis of the morphodynamics on large river systems at different scales is carried out. This research will provide a better understanding of the processes involved in anabranching planforms that could be used to improve prediction of morphodynamic features by using high-resolution mathematical models. First, the effect of the main channel sinuosity in an anabranching planforms at two selected locations in the Amazon River at Peru is assessed with field measurements, numerical modeling and satellite imagery characterization. Next, a three dimensional hydrodynamic model for a bend of the Wabash River (at the Stateline between Indiana and Illinois) is carried out to study the modulation of the bank shear stresses due to the presence of bed forms. Lastly, a three dimensional model to study the turbulence of the bed amalgamation process is performed. From the analysis of the two locations along the Amazon River, it was confirmed that in a medium to high sinuosity stage, the secondary channels behave as non-developed meanders. Also, it was concluded that in all sinuosity stages, the planforms of the secondary channels are controlled by the main channel migration. On the other hand, the model of the Wabash River confirmed that the bank shear stress is greater when bed forms are present. Finally,

the modeling of the amalgamation processes showed that there was a region of high shear stresses associated to turbulence production, in which the streamwise velocity fluctuations were associated to the modification of the bed morphology. Also, the Turbulence Horseshoes Vortices (THV) were more frequent at the beginning of the amalgamation process while the frequency of bursting events was highest when the amalgamation process is at the middle stage.

TABLE OF CONTENTS

PREFACE	xv
1.0 INTRODUCTION	1
2.0 DYNAMICS OF THE ANABRANCHING STRUCTURES	6
2.1 Field Site and Data Collection	10
2.1.1 Low sinuosity stage field data (LS)	10
2.1.2 Medium and high sinuosity stage field data (MS)	12
2.1.3 Digital Elevation Model for LS and MS	14
2.2 The Two-dimensional Shallow Water Model	14
2.2.1 Overview	14
2.2.2 Boundary Conditions	18
2.2.3 Model Calibration	18
2.2.4 Numerical Model Results	19
2.2.5 Satellite Imagery for LS and MS sites	25
2.2.5.1 Site LS (Ronda, Santa Rosa and Chinera Islands - low sinuosity stage)	26
2.2.5.2 Site MS (Muyuy and Panguana Islands)	26
2.3 Metrics analysis	29
2.3.1 Low sinuosity (LS) metrics	30
2.3.2 Medium and high sinuosity (MS) stage metrics	31
2.4 Dynamics of Anabranching Structures Conclusions	31
3.0 MODULATION OF THE FLOW STRUCTURE IN MEANDERING RIVERS DUE TO BED FORMS	36

3.1	Study Site and Field Data	38
3.2	Numerical Model and Computational Setup	41
3.2.1	Governing Equations	42
3.2.2	Mesh Generation, Initial and Boundary Conditions	43
3.2.2.1	Case C-1: with bed forms	43
3.2.2.2	Case C-2: without bed forms	44
3.2.2.3	Mesh construction for C-1 and C-2	44
3.2.2.4	Initial and Boundary conditions for C-1 and C-2	45
3.2.3	Validation	46
3.3	Results	47
3.3.1	Shear Stress Characterization	47
3.3.2	Flow Characterization	49
3.4	Bank Shear Stress Due To Bed Forms Conclusions and Future Work	53
4.0	HIGH RESOLUTION ANALYSIS OF THE FLOW STRUCTURE MOD- ■	
	ULATION DUE TO BED FORMS	65
4.1	Methodology	67
4.1.1	Hydrodynamic Governing Equations	67
4.1.1.1	Dynamic Smagorinsky model	68
4.1.2	Computational Setup	69
4.1.3	Boundary and Initial Conditions	71
4.2	Results, Analysis and Discussion	72
4.2.1	Validation of the LES modeling	72
4.2.2	Flow field structure	73
4.2.3	Interaction ripple-dune structure and turbulence	77
4.2.4	Interaction bed form and water surface elevation	81
4.2.5	Shear stress, bed sediment transport and bursting events	81
4.3	High Resolution Model of Bed Forms Amalgamation Process Conclusions	88
5.0	GENERAL CONCLUSIONS AND FUTURE WORK	92
	APPENDIX A. MADEIRA RIVER FIELD THREE DIMENSIONAL MODEL. ■	
	FIELD CAMPAIGN REPORT.	97

A.1	Objective	97
A.2	Introduction	97
A.3	Field Campaign	98
A.4	Conclusions and Future Work	106
APPENDIX B. ANABRANCHING FLUME. CONSTRUCTION PROGRESS		
	REPORT	109
B.1	Objective	109
B.2	Introduction	109
B.3	Head and Tail Tank Construction	110
B.4	Piping System	110
B.5	Flume Body Construction and Planform Design	113
B.6	Bed morphology measurement	119
B.7	Conclusions and Future Work	119
APPENDIX C. PLANFORM DYNAMICS OF AN ANABRANCHING		
STRUCTURE NEAR IQUITOS. IMPLICATIONS ON THE LARGEST		
CITY IN THE PERUVIAN AMAZON RAINFOREST.		
		122
C.1	Introduction	122
C.2	Site Description	124
C.3	Historical Analysis	125
	C.3.1 Planform evolution stages	125
	C.3.1.1 Anabranh IS-A0	129
	C.3.1.2 Anabranh IS-A1	129
	C.3.1.3 Anabranh IS-A2	130
	C.3.1.4 Anabranh IS-A3	130
	C.3.1.5 Anabranh IS-A4	131
	C.3.2 Planform evolution and migration	131
	C.3.3 Variation of water surface elevations	137
	C.3.4 Field Measurements and Two-dimensional Shallow Water Model	143
C.4	Discussion	149
C.5	Conclusions	152

APPENDIX D. CHRISTIAN FRIAS BIO	155
D.1 Research Experience	155
D.2 Academic Training	155
D.3 Awards	156
D.4 Teaching Experience	156
D.5 Mentoring Experience	156
D.6 Research and Teaching Interests	157
D.7 Published/In Review/ In submission/ In preparation Journal Articles . .	157
D.8 Conference Proceedings	158
D.9 Abstracts/Talks/Posters	160
D.10 Technical Reports	160
D.11 Professional Society Memberships	161
D.12 Professional Service: Conferences	161
D.13 Professional Service: Website Administrator	161
BIBLIOGRAPHY	162

LIST OF TABLES

2.1	LS velocity transects.	12
2.2	MS velocity transects.	13
3.1	Maier bend velocity transects.	40
3.2	Gaging station water surface elevations used to calculate the bed elevation.	40
4.1	Logarithmic inlet profile parameters.	71
C1	Dates for migration analyses, with the period in days between Landsat images processed and water elevation on the river.	134
C2	Water surface elevations in Iquitos after June, 2011 for Landsat images available until September, 2012	150

LIST OF FIGURES

2.1	LS and MS site map.	11
2.2	Digital Elevation Model (DEM) map for the Upper Amazon River Basin valley.	15
2.3	LS and MS bathymetry.	17
2.4	Site LS. Comparison of modeled and measured velocities for transects 1, 3 and 5. Notice the consistently underpredicted low velocities and overpredicted high velocities. These behavior could be due to the speed of the boat as long as it measured the transect. The boat hast to travel slower for low velocities and faster at high velocities causing a bias on the real value of the velocities magnitude.	20
2.5	Site MS. Comparison of modeled and measured velocities for low-flow (muy1, muy2 and pan30) and high-flow (muy2, muy3 and muy23) conditions.	21
2.6	LS site. Contours of bed shear stress and velocity vectors colored by velocity magnitude (panels 1-6).	23
2.7	MS site. Contours of bed shear stress and velocity vectors colored by velocity magnitude (panels 1-6).	24
2.8	Site LS (low sinuosity stage) multitemporal Landsat images.	27
2.9	Site MS (medium and high sinuosity stage) multitemporal Landsat images.	28
2.10	LS satellite image analysis.	32
2.11	MS satellite image analysis.	33
3.1	Site Map for Wabash River Study.	38
3.2	LIDAR survey of the bank and MBES survey of the bed for Maier bend.	52

3.3	Discrimination procedure for a bed profile. (a) Shows the location of the profile processed on (b). λ_{R-1} is the wavelength for the bed forms found in R-1 and λ_{R-2} is the wavelength for the bed forms found in R-2. η , $\eta_{1,3}$, $\eta_{2,3}$ and $\eta_{3,3}$ are the amplitudes for the original, the small bed forms, the large bed forms and the bar signals respectively.	55
3.4	Wabash River Mesh Construction Procedure.	56
3.5	Wabash River comparison of the aDcp and modeled velocity magnitude.	57
3.6	C-1 and C-2 bed morphology and velocity transects for secondary flow analysis.	58
3.7	Contours of shear stress in Pa of case C-1 (case with bed forms).	59
3.8	Contours of shear stress in Pa of case C-2 (case without bed forms).	60
3.9	Comparison between the bank shear stress of case C-1 and case C-2.	61
3.10	Velocity magnitude contours and vectors for C-1 and C-2.	62
3.11	Streamlines for case C-1.	63
3.12	Streamlines for case C-2.	64
4.1	Computational grid for RUN II.	70
4.2	Average streamwise velocity \bar{u} (m/s) for the three cases.	73
4.3	Experimental and numerical results for the average streamwise velocity (m/s) for selected cross sections in RUN II.	74
4.4	Experimental and numerical results for the Reynolds stresses $\langle u'v' \rangle$ (m^2/s^2) for selected cross sections in RUN II.	75
4.5	Average flow streamlines colored by average velocity magnitude (m/s) for a) RUN I b) RUN II and c) RUN III.	76
4.6	Swirling strength isosurfaces with elevation contours (mm) for a) RUN I, b) RUN II and c) RUN III.	78
4.7	Swirling strength isosurfaces with velocity contours (m/s) for a) RUN I, b) RUN II and c) RUN III.	79
4.8	Spanwise velocity fluctuations contours for a plane located at $y = 0$ a) RUN I b) RUN II and c) RUN III.	82

4.9	Instantaneous water surface at selected time steps for a) RUN I b) RUN II and c) RUN III. The upwelling structures on the water surface are denoted as UW1-1, UW2-1 and UW3-1 for RUN I, RUN II and RUN III respectively. The downwelling structures on the water surface are denoted as DW1-1, DW2-1 and DW3-1 for RUN I, RUN II and RUN III respectively.	83
4.10	Bed shear stress contours for a) RUN I b) RUN II and c) RUN III.	85
4.11	Streamwise velocity fluctuations contours (m/s) for a plane parallel to the bed at $z^+ = 2$ for a) RUN I b) RUN II and c) RUN III.	86
4.12	Burst frequency for a) RUN I b) RUN II and c) RUN III. Where ΔT is the duration of a single event, $\langle \Delta T \rangle$ is the average event duration for each case, T_e is the time between single events and $\langle T_e \rangle$ is the average time between events for each case.	90
4.13	Instantaneous streamwise velocity contours and instantaneous velocity vectors for different times.	91
A1	Furuno Echosounder.	99
A2	Teledyne Workhorse Monitor aDcp.	99
A3	Madeira River Study Site Map.	100
A4	FS 2012 Bathymetry	101
A5	SS Site 2012 Bathymetry	102
A6	TS Site 2012 Bathymetry	103
A7	FS Site aDcp transects	104
A8	SS Site aDcp transects	104
A9	Bed sediment sampling	105
A10	GPS points used to compute the water surface slope	105
A11	SS Site 2013 Bahymetry.	107
B1	Anabranching structure selected for the experimental flume planform.	111
B2	Head and Tail tanks	112
B3	Piping System	113
B4	Flume body construction procedure	115
B5	Actual layout of the Anabranching Flume	116

B6	CAD drawing with the coordinates of the main channel.	117
B7	Sediment control structures	118
B8	Methodology used to measure the bed morphology	120
C1	Left: Digital Elevation model in the surroundings of Iquitos anabranching structure. The Digital Elevation Model data was downloaded from Jet Propulsion Laboratory website. Right: Iquitos anabranching structure, located at geographical: Latitude $3^{\circ}42'S$, Longitude $73^{\circ}9'W$. Landsat image taken on June, 2011 (courtesy of USGS). Flow is from south to north.	126
C2	Planform evolution of Iquitos anabranching structure. Image at left top is the form of the anabranching in 1980 and the Image at right bottom in 2012. Intermediate images show the planform evolution on intervals of 5 years, dark blue are areas of permanent water during the analyzed period, light blue areas are erosion zones and grey areas represent deposition zones.	127
C3	More detailed migration for the period 1995 through 2005. Dark blue represents zones of permanent water, light blue are zones of erosion, and gray are zones of deposition.	128
C4	Migration rate is obtained by calculating the displacement of nodes from one centerline to its next stage in time. The analysis was performed using the NCED Stream Restoration Toolbox [119]	132
C5	Historical evolution of channel width and sinuosity of the anabranches. Upper chart shows the water surface level in the river during the date of the Landsat utilized for the analysis. These measurements are at the Iquitos station. . . .	135
C6	Channel width versus sinuosity observed in Iquitos Anabranching structure. .	137
C7	Histogram of daily historical water surface elevations recorded in Iquitos Hydrological station. Lower chart shows the minimum and maximum levels recorded per year.	138
C8	Migration computed with displacements of centerlines. AM: averaged migration, AMR: averaged migration rate, NAM: normalized migration rate	140

C9	Correlation of average migration (AM) and normalized average migration (NAM) versus channel width (Width), sinuosity (Sinuo), average elevation (AveLev), standard deviation of daily water level variation (StdLev), minimum water level (MnLev), maximum water level (MxLev), maximum water level variation in the period (MxVar), all computed with the daily water level recorded between the dates of the two Landsat images utilized for computing the migration.	141
C10	Correlation, R , for migration versus maximum water level variation (DE) negative and positive computed for different intervals of time, in the plots AM stands for average migration and NAM for normalized average migration. . .	142
C11	A. Histogram of water level variation (DE) in periods of 60 days. B. Maximum negative variation on water level observed (recession) per year. C. Maximum water level increase observed per year.	144
C12	Transversal sections for velocity profiles and bathymetry collected during June 2011	145
C13	Comparison of velocities measured versus modeled for some of the sections shown in Figure C12. In the left plots show the modeled and measured velocity field and in the right the comparison of velocity magnitude.	147
C14	Planform migration compared with the hydrodynamics. A. Migration of anabranch IS-A4 since the initial condition on 2011. B. Velocities computed with Telemac-2D with the hydraulic conditions on June, 2011. C. Computed shear stress in the bed. D. Computed water depth.	148
C15	Migration from 2011 through 2012 and variation water levels. Images show the areas of bed exposed during dry season and the areas flooded and eroded during wet season.	150

PREFACE

This thesis is dedicated to my wife Linda and my parents.

“Science never solves a problem without creating ten more.”

-George Bernard Shaw

Acknowledgments

I would like to express my deep gratitude to my advisor, Assist. Prof. Jorge D. Abad (University of Pittsburgh), for his continuous guidance, support, and encouragement throughout my graduate studies.

I also wish to thank Alejandro Mendoza (Post-Doctoral Research Associate, University of Pittsburgh), Cesar Simon (Graduate Research Assistant, University of Pittsburgh), Kristin Dauer (Graduate Research Assistant, University of Pittsburgh), Ross Volkwein (former Graduate Research Assistant, University of Pittsburgh), Dr. Eddy J. Langendoen (U.S. Department of Agriculture, Agricultural Research Service, National Sedimentation Laboratory), Commander Hugo Montoro (Head of the Hydrographic Service, Peruvian Amazonian Basin) for contributing to this effort in different ways and the committee members Dr. Xu Liang, Dr. Daniel Budny and Dr. Daniel Bain.

1.0 INTRODUCTION

Over the last decade several researchers have focused on studying the fluvial geomorphology of the rivers in the Amazon rainforest watershed such as the Madeira River, Parana River, Orinoco River, Ucayali River and the Amazon River, the largest river on Earth. The Amazon River can be classified as a “mega river” [118], with a typical anabranching planform. Most research on multichannel networks has focused on braided rivers. Including, experimental work in flumes [16, 17] and numerical modeling of braided rivers [100, 134, 171]. These two approaches (experiments and numerical modeling) give a good insight into processes involved in multichannel river networks. In the following paragraphs a brief summary of the state-of-the-art for numerical modeling of multichannel river networks is presented.

According to [100], “due to the nature of braided rivers, models of such rivers need to be two-dimensional in some sense.” However, one dimensional stochastic models such as markov chain models or random walk models can be found in literature [94, 112, 146], in which the braiding processes are generated randomly. On the other hand, the braiding processes have been related to other physical phenomena. In this regard, a characteristic cascade from bed forms, bars and islands has been observed in braiding processes similar to what is observed in turbulence eddies cascades. This characteristic cascade motivated [143] to describe a width-averaged model for braiding. In this model a turbulence analogy is used to explain the braiding processes. For example, he relates confluences as the braiding equivalent of sweeps and ejections in turbulence. Although this study cannot predict a braiding river planform, it was concluded that the smallest scales will influence planform changes in the long run. Some other approaches that can be used to study the braiding processes are the use of satellite images or aerial photography to create an autoregressive time series model, two dimensional numerical models, and lattice gas models. From these three models, according to [100], “it

is expected that although lattice gas methods, just like other cellular models, are valuable research tools for the detailed and/or fundamental, process-oriented studies they will not be applied to large scale morphological modelling of rivers in the foreseeable future.”

The nature of the braiding process is two-dimensional. Some recent studies have used two-dimensional models to simulate the process, including the neural network model, the cellular model, the branches model and the two-dimensional hydrodynamics models with bed and bank migration. First, some examples of neural network usage can be found for character recognition in [91] and for braided river planform prediction in [100]. The neural network methodology learns from satellite images or aerial photos how to predict where a dry or wet pixel will be located after one year. Each pixel is considered as an input-output neural network structure. The inputs should be related to the geometrical location of the branches. [100] used five input parameters measured from each pixel. These inputs were: 1) distance to the nearest channel; 2) sine and cosine of the angle between the direction to the nearest channel and the flood flow direction; 3) the local width of the nearest channel; and 3) the fraction of the pixel that is covered by water. The major limitations in the use of the neural network for multichannel river networks are: 1) the large amount of data that is needed to train the network; and (most important) 2) the model is not based on the physical principles governing hydrodynamics and morphology. Next, cellular models or reduced complexity models have been used by [134, 171, 140]. According to [100] in these models “the cells of a lattice interact according to local rules based on abstractions of physical relations describing a dynamic system.” One of the limitations of these models according to [100] is the fact that due to the hydrodynamics simplification, water cannot follow a channel at an angle larger than 45 degrees. Also, in [134]’s model, the water can flow uphill which, at large scale, is clearly unrealistic. Moreover, [140] observed “the existence of localized flow accelerations in shallow flow depths in the reduced complexity model output, reflecting the simple model process equations and neglect of momentum conservation.” Next, [100] developed an innovative model called branches model. The purpose was to have a tool to simulate the formation of braided rivers in less than a fully 2D numerical model would take. In short, the model is based on a representation of the braided river as a network of channels. In software development terms, this model can be referred to an object-oriented model: the

whole river is subdivided into more or less identical, relatively simple objects, namely the channels. Each individual channel can change its width, form mid-channel bars, migrate, or be abandoned. Although [100] claims the branches model includes physical knowledge, it is used only for the lateral migration of the channels. All the other parameters are modeled in a stochastic way, such as the width adjustment and branch abandonment. However, the great advantage of the cellular model and the branches model is the faster computing speed in comparison to a two-dimensional hydrodynamics and morphodynamics model.

Next, software such as MIKE21 C and HSTAR (Hydrodynamics and Sediment Transport in Alluvial Rivers) developed by [49] and [139] respectively have been used to simulate braided and anabranching river systems. The software use shallow water equations, the exner equation and sediment transport equations to simulate the temporal dynamics of the river bed. MIKE21 C model has been used in the Jamuna River [49] resulting in a good approximation of the river planform after 30 years of simulation period. The initial condition for this simulation was a completely uniform river bed with constant slope, discharge, grain size, width, depth and bed resistance. Although the model was able to capture some of the planform characteristics (wave length, braiding intensity, channel width, shape and size of the main bars), this cannot be considered a validation per se, since it lacks validation for hydrodynamics parameters such as velocity and water depth. Moreover, according to [49] “accurate long-term predictions of the morphology of braided rivers cannot be achieved with any model due to the inherent chaotic nature of such rivers”.

Regarding the model HSTAR, in summary, it “solves the depth-averaged shallow-water equations on a grid of cells representing the channel and floodplain surface. Two sediment fractions are represented (silt and sand). The effects of secondary circulation and the gravitational deflection of sediment in the direction of the local bed slope are included in the model. Active channel cells are converted to vegetated floodplain cells when the depth of inundation experienced over a specified time period (T_{veg}) does not exceed a threshold depth (H_{cr}). Bank erosion converts floodplain cells to active channel. ” [140]. Although the model simulates important physics of the multichannel river networks, it cannot be concluded that it is validated per se. Again, the lack of input parameters and standardize metrics for the river systems to which the model is compared against are not available. Moreover, [139]

concludes, “Given the lack of previous research into physics-based morphodynamic modeling of large rivers over centennial time-scales, the current study represents a first attempt to assess if such modeling is feasible, and whether it can contribute to understanding of bar and island morphodynamics. Comparisons between modeled and natural channels are promising, in terms of distributions of channel width and depth, bar and island morphology, and mechanisms and styles of channel evolution. However, much remains to be done to evaluate and improve models of large river evolution.”

As shown above, there are still several issues to address in numerical modeling of multi-channel river networks and therefore in the applicability of the current models in the Amazon River, most of which are related to the computing speed and the validation and calibration of the models. The first issue, computing speed, can be solved by using parallelized two dimensional hydrodynamics model such as TELEMAC2D [55]. For example, TELEMAC2D has been used in a numerical mesh of 200 million cells of the Gironde Estuary in Western Europe. This model was carried out on up to 32,768 cores [133]. The second issue, validation and calibration of the models, can be solved by obtaining metrics such as bifurcation angles, sinuosity, channel width, floodplain shape, soil materials, hydrographs and correlations between number of islands, channels and migration. Also, temporal and spatial distributed data for velocities and water depths will be needed to validate the hydrodynamics. Previous studies in which metrics of the Amazon River have been obtained are [172, 111, 126, 127, 128, 129]. All of these studies were carried out for the Brazilian part of the Amazon River and not for the complete Upper Basin of the Amazon River. On the other hand, countries such as Peru, Brazil and Colombia have carried out field campaigns to survey bathymetry, flow rate and velocities in several rivers in the Amazon River Basin as part of the data needed to design their fluvial nautical charts.

In anabranching river systems the planform presents a main channel and some secondary channels. The mechanisms that are involved in the creation of this pattern remain a research challenge, and therefore numerical models that attempt to replicate it lack a theoretical morphodynamics basis. Much of the research that attempts to explain the anabranching pattern formation is based on satellite imagery alone. To extend the current research, a study for a planform scale, channel scale and bed form scale is presented herein. The study

starts at the planform scale by analyzing the dynamics of main and secondary channels from satellite imagery, two dimensional numerical modeling and field data in Chapter 2. For that, two anabranching structures with different main channel sinuosities were selected in the Upper Amazon River Basin. Next, at the channel scale, a meander bend in the Wabash River (Stateline between Illinois and Indiana, USA), whose size is at the same scale as a secondary channel in an anabranching structure was selected in Chapter 3. Although this study is not located in the Amazon River Basin, it allowed us to develop the methodology to be used for secondary channels of an anabranching pattern of the Upper Amazon River. On this bend, the modulation of the bank shear stress due to bed forms presence was assessed. Finally, at the bed forms scale, the amalgamation process of a train of ripples to a dune size bed form was studied by means of a Large Eddy Simulation (LES) in Chapter 4. In such a way, the dynamics of an anabranching structure can be studied from similarities found in bed forms amalgamation and bank migration due to bed forms, resulting in the characterization of planform dynamics due to bank migration and bed morphology. Conclusions of this process are drawn in Chapter 5.

2.0 DYNAMICS OF THE ANABRANCHING STRUCTURES

A recent topic in river geomorphology is the concept of the anabranching pattern developed in mega-rivers such as the Amazon River, Parana River or Mississippi River [118]. These “mega-rivers” have a mean annual discharge greater than 17,000 cms, very low slopes and fine sandy sediment bed load [118]. Currently is still needed to characterize for large rivers the interaction of the parameters studied for small rivers such as hydrodynamics and sediment transport. According to [118] it has not been possible to “scale up” experimental results obtained from flumes to “mega-rivers”. However, an effort to study the anabranching configuration of the Magela Creek in Australia is found in [103]. Therefore, there is an existing need to use other methods for this purpose. [95] proposed a quantitative theoretical analysis that related the number of channels and bed load transport to explain the formation dynamics of an anabranching river. On the other hand, [103, 135] associated the maximum flow efficiency with the anabranching planform. A promising methodology to explain the formation dynamics of an anabranching river is to develop numerical models that could be applied to the mega-rivers scale. On this regard, an effort to validate different types of numerical models on a mega-river scale was carried out by [140]. On that study, a three dimensional model a shallow water model and a reduced complexity (RC) model was used. From those three models the novel one was the RC model which delivered a fast method (four times faster than a shallow water two dimensional model) to determine velocities in a very large scale. However, the RC model neglects all the momentum equations to achieve such efficiency. Although the purpose of that study was to demonstrate the validity of the RC model to predict velocities, there were also pointed limitations such as the lack of localized flow accelerations. This limitation could prevent the use of the RC model to study hydrodynamics in a anabranching fluvial system such as the effect of the velocity gradients

and shear stresses in branches formation. On the other hand, considering the computational efficiency and validity of the results, the second best option to the RC model is a shallow water two dimensional model.

There are existing hypothesis concerning to the formation of anabranching fluvial systems. It can be mentioned the consideration of [105] that this type of rivers are a result of avulsion. According to his hypothesis the lateral displacement due to bank erosion is small compared to the bed deformation due to bed load deposition. To quantify the existence of an anabranching river [105] uses a parameter called mobility number. This number relates the lateral migration with the aggradation. According to this number the anabranching pattern is presented in cases where the mobility number is much less than one. The latter means that anabranching rivers will be presented in environments undergoing bed aggradation rates that are rapid compared to lateral cutting rates [105]. Prediction of aggradation and bank erosion rates is an ongoing research topic in river morphodynamics. Aggradation and avulsion has been studied in the past by [167, 101, 169]. [169] carried out a numerical model able to transport water and sediment to explain the dynamics of an anabranching fluvial system formation. One of his most important conclusion is that the increase of sediment supply leads to aggradation which increases the braid intensity and a small increment of the channel width [169]. The process of aggradation is related to the maturity stage of an anabranch or branch. The maturity of an anabranch is achieved when a low depth-width ratio and gentle gradient is presented [101]. Consequently, since the reach losses sediment transport capacity an avulsion process happens creating another branch and abandoning the old one [101]. However, this field is still under research and there is almost no investigation to relate the bed load migration and lateral migration in anabranching “mega rivers as well as the effect of the main channel planform configuration on the secondary channels. The largest river classified as a “mega river” is the Amazon River. The entire Amazon River Basin has an average discharge of $209,000 \text{ m}^3/\text{s}$, a drainage area of $6100 \times 10^3 \text{ km}^2$ and a sediment yield of $167 \text{ tn}/\text{km}^2/\text{year}$ [118]. This river as well as the other large rivers on the Amazonian river Basin are not highly disturbed by human activities [2]. For this reason the Amazonian region is one of the richest region in fauna and flora [150, 168, 30, 82]. Moreover, it presents a unique planform configuration that has not been studied in depth. The fact

that it behaves as a anabranching river system, as stated above, increase the complexity of the morphodynamics of such river in comparison to the well studied meandering riverine systems.

It has been noticed that the islands formed in the Amazon River remains in place which differs from other anabranching planforms [2]. As explained above, it was concluded from previous research that on a anabranching structure the islands undergo a creation and destruction process according to the avulsion process. In contrast, a recent study from [19] concludes that the anabranching pattern is achieved by different processes and thus it cannot be related only to avulsion processes. In fact, that is the case of the Amazon River where the secondary branches does not show an avulsion process tendency as will be shown herein. On the contrary, the processes that can be identified from satellite imagery are chute cutoffs after a channel migration and mid-channel bar formation after a channel width adjustment. These processes have been observed experimentally by [16]. The purpose of this study was to explain how gravel-bed rivers braid by studying the sedimentation processes (scour and deposition). Although the rivers studied were gravel-bed rivers the material used for the experiments was sand and the processes described from experimental observation are very similar to the ones observed in the Amazon River.

Because of the large time and spatial scale of the Amazon River the secondary anabranches follow their own planforms. As will be explained herein they resemble a meandering migration pattern between islands. Therefore the secondary branches of the Amazon River show patterns of meander growth and shift such as extension, translation, rotation, conversion to a compound meander, neck cutoff and chute cutoffs as explained by [158] for meandering streams. Thus, this river can be classified as a mixed-load, laterally active anabranching river according to [135]. This configuration is possible when the banks are cohesive and can resist increased stress [135]. The latter can be enhanced with the presence of vegetation on the islands that grows after a drought event. A study that characterizes the influence of the vegetation in the anabranching fluvial system is the one carried out by [104]. On that study it was conclude that the presence of vegetation is strongly related to the stability of the anabranches on the Magela Creek, Australia.

On the other hand, [127] carried out an study to relate channel features of the Amazon River such as main channel sinuosity, main channel width, main channel bank height and floodplain features such as floodplain width and islands and lakes area with the tectonics of the floodplain. For this study a temporal analysis of 9 years (1971 to 1980) was performed and a spatial analysis of the Amazon River valley for the Brazilian region. Some important observations are the high correlation between sinuosity and floodplain width along the Amazon River valley and the change of size and distribution of the lakes and scroll bars valley crosses the geological structural arches. Later [126] extends her research by adding the effect of climate change and sea level to the floodplain planform. One of the main observations of this study is the effect of the tectonics on the water surface gradient with a greater gradient upstream structural arc Purus (near Manaus). Nevertheless these studies aided to give a better insight on the morphodynamics processes involved in the Amazon River do not explain the morphodynamics of each particular anabranching structure in the Amazon River. Moreover, the temporal analysis is less than 10 years and then the results cannot be used for engineering time scales (i.e 50 to 100 years) [131].

Although there are several researchers that tried to explain the dynamics of the Amazon River in the Brazilian region [172, 70, 128, 10, 127, 164, 53, 126] there is a lack of research on this regard for the Peruvian region where the Upper Basin of the Amazon River is located. One of the interesting, and not well studied, parameter of the anabranching fluvial systems in this region is the sinuosity of the main and secondary anabranches. According to [2] the sinuosity of the main anabranches can be classified as low, medium and high sinuosity. The sinuosity of these main anabranches change as long as them migrate. Also the main anabranch can convert to a secondary anabranch or viceversa if the discharge through it increases or decreases. There is very little research regarding to this characteristic among others in the upper Basin region. Hence, this work presents an analysis of the behavior of the secondary anabranches for medium and low sinuosity by means of a two dimensional numerical model and historical imagery data. For this purpose two anabranching structures called MS, near Iquitos, Peru and LS at the triple frontier Peru-Colombia-Brazil on the Amazon River were selected as cases of medium and low sinuosity respectively. The different sinuosities represent different stages of anabranching development in the upper Basin of the

Amazon River. Field data collection on these locations is presented in section 2.1. Next, parameters such as braid-channel ratio [74], secondary-main channel width ratio, secondary-main channel length ratio and secondary-main channel sinuosity are calculated in section 2.3. The results from a two dimensional shallow water numerical model is presented in section 2.2.4. Finally the results and discussion of the implications of the sinuosity on the anabranches of the Amazon river are given on sections 2.3 and 2.4 respectively.

2.1 FIELD SITE AND DATA COLLECTION

2.1.1 Low sinuosity stage field data (LS)

To study a low sinuosity stage anabranching structure, a site located at the boundary between Peru, Colombia and Brazil was selected (see Figure 2.1 (a)). This study site is denoted as LS. The largest city in this site is Leticia, Colombia followed by Tabatinga, Brazil and Santa Rosa, Peru. By 2012, the site presented a main anabranch referred as LS-A0 and three secondary anabranches that start from the main anabranch referred as LS-A1, LS-A2 and LS-A3 (see Figure 2.1 (a)). The main islands in this structure are denoted as LS-I1, LS-I2, LS-I3 and LS-I4 (see Figure 2.1 (a)). Islands LS-I2, LS-I3 and LS-I4 are also known by the names Ronda, Santa Rosa and Chineria, respectively. As it can be seen in Figure 2.1 (a), Leticia, Tabatinga and Santa Rosa towns are located along the banks of the secondary anabranch LS-A2. The city of Leticia has an important harbor for the region and is highly dependent on the water level of this anabranch. For this location, bathymetry and velocity measurements were carried out on December of 2011 (wet season). The bathymetry (cross sections spacing 200m) was collected using a single beam echosounder SyQwest Batty 500 controlled by the Hypack Software [51]. Real time positions were obtained by using a Fugro SeaStart DGPS. This instrument measures the water depth surface for the site, however, numerical modeling requires bed elevation. To obtain the bed elevation for each bathymetry cross section the water surface levels at the gaging stations shown in Figure 2.1 (a) were used. Using these water levels a water surface was obtained and the bed elevation for all the



Figure 2.1: a) LS site map (image from September 2011). The red line represents the triple boundary between Brazil, Colombia and Peru. The yellow dashed lines are velocity measurements. The water flows from north to south b) MS site map (image from October 2010). The yellow dashed lines are velocity measurements and the yellow points stage measurement points. The water flows from south to north. Images are courtesy of USGS.

Table 2.1: LS site (at Peru-Colombia-Brazil boundary) velocity transects. Where τ_b is the shear stress, \bar{U} is the mean average velocity for each transect, C_f is the friction coefficient and k_s is the roughness height.

Transect Name	Area [m ²]	Width [m]	Water Depth [m]	τ_b [Pa]	\bar{U} [m/s]	C_f	k_s [m]	branch type	date
2	23335	1114	20.9	10.92	1.217	0.0074	1.94	main	12/13/2011
3	6731	548	12.3	6.40	1.045	0.0059	0.64	secondary	12/13/2011
4	21528	1632	13.2	6.87	1.369	0.0037	0.17	main	12/13/2011
5	22070	1562	14.1	7.36	1.297	0.0044	0.32	main	12/13/2011
6	22092	2015	11.0	5.71	1.334	0.0032	0.09	main	12/13/2011
7	29767	2237	13.3	6.94	1.139	0.0053	0.54	main	12/13/2011
8	23620	1296	18.2	9.50	1.416	0.0047	0.52	main	12/13/2011
9	3974	327	12.2	6.34	1.104	0.0052	0.45	secondary	12/13/2011
10	3383	760	4.5	2.32	0.719	0.0045	0.11	secondary	12/13/2011
11	5309	613	8.7	4.51	1.073	0.0039	0.14	secondary	12/13/2011

bathymetry points was calculated by simple subtraction. On the other hand, the velocity measurements were collected using an acoustic Doppler current profiler (aDcp) Workhorse Rio Grande 600 Khz RD Instruments. In total, 10 velocity cross sections were surveyed (at least two passes per cross section) as shown in Figure 2.1 (a) and Table 2.1. All the velocity transects were surveyed in the same day December 13 of 2011. Additionally, a topographic survey was carried out for the left bank of anabranch LS-A2 where cities Leticia and Tabatinga are located (see Figure 2.1 (a)).

2.1.2 Medium and high sinuosity stage field data (MS)

To study a medium to high sinuosity stage anabranching structure, a site located about 20 km upstream of Iquitos, the largest city in the jungle of Peru was selected as shown in Figure 2.1 (b). This site will be denoted as MS. The water levels of the study site were located at a town called Tamshiyacu (see Figure 2.1 (b)). The main anabranch is denoted as MS-A0,

while the secondary anabranches are MS-A1, MS-A2, MS-A3 and MS-A4 (see Figure 2.1 (b)). The main islands have been denoted as MS-I1, MS-I2, MS-I3 and MS-I4 (see Figure 2.1 (b)).

Table 2.2: MS site (near Iquitos, Peru) velocity transects. Where τ_b is the shear stress, \bar{U} is the mean average velocity for each transect, C_f is the friction coefficient and k_s is the roughness height.

Transect Name	Area [m ²]	Width [m]	Water Depth [m]	τ_b [Pa]	\bar{U} [m/s]	C_f	k_s [m]	branch type	date
TAMSHI 06	14003	967	14.5	4.77	0.933	0.0055	0.62745	main	08/19/2010
MUY 01	14488	1347	10.8	3.55	0.862	0.0048	0.31282	main	08/17/2001
MUY 05	13333	2481	5.4	1.77	0.942	0.0020	0.00611	main	08/17/2010
MUY 10	4964	1053	4.7	1.55	1.427	0.0008	0.00002	main	08/18/2010
MUY 15A	4337	876	4.9	1.63	1.059	0.0015	0.00117	main	08/18/2010
MUY 20	5878	661	8.9	2.93	1.068	0.0026	0.03001	main	08/18/2010
PAN 10	1212	276	4.4	1.45	1.206	0.0010	0.00011	secondary	08/17/2010
PAN 15	1379	386	3.6	1.18	1.005	0.0012	0.00024	secondary	08/17/2010
PAN 20	2872	757	3.8	1.25	1.114	0.0010	0.00010	secondary	08/17/2010
PAN 25	1561	304	5.1	1.69	1.489	0.0008	0.00002	secondary	08/18/2010
PAN 30	3042	440	6.9	2.28	1.139	0.0018	0.00429	secondary	08/18/2010
SEC 240	12325	1351	9.1	3.01	1.101	0.0025	0.02671	secondary	08/17/2010

The data was collected on August of 2010 (dry season). A bathymetry survey was carried out with single beam equipment every 100m and velocity measurements were carried out at locations shown in Figure 2.1 (b). Due to the complexity on the planform configuration the slope of the water cannot be assumed as constant for all the anabranches. Due to this fact, it was decided to measure the water surface elevation at 10 locations in the study site (see Figure 2.1 (b)). On each location, a GPS benchmark was surveyed and monumented with concrete slabs. Next, an optical level survey was carried out up to the water surface to obtain the water surface elevation at that location. Finally, the water surface slopes of the branches were obtained as 3.29E-05, 4.37E-05, 4.32E-05 and 5.85E-05 for anabranches MS-A0, MS-A1, MS-A2, and MS-A3, respectively. The velocity measurements were collected

using an acoustic Doppler current profiler (aDcp) [50]. In total, 12 velocity transects were surveyed as shown in Figure 2.1 (b) and Table 2.2. These velocity transects were measured in three days from August 17 to August 19 of 2010.

2.1.3 Digital Elevation Model for LS and MS

A mosaic of a Digital Elevation Model (DEM) from the USGS Shuttle Radar Topography Mission (SRTM) was built. The elevation can be used to define the boundaries of the valley of the Upper Amazon River Basin (from site MS to site LS). Figure 2.2 shows the contours for this DEM from which is depicted that the valley width for site MS ranged from 23 to 24Km (see Figure 2.2 b) and for site LS ranged from 30 to 31Km (see Figure 2.2 c)). Also, the available space for river migration is shown in these figures. Thus, for site MS, the largest available space for river migration is located at the left bank of the main anabranch. Whereas, for site LS the largest available space for migration is located at the right bank of the main anabranch.

2.2 THE TWO-DIMENSIONAL SHALLOW WATER MODEL

2.2.1 Overview

The system of equations encompasses one continuity equation (3.1) and two momentum equations (2.2 and 2.3), thus by solving them, the water depth and the streamwise and spanwise velocity for each node are obtained.

$$\frac{Dh}{Dt} + \frac{\partial(hU)}{\partial x} + \frac{\partial(hV)}{\partial y} = S_h \quad (2.1)$$

$$\frac{\partial(hU)}{\partial t} + U \frac{\partial(hU)}{\partial x} + V \frac{\partial(hU)}{\partial y} = -gh \frac{\partial H}{\partial x} + \frac{\partial}{\partial x} \left(h\nu_t \frac{\partial U}{\partial x} \right) + \frac{\partial}{\partial y} \left(h\nu_t \frac{\partial U}{\partial y} \right) + S_x \quad (2.2)$$

$$\frac{\partial(hV)}{\partial t} + U \frac{\partial(hV)}{\partial x} + V \frac{\partial(hV)}{\partial y} = -gh \frac{\partial H}{\partial x} + \frac{\partial}{\partial x} \left(h\nu_t \frac{\partial V}{\partial x} \right) + \frac{\partial}{\partial y} \left(h\nu_t \frac{\partial V}{\partial y} \right) + S_y \quad (2.3)$$

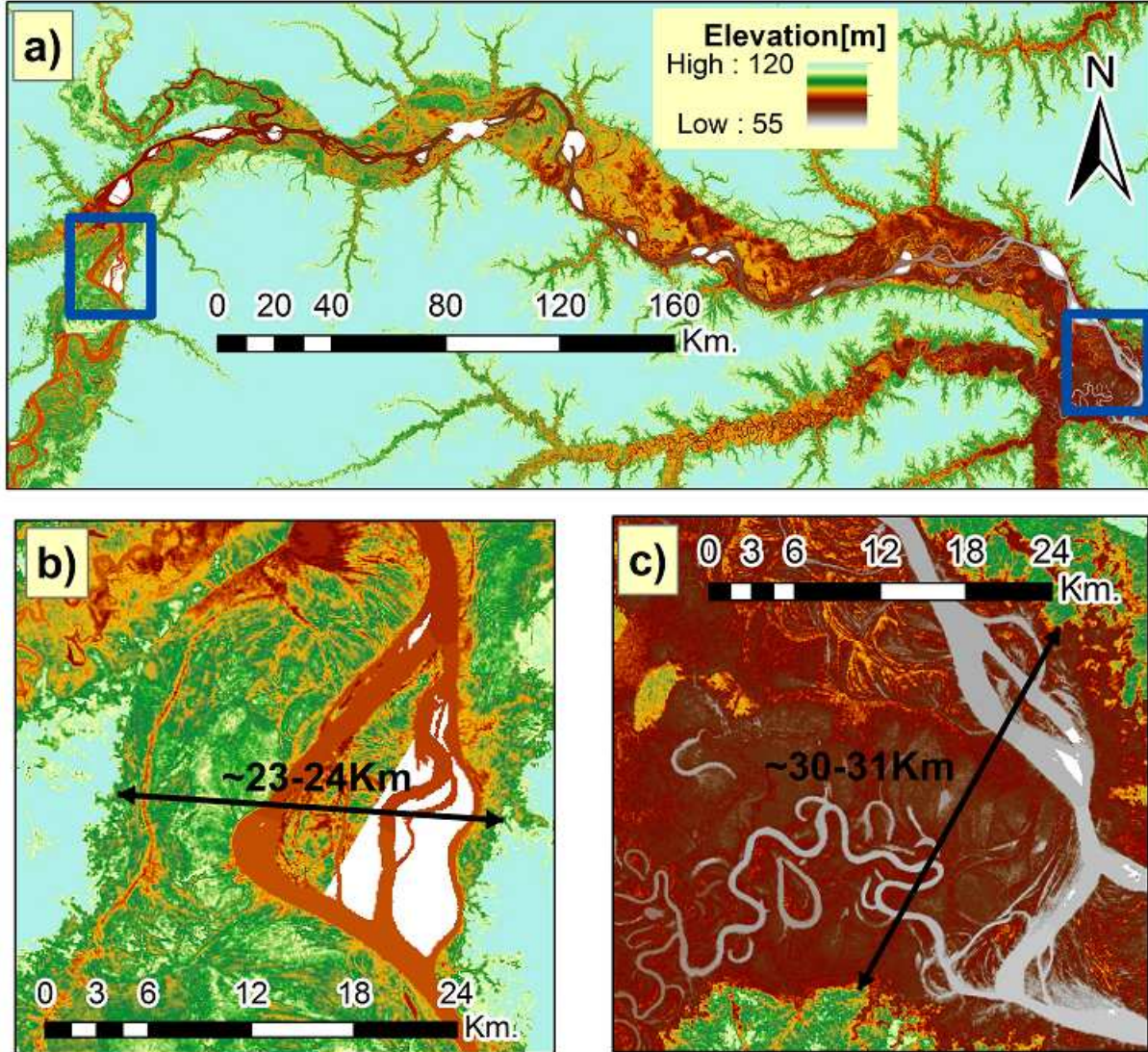


Figure 2.2: a) Digital Elevation Model (DEM) map for the Upper Amazon River Basin valley (from Peru to Brazil). The blue squares are sites LS and MS. The contours are the elevation in meters and depict the floodplain boundary which is the region at which the elevation is less than 120 meters. b) Site MS DEM map. The valley width ranged from 23 to 24 km. c) Site LS DEM map. The valley width ranged from 30 to 31 km. (courtesy of USGS - Shuttle Radar Topography Mission)

where $U, V(m/s)$ are the streamwise and spanwise velocities, $h(m)$ is the water depth, $H(m)$ is the water surface elevation, $S_h(m/s)$ is the source or sink of fluid, $S_x, S_y(m/s^2)$ are the source or sink terms representing the wind, Coriolis force and bottom friction, and $\nu_t(m^2/s)$ is the turbulent viscosity. Additionally, the turbulence closure model $k - \epsilon$ was used to obtain the turbulent viscosity. Although at this scale the bed shear stress and the velocity field can be solved using a mixing length model (which is less computing intensive) $k - \epsilon$ was used to have a better visualization of the streamlines. Streamlines are useful to detect re-circulation areas and thus asses where are the most dynamically active areas. This model adds two more equations to the shallow water equations to solve the turbulent kinetic energy (k) and the dissipation of energy (ϵ)[3].

$$\frac{\partial k}{\partial t} + U \frac{\partial k}{\partial x} + V \frac{\partial k}{\partial y} = \frac{\nu_t}{\sigma_k} \left[\frac{\partial}{\partial x} \left(\frac{\partial k}{\partial x} \right) + \frac{\partial}{\partial y} \left(\frac{\partial k}{\partial y} \right) \right] + P - \epsilon \quad (2.4)$$

$$\frac{\partial \epsilon}{\partial t} + U \frac{\partial \epsilon}{\partial x} + V \frac{\partial \epsilon}{\partial y} = \frac{\nu_t}{\sigma_\epsilon} \left[\frac{\partial}{\partial x} \left(\frac{\partial \epsilon}{\partial x} \right) + \frac{\partial}{\partial y} \left(\frac{\partial \epsilon}{\partial y} \right) \right] + \frac{\epsilon}{k} (C_{1\epsilon} P - C_{2\epsilon} \epsilon) \quad (2.5)$$

where k is the turbulent kinetic energy, ϵ is the dissipation of turbulent kinetic energy, $C_{1\epsilon}=1.44$, $C_{2\epsilon}=1.92$, $\sigma_k=1.0$, $\sigma_\epsilon=1.3$, P is the production of turbulence = $\nu_t \left(\frac{\partial U}{\partial y} + \frac{\partial V}{\partial x} \right) \frac{\partial U}{\partial y}$. From equations (3.4) and (2.5) the turbulent kinetic energy and the dissipation of energy can be determined. Thus, the turbulent viscosity can be calculated as $\nu_t = C_\mu \frac{k^2}{\epsilon}$, where $C_\mu = 0.09$. TELEMAC-2D [55] was used to solve the equations shown above. This program carries out parallel computations using the MPI library [55]. Taking advantage of this feature, and due to the large area to be modeled, 24 processors were used simultaneously for both simulations. In both cases the computational grid was generated using Triangle [153]. The computational domain for LS had about 180,000 elements whereas the computational domain for MS had about 791,000 elements. The maximum edge length of the triangles was kept below 30m for site LS and 15m for site MS (Figure 2.3). Site MS has a higher mesh resolution because the secondary anabranches are narrower than site LS.

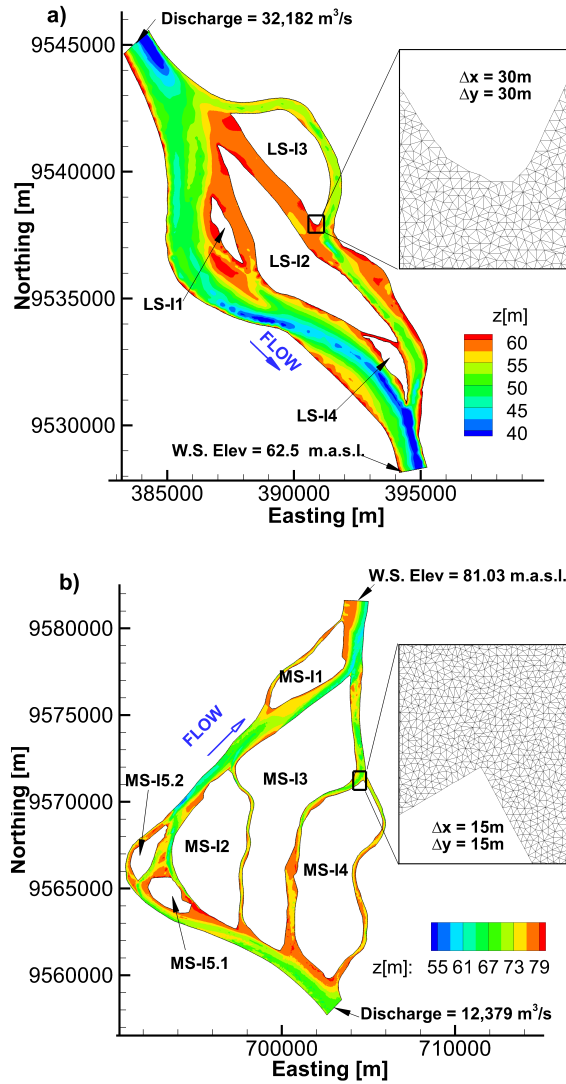


Figure 2.3: a) Site LS bathymetry shows 4 islands by December 2011 (wet season) LS-I1, LS-I2 (Chineria Island), LS-I3 (Ronda Island), LS-I4 (Santa Rosa Island). Grid spacing of the irregular mesh is on average 30m. b) Site MS bathymetry shows 6 islands by August 2010 (dry season) MS-I1, MS-I2, MS-I3 (Muyuy Island), MS-I4 (Panguana Island), MS-I5.1 and MS-I5.2. Secondary anabranches MS-A1 and MS-A3 shows a more meander-style bathymetry with erosion at the outer bank and deposition at the inner bank. Grid spacing of the irregular mesh is on average 15m.

2.2.2 Boundary Conditions

For both cases a constant discharge was applied at the inlet and a constant elevation at the outlet (Figure 2.3). At site LS, a discharge of $32,182 \text{ m}^3/\text{s}$ corresponding to cross section 8 was used as the inlet boundary condition (see Figure 2.1). For the banks and islands a non-slip boundary condition was applied. For this site there were no available water surface elevations nearby. Thus, the water surface level (equal to 62.5 m.a.s.l.) for the outlet was obtained from the bank topographic survey carried out in 2011. On the other hand, for site MS, a discharge of $12,379 \text{ m}^3/\text{s}$ corresponding to the transect muy240 (see Figure 2.1) was used as the inlet boundary condition assuming mass conservation with respect to the inlet. The water surface elevation for the outlet was obtained using a gaging station located at Tamshiyacu town (see Figure 2.1) and the water surface slope calculated from the GPS benchmarks. Since the bathymetry was collected on a period of several days, the average water surface elevation (equal to 81.03 m.a.s.l.) for that period was used.

2.2.3 Model Calibration

The TELEMAC software has been verified and validated in several previous studies and technical reports [54, 43, 44, 45]. The calibration of the model was achieved by changing the value of roughness length (k_s) which is used to calculate the bottom friction coefficient (C_f). It is well known that the roughness length does not depend only on the friction exerted by the grains at the bed surface but also the bed forms geometry [79, 86]. Since the single beam bathymetry does not reflect the geometry of the bed forms, the calibrated roughness should include this effect. The roughness length was calculated as $D_{50} = k_s$. From field measurements and corroborated by other studies [118, 70, 128], the mean particle size $D_{50} = k_s$ for the Amazon River was 0.3mm. [155] presented a similar methodology to calculate roughness length, in which the bed forms geometry effects are included. An equivalent roughness length is calculated by using the values of depth-averaged velocity (U), average depth (H) from the aDcp transects and water surface slope (S) in the following equations:

$$\tau_b = \rho g H S \tag{2.6}$$

$$\tau_b = \rho C_f U^2 \quad (2.7)$$

$$C_f = \left[\frac{1}{\kappa} \ln \left(\frac{11H}{k_s} \right) \right]^{-2} \quad (2.8)$$

where τ_b is the bed shear stress, ρ is the water density, g is the acceleration of gravity, C_f is the friction coefficient and κ is the von Kármán constant. The values of equivalent roughness length for LS and MS ranged from 0.09 m. to 1.94 m. and from 0.2 mm. to 0.6 m, respectively. Due to the great variability of the roughness length along the velocity transects it was decided to use the average value (LS: 0.49 m, MS: 0.08 m) among all aDcp measured transects. Notice that the spacing for single beam bathymetric data for LS and MS were 200 and 100 m, respectively, thus these calibrated roughness lengths should include bed forms that were not captured accurately during field measurements. To test the selected roughness, a comparison of velocities was carried out as shown in Figure 2.2.3 and Figure 2.2.3 for sites LS and MS, respectively. For site MS additional velocity transects for a high flow conditions (taken in May 2010) were use for comparative purposes. These conditions were simulated because the velocity was measured over three days with variable stage and because the planform of site MS was more complex than site LS. This high flow simulation was performed with a discharge of $26,687 \text{ m}^3/\text{s}$. The location of higher shear stresses were similar to the one reported for the low flow simulation, however, the images used herein are for dry season, this simulation will be used only for calibration purposes. In general good agreement was found between the modeled and measured depth-averaged velocities for both sites LS and MS.

2.2.4 Numerical Model Results

The results for bed shear stress and velocity for site LS are shown in Figure 2.6. Regions of bed shear stress greater than 13 Pa are observed and are located in the main anabranch at the downstream outlet and after the confluence with anabranch LS-A4. These regions are related to the migration direction that the anabranching structure is following during recent periods towards Peru. The velocity vectors colored by velocity magnitude are shown in panels 1-6.

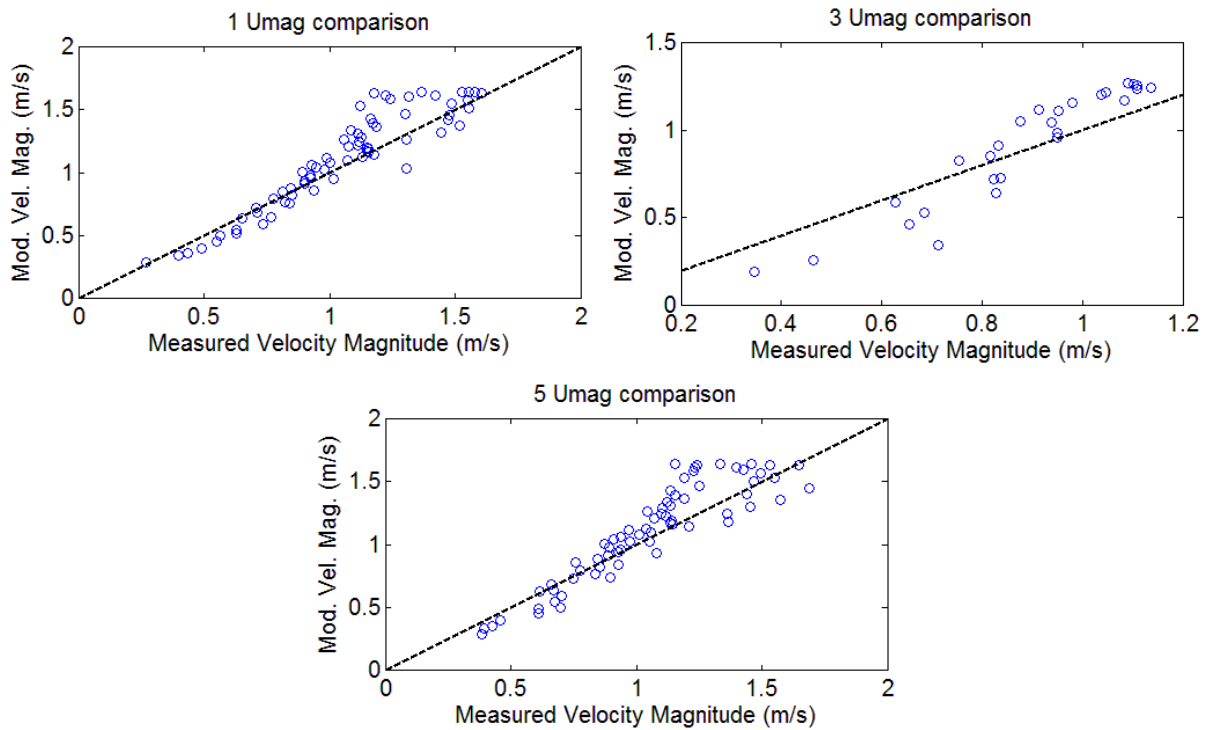


Figure 2.4: Site LS. Comparison of modeled and measured velocities for transects 1, 3 and 5. Notice the consistently underpredicted low velocities and overpredicted high velocities. These behavior could be due to the speed of the boat as long as it measured the transect. The boat hast to travel slower for low velocities and faster at high velocities causing a bias on the real value of the velocities magnitude.

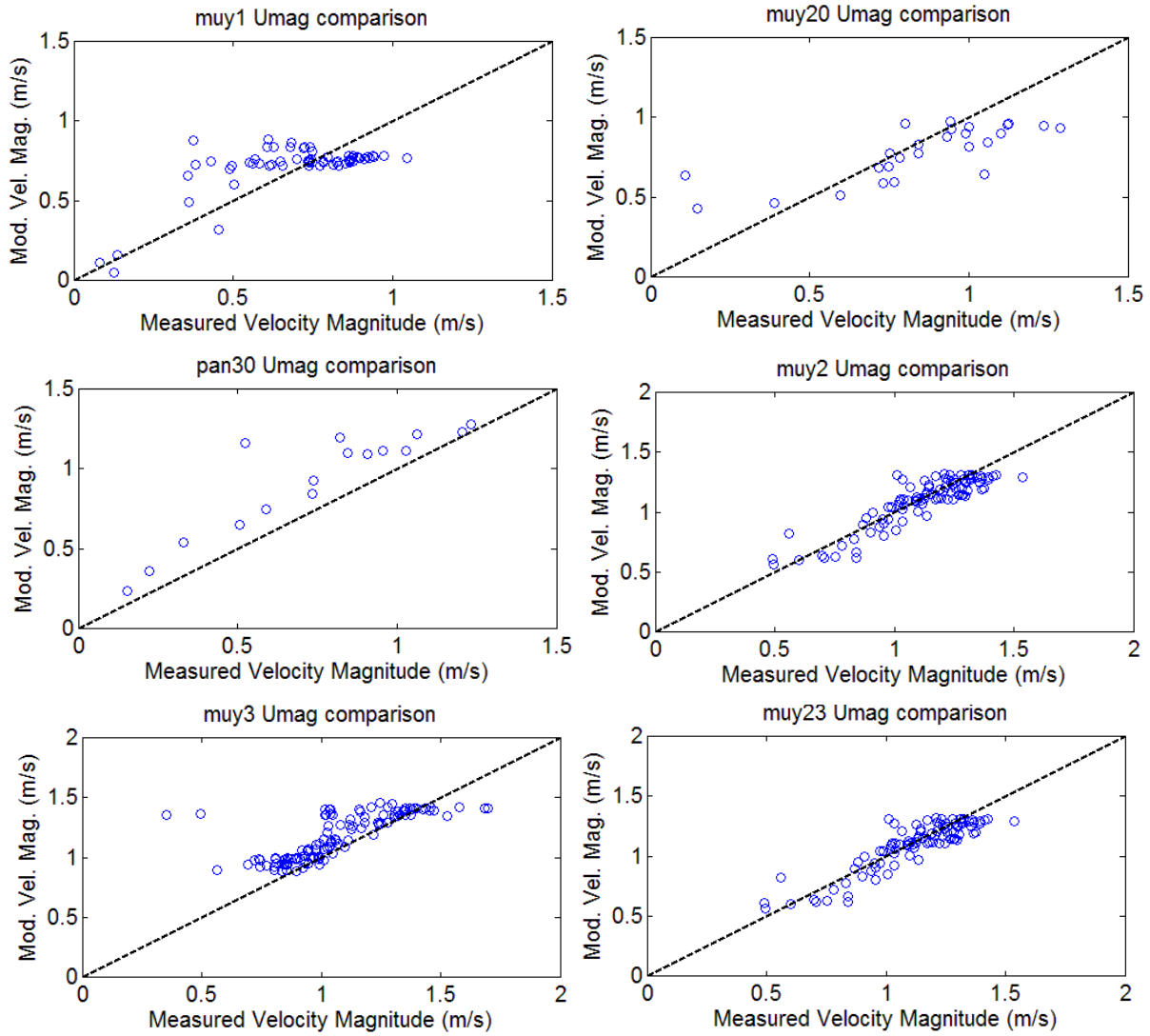


Figure 2.5: Site MS. Comparison of modeled and measured velocities for low-flow (muy1, muy2 and pan30) and high-flow (muy2, muy3 and muy23) conditions.

For a low sinuosity stage, the main anabranch velocity field resembles a meandering river velocity field with higher velocities at the outer bank and lower velocities at the inner bank. For the upstream end of the secondary anabranch LS-A1 (panel 1), the velocity distribution is still under development, thus, the velocity distribution shows an opposite direction with higher velocities at the inner bank and lower velocities at the outer bank. Anabranch LS-A1 shows a lower migration rate from 1984 to 2012 compared to the main anabranch, since, this channel is the closest anabranch to the valley boundary. The secondary anabranch LS-A2 seems to be constrained by the upstream and downstream boundary condition. From field measurements, it seems that the bed in anabranch LS-A2 accreting. If this process continues, less water will flow through LS-A2 and LS-A1, consequently the Leticia harbor will grow inaccessible to large vessels.

[17] noticed that confluences are more dynamically active than the bifurcations. This is observed in Figure 2.6 panels 2 and 6 where recirculation patterns (represented by streamlines) are shown in contrast to the bifurcations where no recirculation patterns are observed.

On the other hand, the results for bed shear stress and velocity for site MS are shown in Figure 2.7. Although, this site starts from a medium sinuosity stage in 1984, by 2010 (the year of the numerical model data) the site is under a high sinuosity stage (this will be explained in the following section). Therefore, the following condition is considered in high sinuosity stage. The high bed shear stress regions are located at the mid to downstream end of the secondary anabranches and near the apex of the main anabranch. These regions have a bed shear stress greater than 8 Pa. The fact that the higher bed shear stresses are located at the downstream end of the secondary anabranches asserts the developing process observed in the low sinuosity stage. In other words, since the secondary anabranches are not completely developed due to geometric constraints (they join with the main anabranch) the bed shear stress increases in the downstream direction. For these regions, a meandering river velocity pattern is also observed (see Figure 2.7 panels 3, 4 and 5) as for the low sinuosity stage. The high bed shear stresses located at the apex of the main anabranch is related to the lateral migration of it. The main anabranch MS-A0 is more dynamically active than other channels, since, it is the furthest one from the valley boundary. Whereas, anabranch MS-A3 is the closest one to the valley boundary and thus it does not show any significant lateral migration

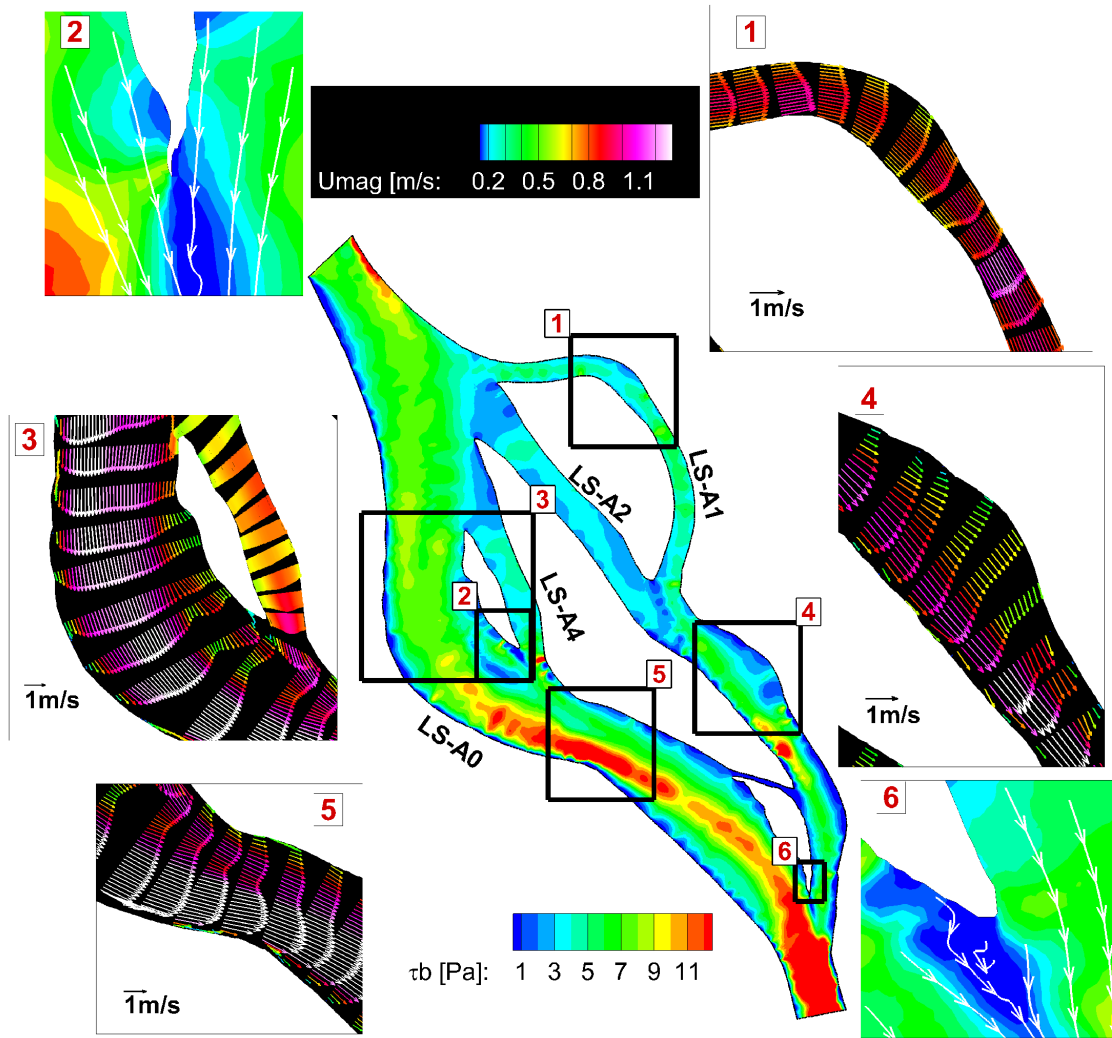


Figure 2.6: LS site. Contours of bed shear stress and velocity vectors colored by velocity magnitude (panels 1-6).

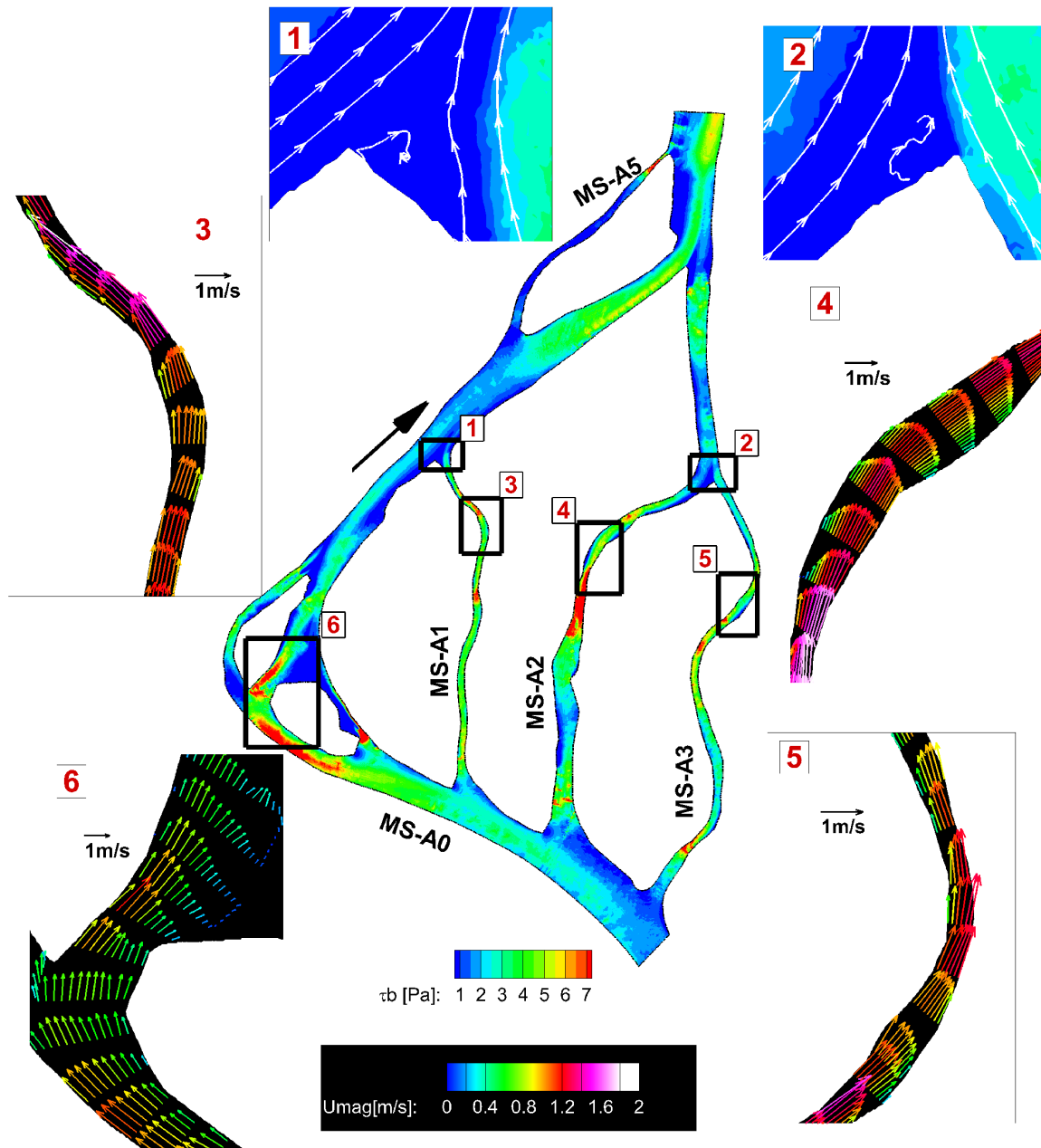


Figure 2.7: MS site. Contours of bed shear stress and velocity vectors colored by velocity magnitude (panels 1-6).

from 1984 to 2012. Moreover, anabranches MS-A1 and MS-A2 do not show any significant lateral migration after 2005 (this will be further explained from satellite images in the next section). The steady condition of these three secondary anabranches (MS-A1, MS-A2 and MS-A3) let us conclude that the high sinuosity of the main anabranch is a more stable stage. Following this stage, the lateral migration rate should decelerate and it will be modified only if an important extreme event upstream (such as extreme discharge) or downstream (such as a chute cutoff process) is carried out. Finally, similarly to the LS site, 2.7 panels 1 and 2 show recirculation patterns to demonstrate that the confluences are more dynamically active than the bifurcations as for the lower stage case. However, the recirculation regions for this site are larger than for site LS.

2.2.5 Satellite Imagery for LS and MS sites

The selection of the scenes was decided based upon a cloud percentage less than 20% and the season at which the image was obtained. Most of the low cloud percentage images were taken in dry season which goes from July to December. Thus, in order to perform a suitable temporal comparison of sinuosity, width and lateral migration, only images for dry season were used herein. For both sites, and when possible, Landsat TM, ETM+ and MSS images were obtained yearly. As a result, for site LS images from 1984 to 2012 (29 years) with a gap between 1993 and 1995 were processed. For site MS, images from 1985 to 2012 (28 years) were used. For MS site, images for 1986, 1990, 1992 and 1993 were not available. In missing years metrics were interpolated and contrasted with available wet years to ensure a correct interpretation. Additionally, for site MS an image for December 1973 was available and used to assess the lateral amount of lateral migration from 1973 to 1985.

The available bands from the satellite imagery data were band 1, 2 and 3. Band 2 was used to highlight the water in all the images. Previous efforts to use Landsat images for multitemporal analysis in the Amazon River basin have been conducted by several researchers [77, 10, 127, 164, 26, 152]. However, only [77] reported 18 years analysis for river migration purposes on the Peruvian region where sites LS and MS are located. The purpose of this section is to explain the change in planform for both sites in a period of more than 20 years.

2.2.5.1 Site LS (Ronda, Santa Rosa and Chinera Islands - low sinuosity stage)

[100] developed a numerical model called "Branches model" in which four processes were used to simulate the morphodynamics based on [16]: channel width adjustment, mid-channel bar formation, channel migration and branch abandonment. Although the work of [16] was focused for bed-gravel rivers, and contrary to the typical avulsion and obstruction theory [105, 167, 101, 169], the "Branches model" is more representative of the physics involved in the Amazon River upper basin.

Figure 2.8 shows the progression of the anabranching structure at LS site from 1984 to 2012 (29 years). Additionally, Figure 2.10 (b) and Figure 2.10 (c) show the temporal change in sinuosity and width for all the anabranches. In this case, the structure migrates toward the right bank likely due to its distance from the valley wall (Figure 2.2). The changes in sinuosity for the main anabranch ranges from 1.04 to 1.09 (see Figure 2.10 (a)). At the middle of this anabranch, a channel width adjustment and an island formation is observed from 1984 to 2003. Thus, a new secondary anabranch called LS-A4 is created by 2003. Also, it is observed that the main anabranch tends to migrate down-valley. This was also observed by [100] in a neural network model of the Jamuna River.

On the other hand, the secondary anabranch that separates islands LS-I2 and LS-I4 called LS-A3 narrows as shown in Figure 2.8 and Figure 2.10 (c). This narrowing is triggered by the creation of the new anabranch LS-A4. Now, according to the numerical model, the highest bed shear stresses are observed downstream the apex of the main anabranch. Figures 2.8 a) to g) show that the high bed shear stress is causing a migration of the main anabranch down-valley. In order to predict the development and evolution of anabranching structures, a 2D hydrodynamic model that can simulate the bed and bank morphodynamics is required. Nowadays similar models are available such as HSTAR [139] and MIKE21C [49] or previous cellular models such as CAESAR [171, 134].

2.2.5.2 Site MS (Muyuy and Panguana Islands)

Figure 2.9 shows the progression of the anabranching structure located at site MS site from 1985 to 2012 (28 years). The initial geometry of the structure encompasses one main branch and four secondary branches (MS-A1, MS-A2, MS-A3, MS-A4 and MS-A5). For the secondary anabranch MS-A2, the main

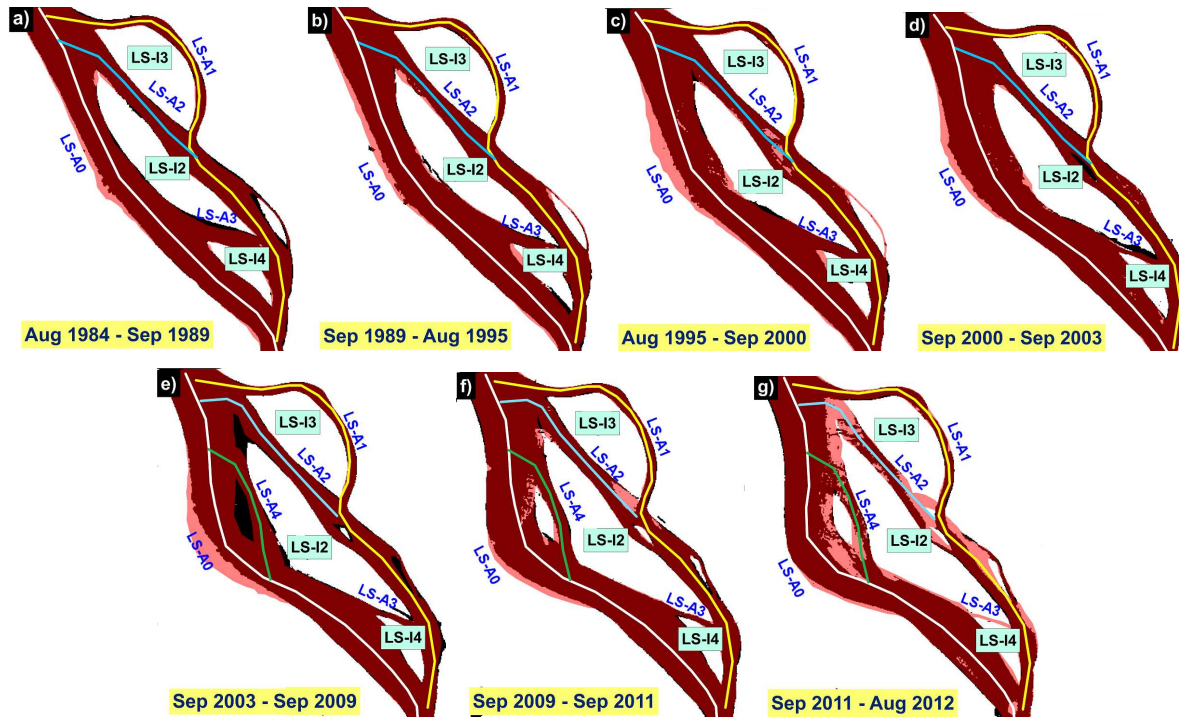


Figure 2.8: Site LS (low sinuosity stage) multitemporal Landsat images. All the images are on the same scale. On each sub-figure two Landsat band 2 images from different years have been overlapped. The earlier year is a black and white binary image and the latest year is a red and white binary image with a transparency of 50%. The results are images showing the earlier year in black color and latest year in a red color. Whenever the earlier year showed dry zones and for the latest year those zones are wet, the color is pink. Additionally the main anabranch (white line) and the secondary anabranches LS-A1 (yellow line), LS-A2 (cyan line), LS-A3 and LS-A4 (green line) along with islands LS-I2, LS-I3 and LS-I4 are shown.

process is channel migration. After 1985 the migration is down-valley with one downstream skewed bend that impacts anabranch MS-A3 in 2005 (a 20-year process). This impact causes a branch abandonment at the left bank of the confluence between MS-A3 and MS-A2 and an upstream retreat of the confluence. This retreat causes a high bed elevation slope at the outlet of anabranches MS-A3 and MS-A2. This high bed gradient can be seen in Figure 2.3

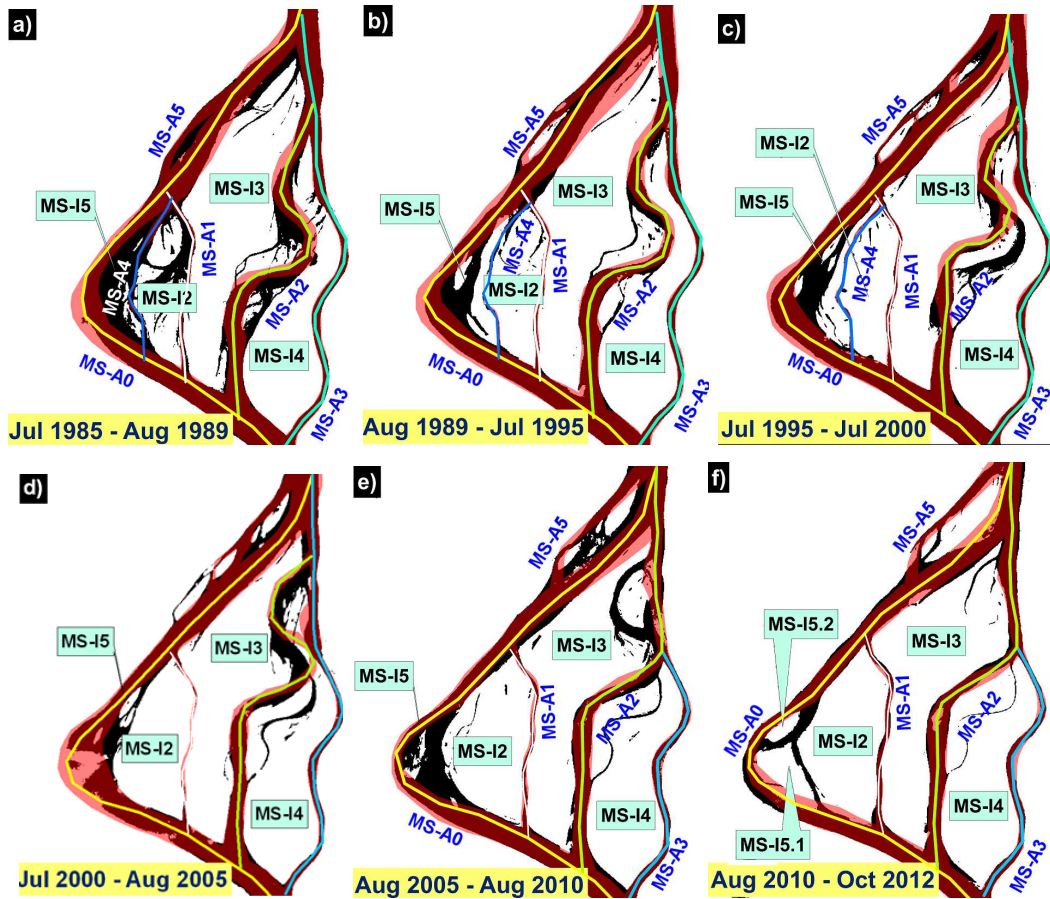


Figure 2.9: Site MS (medium and high sinuosity stage) multitemporal Landsat images. All the images are on the same scale. On each sub-figure two Landsat band 2 images from different years have been overlapped. The earlier year is a black and white binary image and the latest year is a red and white binary image with a transparency of 50%. The results are images showing the earlier year in black color and latest year in a red color. Whenever the earlier year showed dry zones and for the latest year those zones are wet, the color is pink. Additionally the main anabranch (yellow line) and the secondary anabranches MS-A1 (white line), MS-A2 (green line), MS-A3 (cyan line), MS-A4 (blue line) and MS-A5 along with islands MS-I2, MS-I3, MS-I4 and MS-I5 are shown.

(a) where the bed elevation collected in 2010 is shown. It is observed that anabranch MS-A3 shows a more meander-style configuration with erosion at the outer bank and deposition at

the inner bank. Whereas, anabranches MS-A2 and MS-A1 were still developing this bed configuration. Some additional observations are:

- The secondary anabranches migrate downstream for the widest secondary anabranch that is not adjacent to the valley boundary. That is why anabranch MS-A2 migrates after 1985 and not MS-A1 and MS-A3 which are the closest one the floodplain boundary.
- The mechanism used by the main anabranch to create new secondary anabranches is the channel widening and mid-channel bar formation that result in island formation. It is assumed that this happened between 1985 and 2013 for the northern region of the anabranching structure creating anabranch MS-A5 (see Figure 2.9).
- According to [126] the Amazon River planform is a result of the tectonic setting, climate change and sea-level fluctuations interaction. Moreover, [127]’s findings showed that the width to depth ratio and homogeneous bank texture do not correlate with the variation in sinuosity of the river. In contrast, the sinuosity correlated very well with the floodplain width. As shown in Figure 2.2 the floodplain for this structure is asymmetrical with respect to the main channel being more distant from the river at the left bank. Thus, since floodplain width is assumed to be correlated with the sinuosity in this location it is expected to have a larger migration of the structure at the left bank than at the right bank. The latter adds a restriction to the structure mechanism explained above which is related to soil textures and tectonic setting.
- As shown in Figure 2.9 (a) to (f) and Figure 2.11 (b) the sinuosity of the main anabranch goes from a medium sinuosity of 1.3 to a high sinuosity stage of about 1.5, an increase of 10 to 15% in a period of 25 to 30 years.

2.3 METRICS ANALYSIS

From the satellite imagery it was possible to obtain metrics such as channel average width, channel sinuosity and annual migration rate of the centerline for each anabranch. The width and the sinuosity were obtained from a relational database created in ArcGIS [1] for the centerlines and polygons that outline the water. Thus, the average width was calculated

by dividing the polygon areas by its centerline length. The centerline was obtained by digitalizing the channel banks and using the NCED Stream Restoration Toolbox [119] to interpolate the centerlines. Figures 2.10 (b), 2.10 (c), 2.11 (b) and 2.11 (c) show the temporal variation of the sinuosity and the width for all the anabranches resulted using the information from the relational databases.

Additionally, the NCED Stream Restoration Toolbox was also used to obtain migration vectors from two consecutive years for the study period of site LS and MS. Figure 2.10 (a) and 2.11 (a) shows an example of the centerlines migration in a 10 years period (1990 to 2000) for sites LS and MS, respectively. Another relational database was created for the centerlines migration in which the centerline point-migration (length of the curved vectors shown in Figures 2.10 (a) and 2.11 (a) and the streamwise coordinate of each point of every anabranch was stored. The point-migration is positive if the displacement is to the right bank and negative if is to the left bank. On the other hand, the total average migration is the sum of all the migration vectors divided by the length of the channel centerline. Finally, the annual migration rate for each anabranch was calculated as the total average migration divided by the period for which that total migration was developed. Figures 2.10 (d) and 2.10 (d) show the total average migration of the main anabranch for sites LS and MS, respectively.

2.3.1 Low sinuosity (LS) metrics

For site LS the sinuosity of the secondary anabranches in site LS is almost constant (Figure 2.10 (a)). Whereas, the sinuosity of the main anabranch in site LS is increasing slowly until 2005 when a rapid increase occurred and the sinuosity went from 1.04 to 1.09 approximately (about 5% in 29 years). This increase is related to the peak in annual migration rate for that year as shown in Figure 2.10 (d). On the other hand, since the secondary anabranch is disappearing, its width decreases from approximately 800m to 200m while LS-A1 has a constant value. However, secondary anabranch LS-A2 decreases in 2002 and remains constant until 2012 while the main anabranch LS-A0 increases from 1985 to 2000 and then it is almost constant until 2006 when it is narrowed and starts to increase until 2012. From these

observations we can conclude that for a low sinuosity stage, the increase in annual migration rate causes an increase in the main anabranch sinuosity. Also the main anabranch widens until it reaches an equilibrium width after a peak in migration. On the other hand, for this stage the metrics of the secondary anabranches do not change dramatically except for any anabranch that, due to the discharge diverted to the main anabranch (because of the widening), tend to disappear (since less water will flow through it). These dynamics are shown, for example, in the width of LS-A3 that decreases until it is 200m before disappearing.

2.3.2 Medium and high sinuosity (MS) stage metrics

For site MS, the main anabranch sinuosity increases from 1.35 to 1.64 between 1985 and 2012 (about 21% in 28 years). This is a higher change than for a low sinuosity stage of the main channel. Whereas, the sinuosity of the secondary anabranches are almost constant except for MS-A2 and MS-A3 which are interacting because of the down-valley migration of MS-A2 as explained in the previous sections. On the other hand, the width of the main anabranch remains constant with some spurious peaks in 2000 and 2010 due to the difference in water stage for the months used in the 2000 and 2010 satellite images. Again, there is a clear relation between the annual migration rate peak in 2007 shown in Figure 2.11 (d) and the sinuosity increase of the main anabranch. However, the width does not show any apparent correlation with the annual migration rate.

2.4 DYNAMICS OF ANABRANCHING STRUCTURES CONCLUSIONS

Two sites in the Upper Amazon River Basin representing three main anabranch sinuosity stages from 1.02 to 1.5 (low, medium and high sinuosity) were analyzed by means of a field data collection, the application of a two dimensional hydrodynamic numerical model and a temporal analysis of satellite images. Water surface levels, bathymetry and velocity measurements were surveyed during the field campaign. The water surface used to determine the bed surface was calculated from the surveyed water surface levels and the water slope.

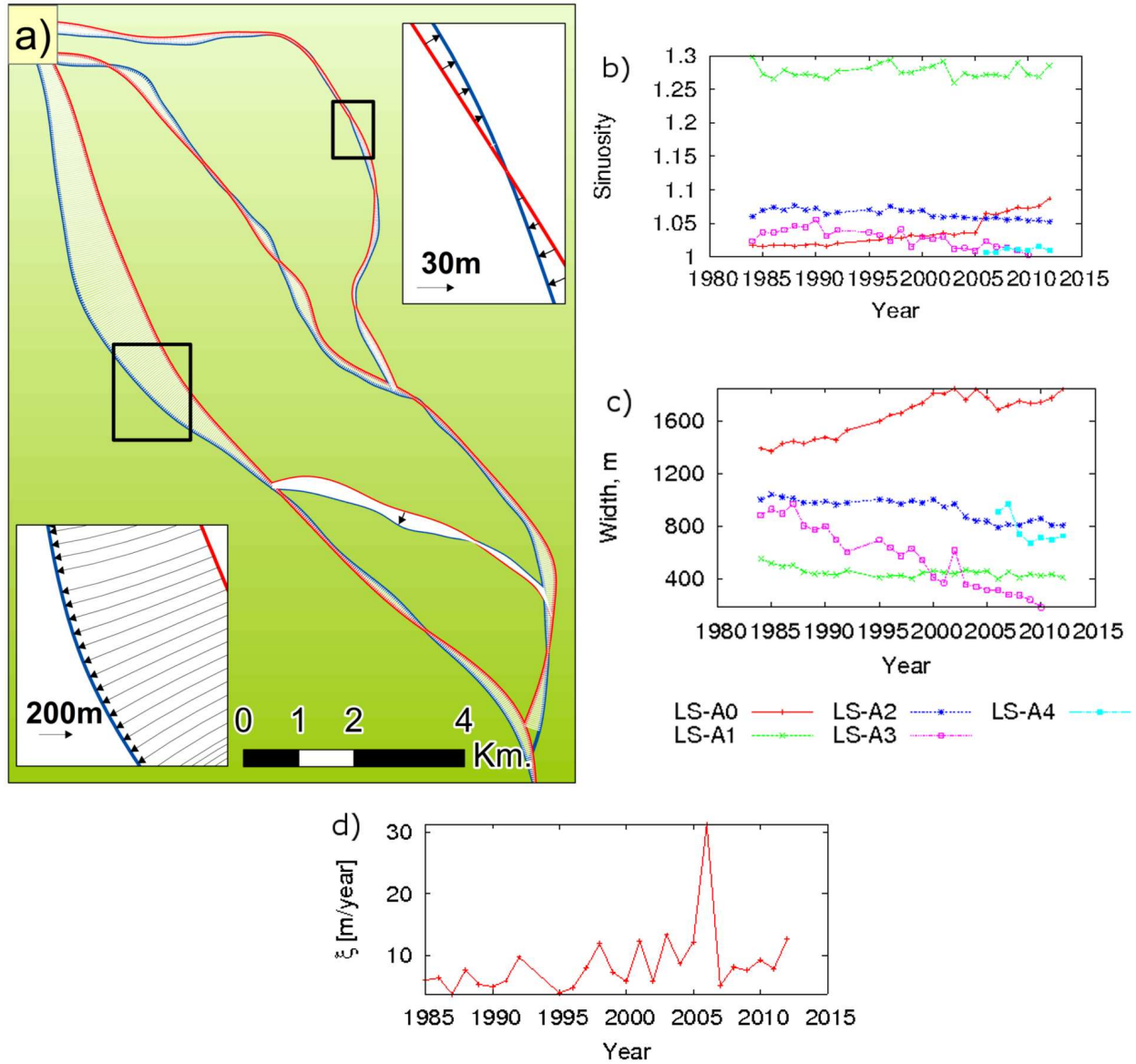


Figure 2.10: LS site. a) Migration vectors for a period of 10 years (between 1990 and 2000). The red lines are for year 1990 whereas the blue lines are for year 2000. b) Sinuosity from 1984 to 2012. c) Channel width from 1984 to 2012. d) Annual migration rate for the main anabranch from 1984 to 2012.

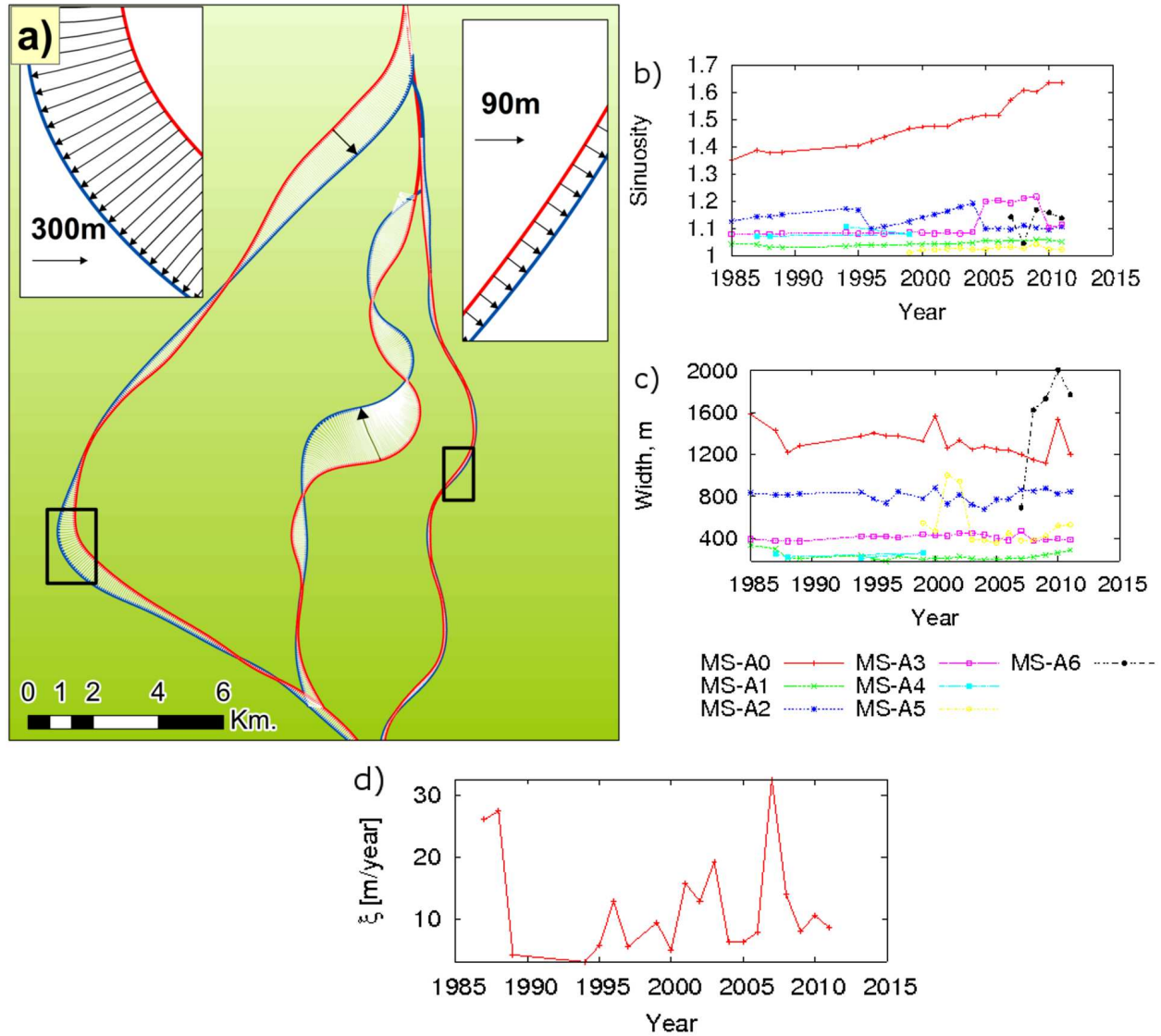


Figure 2.11: MS site. a) Migration vectors for a period of 10 years (between 1990 and 2000). The red lines are for year 1990 whereas the blue lines are for year 2000. b) Sinuosity from 1985 to 2012. c) Channel width from 1985 to 2012. d) Annual migration rate for the main anabranch from 1985 to 2012.

However, it was considered that for site MS (high sinuosity) the water slope varies between anabranches in such a way that considering a single water slope for all the study area will

lead to some errors when correcting for bed elevation. Therefore a surveying of water levels at each anabranch was carried out in contrast to LS site, where only water levels at the inlet and outlet were collected. This procedure can be used in any anabranch structure that present a complex secondary anabranches layout such as MS.

From the numerical models and the satellite images analysis it was possible to characterize the morphodynamics processes of all the sinuosity stages. Thus, it was observed that the secondary anabranches for all the three stages behave as non-developed meandering rivers. This can be confirmed by the fact that high velocities at the outer bank and low velocities at the inner bank are better defined at the downstream end of the secondary anabranches. On the other hand, the fact that the bed shear stress is higher at the downstream end of the secondary anabranches indicates that hydrodynamics of them are still developing.

By using satellite images, the planform dynamics of both stages were characterized adequately. For example, it was observed that the main morphodynamic process developed from the low sinuosity stage to the high sinuosity stage is the channel width adjustment and island formation. This process triggers the creation of new secondary anabranches as shown in site LS (low sinuosity stage) in 2003 and in site MS in 1995 (medium to high sinuosity stage). During this processes for a low sinuosity stage, the main migration is carried out by the main anabranch. Also, from the metrics analysis, the sinuosity change rate showed to be higher at a medium to high sinuosity stage than at a low sinuosity stage. Thus, at a low sinuosity stage, the width of the secondary channels is inversely correlated with the main anabranch width and sinuosity in contrast to a high sinuosity stage where the width of almost all the anabranches remains constant.

The floodplain boundary influence on the anabranches planform was studied. It was observed that secondary anabranch LS-A1 in site LS (low sinuosity stage) is not migrating due to proximity the valley boundary and it is restrained by secondary anabranches LS-A2 and LS-A3). The bed of anabranches LS-A2 and LS-A3 is aggrading which could cause their detachment from the main anabranch. By 2012, the water in LS-A3 is almost null. It is expected that the same might happen to LS-A2 which will trigger the migration down-valley of LS-A1, which implies serious problems for the delimitation of the boundary between Brazil, Colombia and Peru.

Although several differences were found between a low sinuosity and high sinuosity stage, there were also some common findings in all the stages. For instance, planform of the secondary anabranches in all the sinuosity stages is controlled by the main anabranch migration which is triggered by extreme hydrology events (see Appendix C for more information). Moreover, from the satellite images, it was concluded that there is a width threshold for the secondary anabranches of 200m at all the sinuosity stages. After this threshold is reached, the anabranch may disappear in the following years. With the methodology presented herein it was possible to characterize the interaction between the main anabranch and secondary anabranches in terms of sinuosity stages. However, to get a better insight of the problem a 2D hydrodynamic model able to predict bank and bed geometry is needed. Although, there are existing models none of them have been validated or proved to work in the Upper Amazon River Basin anabranching structure. If this is done it will be possible to answer when and how fast the boundary between Brazil, Colombia and Peru will change. On the other hand, due to logistics limitation it was possible only to obtain field data from two sites. If more data is available it could be possible explore correlations among metrics of the main anabranch, including the migration rates and field data such as velocities and sediment concentration. Further, new metrics can be incorporated in this analysis such as bifurcation and confluences asymmetry.

3.0 MODULATION OF THE FLOW STRUCTURE IN MEANDERING RIVERS DUE TO BED FORMS

River bed forms have been studied extensively using varied approaches including experimental [137, 21, 42, 178, 22, 180, 65, 176, 5, 6, 136, 36], numerical [163, 186, 83, 40, 136, 9, 73, 39] and field measurements [23, 52, 144]. From these studies, important insights have been made regarding the interaction of the flow and river morphology. For example, [176] stated that sediment transport influences bed roughness and vice versa, thus, the prediction of any of those is still challenging. [176] described that the characteristic of ripples are commonly assumed to be related to turbulence characteristics such as bursts and sweeps and [148] related turbulence with ripples creation. [42] stated that ripples and dunes are developed from the sand wavelets. [58] stated that ripples and dunes scale with the sediment size and water depth, respectively.

Regarding to the effect of the bed forms in river hydrodynamics, it is well known that when bed forms are not present on a river bed, all the drag force on the bed is due to skin friction [56]. However, in the presence of bed forms, the drag force on the bed is a combination of skin friction and form drag. Skin friction is the force responsible for sediment transport and could include different sediment size scales. Therefore, in presence of bed forms, the form drag has to be subtracted from the total drag force, thus to calculate the bed shear stress responsible for sediment transport. Form drag predictors are available in the literature such as [56, 59, 184]. Drag form is also important when unsteady flow conditions are observed, since morphology of bed forms changes due to changes in flow discharge [136]. Based on field data from a large river, [155] carried out a sensitivity analysis on the range of roughness length using three approaches, [1] Colebrook-White equation (CWE) , [2] a grain size based equation and [3] the [175] roughness predictor. The minimum roughness

length value, 0.001m, resulted from the grain size based equation in contrast to the [175] predictor that gave a value of 0.73m and a CWE maximum value of 3m. The [175] and CWE approaches include the effect of bed forms and therefore prove the importance of including the river bed forms in the calculation of the bed roughness and therefore the modulation of the bed shear stress.

Studies such as [178, 180, 179, 177, 87] have characterize the three dimensional shape of river bed forms. Therefore, the location of the bed forms' crests and trough are not horizontally aligned and neither the distribution of the bed shear stress. Nowadays, it is possible to capture the bathymetry of a river with very high resolution using multibeam echosounders as shown by [144] in the Parana River. Pioneering bed forms size discrimination toolbox using 1D Wavelets has been presented by [38] and [87]. [87] developed a methodology to discriminate bed morphology (ripples, dunes and bars) for synthetic morphodynamic signals as well as for the Parana River, by combining 1D wavelets and robust splines. The discrimination of bed form scales is useful for roughness characterization purposes and for calibrating numerical models.

[9] presented an original contribution on the effects of progressing bedforms on the near-bank shear stresses along an experimental bend, and hypothesized that the presence of bed forms may increase up to 50% the magnitude of bank shear stresses, thus directly influencing fluvial or hydraulic erosion rates. This statement arises from three-dimensional numerical simulations of an experimental fixed bed with vertical side walls for several bed morphology configurations with progressive bed forms and without bed forms. Nevertheless, the question on what percentage the bank shear stresses (where walls are non-flat and non-verticals) are being modulated by progressive bed forms remained unanswered. Herein, [9]'s hypothesis is tested at the field scale in the meandering Wabash River. The Wabash River has shown large migration rates during the last years, however, most of the past studies have been focused in the flow regime [20, 98], ecosystem integrity [14, 46, 68, 78, 162], river planning (several US Army Corps of Engineers reports since 1938) and water quality [41, 93, 122, 123] and little on its morphodynamics, except, [189] who study the sediment transport variation due to cutoffs and the classical paper [99] that showed a depositional model of point bars in the lower Wabash.

3.1 STUDY SITE AND FIELD DATA

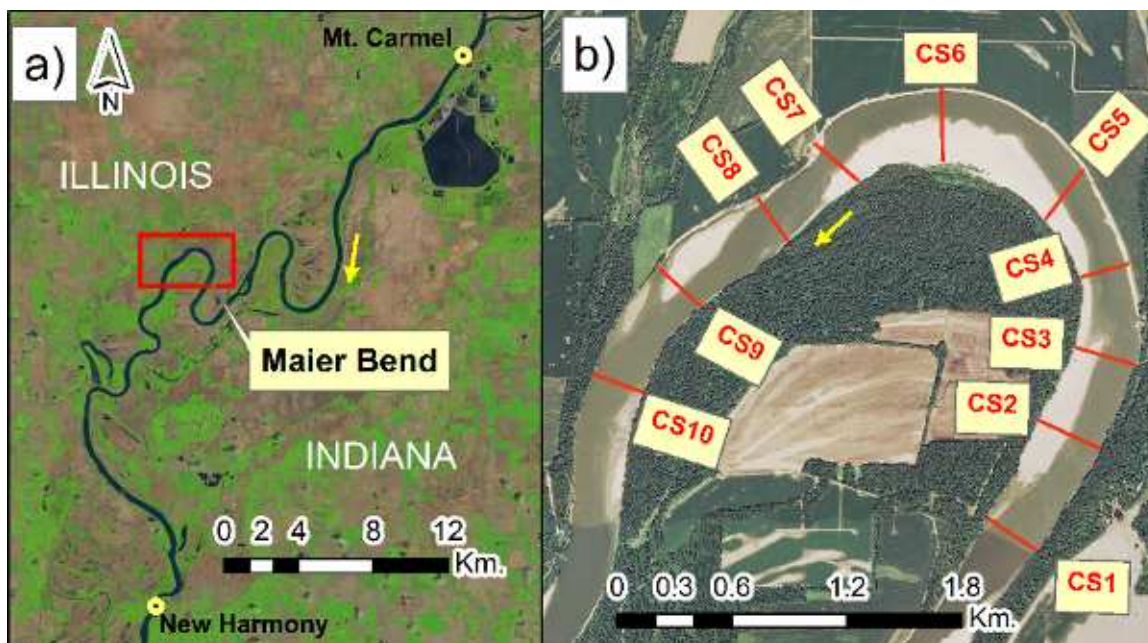


Figure 3.1: (a) Location of gaging stations Mt. Carmel and New Harmony used to calculate water surface elevation. The figure also shows the location of the Maier bend which was located between the Stateline of Indiana and Illinois. (b) Location of the velocity (aDcP) transects CS1 to CS10 on Maier bend. The measurements were collected on February of 2012.

The study site is the Maier Bend in the Wabash River located along the Illinois and Indiana Stateline as shown by Figure 3.1 (a). Several field campaigns have been conducted in 2011 and 2012 to collect bathymetry, bank topography, velocity measurements and soil characterization along the Wabash River. The bathymetry and velocity measurements were surveyed on the same field campaign (February, 2012) thus, taking advantage of high flow stage. The bank topography was surveyed on August of 2011 at low flow stage while the soil samples were collected on November of 2011. The bank topography was measured using a laser scanner Topcon GLS-1500 and a RTK GPS Topcon GR-3. The laser scanner survey was made from the point bar located at the Maier Bend as shown in Figure 3.2. Due to

the bend curvature, the range of view of the laser was decreased and therefore several laser stations were used to survey the bank. Most of the bank geometry was captured by the laser scanner except for low reflectivity spots such as bedrock and the top of the bank (which was no visible from the laser scanner location). A GPS RTK was used to complete the point cloud at places where the laser scanner did not capture the bank geometry. The base station for the GPS RTK data was corrected using OPUS (Online Positioning User Service) from the National Geodetic Survey of the United States. About 17.6 million points were collected for the bank topography after neglecting outliers due to low signal intensity and filtering out some vegetation.

The bathymetry was collected using a Reson multibeam echosounder and the velocity measurements were collected with an aDcp (Acoustic Doppler Current Profiler) instrument. In total, 10 velocity cross sections were used as shown in Table 3.1 and Figure 3.1 (b). From the bathymetry data, it was possible to determine the water depths of the river at a very high resolution. On the other hand, using the water levels (see Table 3.2) of the closest gaging stations (Mount Carmel and New Harmony, see Figure 3.1), it was possible to obtain a water slope of 1.1×10^{-4} . [118] argue that water surface slopes for large rivers are difficult to measure accurately. According to [166, 147], the slopes of these rivers are in the order of 1×10^{-5} . This order of magnitude is for the world's largest rivers such as the Orinoco or Amazon River at which the water slope is calculated using optical level methods at different times of the day. Since the order of magnitude for the water surface slope of the Wabash River is greater, it is expected that a more accurate method such as the one using water levels from gaging stations for the same time will give better results. A water surface TIN (Triangulated Irregular Network) was built using the water surface slope and the water level recorded at Mount Carmel and New Harmony gaging stations. Next, the bed elevation points were calculated by subtracting the measured water depth from the constructed water surface TIN. The final bathymetry was post-processed to neglect outliers and mapped onto a grid of 0.5m of resolution which turned out to have a total of 5.9 million of points. The final dataset with the GPS (Global Positioning System) that covered the point bar and bank edges, LIDAR (LIght Detection And Ranging) that covered the outer bank and multibeam echosounder points that covered the bed morphology is shown in Figure 3.2.

Table 3.1: Maier bend velocity transects. Where τ_b is the shear stress, \bar{U} is the mean average velocity for each transect and k_s is the roughness height.

Transect	Area [m ²]	Width [m]	W. Depth [m]	τ_b [Pa]	\bar{U} [m/s]	k_s [m]
CS1	2206.3	306.4	5.9	6.37	1.14	0.21
CS2	2252.1	355.3	5.04	5.44	1.18	0.09
CS3	2295.7	327.6	5.71	6.16	1.12	0.21
CS4	2058.5	260.7	6.6	7.12	1.23	0.21
CS5	2070.8	325.5	5.06	5.46	1.25	0.07
CS6	2197.1	376.3	4.54	4.9	1.17	0.06
CS7	1974.3	305	5.17	5.58	1.27	0.06
CS8	2191.4	278.8	6.56	7.08	1.13	0.34
CS9	2150.1	303.6	5.78	6.24	1.13	0.2
CS10	2129.4	279.7	6.31	6.81	1.17	0.24

Table 3.2: Gaging station water surface elevations used to calculate the bed elevation.

Station	Date	Maximum W.S. Elev. [m]	Minimum W.S. Elev. [m]	Average W.S. Elev. [m]
Mt. Carmel	2/3/2012	6.98	6.9	6.95
New Harmony	2/3/2012	5.13	5.12	5.13

The soils were characterized using in-situ tests such as BSTs' (Borehole Shear Test) and jet tests to obtain parameters like friction angle, matric suction, cohesion, erodibility and critical shear stresses. Sediment samples were analyzed in the laboratory to obtain parameters such as pore water pressure and grain size distribution. For the purpose of this work only the shear stresses and sediment size distribution are used. The locations of the tests are shown in Figure 3.1 (b). The average critical shear stress (τ_c) from the jet test at the bank resulted in 3.7Pa and this value is considered as the average bank critical shear stress along the entire bend.

3.2 NUMERICAL MODEL AND COMPUTATIONAL SETUP

Two simulation cases were prepared for this study. The first case (C-1) was built using the measured bathymetry and bank topography surveyed in 2011. The second case (C-2) was built using a filtered bathymetry using [87]'s methodology and the same bank topography as the first case. Thus, the effect of the bed forms modulation in the near-bank shear stresses could be assessed by comparing simulations with bed forms and without them. For both cases, a three dimensional RANS (Reynolds Averaged Navier Stokes) was used with a $k - \omega$ SST (shear stress transport) turbulence model [125]. This model has shown good behavior for rugged relief surfaces such as the ones used for the bed and bank. The solution of the equations was carried out in OpenFOAM [69]. OpenFOAM is an open source code software that can handle CFD (Computational Fluid Dynamics) models such as DNS (Direct Numerical Simulation), LES (Large Eddy Simulation), DES (Detached Eddy Simulation) and RANS models. Related to river bed forms, [73] have presented LES modeling of bed forms during superimposition and amalgamation processes.

3.2.1 Governing Equations

The well known three dimensional Navier Stokes equations considering a RANS approach are:

$$\frac{\partial \bar{u}_i}{\partial x_i} = 0 \quad (3.1)$$

$$\frac{\partial \bar{u}_i}{\partial t} + \bar{u}_j \frac{\partial \bar{u}_i}{\partial x_j} = -\frac{\partial \bar{p}}{\partial x_i} + \frac{1}{\rho} \frac{\partial}{\partial x_j} (2\nu \bar{s}_{ji} - \overline{u'_j u'_i}) \quad (3.2)$$

where $\bar{s}_{ji} = \frac{1}{2} \left(\frac{\partial u_j}{\partial x_i} + \frac{\partial u_i}{\partial x_j} \right)$. As explained by [181], the system of equations defined by Equations 3.1 and 3.2 needs to be closed by finding an expression for the Reynolds-stress tensor $\tau_{ij} = -\rho \overline{u'_i u'_j}$. Using a Boussinesq eddy-viscosity approximation $\tau_{xy} = \nu_t \frac{dU}{dy}$, it is possible to close the system by using a replacement for the eddy viscosity ν_t (for more detail about the Boussinesq eddy-viscosity approximation, see [181]). For the cases mentioned above, a two-equation turbulence energy model called $k - \omega$ SST was used [125]. It is known that this model provides reliable results in cases of flow separation such as the one caused by river bed forms. In general, the model uses a $k - \omega$ formulation near the wall and a $k - \epsilon$ model anywhere else in wall bounded domain. The model computes the eddy viscosity ν_t using an equation for the turbulent kinetic energy k and the specific dissipation rate of energy ω . The implemented equations in OpenFOAM varied slightly from the standard $k - \omega$ model [125] in the ω terms:

$$\nu_t = \frac{a_1 k}{\max(a_1 \omega, SF_2)} \quad (3.3)$$

$$\frac{\partial k}{\partial t} + U_j \frac{\partial k}{\partial x_j} = P_k - \beta^* k \omega + \frac{\partial}{\partial x_j} \left[(\nu + \sigma_k \nu_T) \frac{\partial k}{\partial x_j} \right] \quad (3.4)$$

$$\begin{aligned} \frac{\partial \omega}{\partial t} + U_j \frac{\partial \omega}{\partial x_j} = & \alpha S^2 - \beta \omega^2 + \frac{\partial}{\partial x_j} \left[(\nu + \sigma_\omega \nu_T) \frac{\partial \omega}{\partial x_j} \right] \\ & + 2(1 - F_1) \sigma_{\omega 2} \frac{1}{\omega} \frac{\partial k}{\partial x_i} \frac{\partial \omega}{\partial x_i} \end{aligned} \quad (3.5)$$

Where, $S = \sqrt{2S_{ij}S_{ij}}$ is the strain rate magnitude, $a_1 = 0.31$, $\beta^* = 0.09$ and the rest of the variables are defined by the following equations:

$$P_k = \tau_{ij} \frac{\partial U_i}{\partial x_j} \quad (3.6)$$

$$\sigma_k = \frac{1}{F_1/\sigma_{k1} + (1 - F_1)/\sigma_{k2}} \quad (3.7)$$

$$F_2 = \tanh \left[\left[\max \left(\frac{2\sqrt{k}}{\beta^*\omega y}, \frac{500\nu}{y^2\omega} \right) \right]^2 \right] \quad (3.8)$$

The algorithm used to solve this system of equations was the SIMPLE (Semi-Implicit Method for Pressure Linked Equations) algorithm. The construction of the solution matrices is carried out using the Finite Volume (FV) method. The simulations were ran until reaching steady state conditions (residuals of less than 1×10^{-3} for all variables U , k , ω and p). A second order Gaussian integration numerical scheme was used for all terms of the system of equations. On the other hand, the interpolation schemes used from cell centers to face centers were linear for all the gradient terms and linear upwind for all the divergence and Laplacian terms in the system of equations.

3.2.2 Mesh Generation, Initial and Boundary Conditions

The basic input data for mesh generation are surfaces for the bed, bank and the water elevation given as STL (STereoLitography) files for cases C-1 and C-2. The procedure carried out to determine these input files is explained below.

3.2.2.1 Case C-1: with bed forms For C-1, the bed and the bank surfaces were obtained from the MBES (multibeam echosounder) and GPS-LIDAR topography data respectively. Whereas, the water surface was calculated using the water levels recorded at gaging stations New Harmony and Mount Carmel as explained above.

3.2.2.2 Case C-2: without bed forms For C-2 the banks surface was the same as C-1. However, the bed surface was obtained from a discrimination filtering procedure [87]. Figure 3.3 shows an example of the initial measured bed profile (η) and the partition into ripples ($\eta_{1,3}$), dunes ($\eta_{2,3}$) and bars ($\eta_{3,3}$). Notice that the geometry of bed forms geometry changes along the Maier bend. The wavelengths for the upstream (λ_{R-2}) and downstream (λ_{R-1}) bed forms are less than 10 m and between 10m and 100 m, respectively (see Figure 3.3). The water surface needed special attention since no field data for the case without bed forms exists. It is known that the effect of bed forms increases bed roughness, thus manifesting an increase in water surface elevation, herein, it was assumed that the condition without bed forms will produce the same water surface slope as the case with bed forms. Thus, the methodology used to obtain the same water slope for both cases (C-1 and C-2) was to run a one-dimensional simulation in HEC-RAS (Hydrologic Engineering Centers River Analysis System) for each case and calibrate the Manning’s roughness coefficient for C-2 until the water slope for both cases were approximately the same. Notice that the water discharge is maintained constant. The boundary condition used for both cases was the energy gradient at the outlet and the average discharge ($2535 \text{ m}^3/\text{s}$) from aDcp measurements (cross section at the inlet of the computational domain). [155] proved that the water slope is very sensitive to the change on roughness length due to small roughness increments. Because of that, the Manning’s roughness coefficient was varied in increments of 0.01 until the slope was approximately the same for both cases. Based on the HEC-RAS simulations of C-2, the water surface elevation was lowered by 1.3m from the water surface elevation for C-1.

3.2.2.3 Mesh construction for C-1 and C-2 The meshes were built using the mesh generation tools SHM (snappyHexMesh) and blockMesh from OpenFOAM. The procedure consisted in creating a background mesh with hexahedral elements using blockMesh as the one showed in Figure 3.4 (a). First, the bottom and top boundaries of the background mesh were defined by the limits of the bank topography, the river bed bathymetry and the water surface obtained for cases C-1 and C-2 as explained above. For both cases the background mesh had cell sizes of 0.5m x 1.8m in the vertical and horizontal directions, respectively. Although, SHM requires in some cases that the aspect ratio of the cells to be about 1:1, the

meshes obtained herein resulted in a very good approximation of the actual point cloud as shown in Figure 3.4 (c). In order to shape the mesh according to the bank topography and river bed geometry for both cases, an STL (StereoLithography) file was created using the point clouds from each case. For the case with bed forms, the STL file is created directly from the points surveyed on the field campaigns. However, for the case without bed forms a filtering process of the river bed points was carried out before the creation of the STL. The filtering process followed a procedure that uses wavelet analysis and robust spline filters developed by [87]. For that, a TIN of the river bed was constructed and streamwise profiles were mapped onto this TIN as shown in Figure 3.3. The profiles and the points in the profiles were spaced 0.5m creating a regular evenly spaced mesh. Each of these profiles were considered a signal on which a discrimination process was carried out to filter the bed forms and to obtain a new set of points for only the bars geometry ($\eta_{3,3}$). With the new set of points, a surface of the river bars was created and converted to an STL file as shown in Figure 3.4 (b).

Next, the background mesh is modified using these STL files with a three step algorithm carried out by SHM. The first step of the algorithm consists of detecting and removing the cells that are outside the boundary delimited by the STL file and the background mesh. In the second step, the remaining cells of the domain are snapped or smoothed to match the STL geometry as best as possible. Finally, a layer addition step at the walls is carried out. The mesh was processed up to the second step since no layers were needed at the walls. Thus, the meshes used for the case with bed forms had 5.6 million of points, whereas, the case without bed forms had 4.9 million of points. These meshes were hybrid meshes with polyhedral and prisms elements as shown in Figure 3.4 (c).

3.2.2.4 Initial and Boundary conditions for C-1 and C-2 To initialize the flow in the domain, a potential flow simulation was carried out for each case. The values of velocity from this simulation were used to initialize the cases. For both cases, the continuity residuals were kept below 1×10^{-5} to ensure a good initialization. The initial values of pressure (p), turbulent kinetic energy (k) and specific dissipation rate (ω) were 0, 7.5×10^{-4} and 7.14×10^{-3} , respectively. For the boundary conditions of velocity, a constant flow rate of $2,517 \text{ m}^3/\text{s}$, obtained from velocity cross section CS1, was used at the inlet. Also, at the

inlet, constant values of k and ω of 7.5×10^{-4} and 7.14×10^{-3} were used, respectively. The top of the mesh used a surface built from the water surface elevation based on analysis of the closest gaging stations. Because of that, a rigid lid approximation is considered a good approach for the top boundary condition for both cases. Thus, a slip boundary condition was considered for the velocities and pressure at the top of the mesh. The bank and the bed were considered as wall boundary conditions. Thus, a no slip boundary condition with wall functions was used at those faces of the mesh. At the outlet, zero flux was considered for all the variables.

3.2.3 Validation

The validation was achieved by comparing velocity transects CS5, CS6, CS7 and CS8 (see Figure 3.1). These transects were selected because they are located near the apex of the bend where the shear stress will be analyzed and the effects of the boundary conditions are less important. According to [8], previous studies compared measured quantities and model predictions by plotting data on 1:1 graphs [64] and visual comparison [151] of measured and predicted velocity fields in separate plots. Herein, a methodology similar to the one used by [8] was carried out. For that purpose a rectangular grid with indexes i, j was used to map the measured and modeled velocity magnitude values. Next, the difference between the velocity magnitude is compared by an error percentage between the measured and modeled quantities given by $Error[\%]_{i,j} = \frac{UmagMod_{i,j} - UmagMeas_{i,j}}{UmagMeas_{i,j}}$; where $UmagMod_{i,j}$ is the modeled velocity at point i, j and $UmagMeas_{i,j}$ is the measured velocity at point i, j . Figure 3.5 shows that there are areas with an over prediction error of more than 20% located as vertical strips at the center of the cross sections. Also, there are areas with an under prediction error of more than 20% that are located at the bottom of the inner and outer bank. However, the distribution of the velocity magnitude for all cross sections analyzed is very well predicted by the model with less than 10% of over prediction at the outer bank and less than 10% of under prediction at the inner bank for most of the regions in each cross sections.

3.3 RESULTS

3.3.1 Shear Stress Characterization

As depicted in Figure 3.6 (a) and Figure 3.3 (a), the bed forms are three dimensional and according to their sizes, they can be separated in region R-1 and region R-2. In region R-1, the bed forms show crests' alignments oriented upstream and downstream and has the larger bed forms with an average bed forms wavelength (λ_{R-2}) between 10m and 100m. The bed forms in region R-2 have crest's alignments perpendicular to the channel centerline. Also, they are smaller than region R-1 with an average bed forms wavelength (λ_{R-1}) smaller than 10m. For both cases (C-1 and C-2), the shear stresses at the bed and the side wall were calculated. The bank topography showed some scarps similar to ones found in riprap failures by particle erosion [27]. These scarps might be product of mass failure and slump blocks creation at the bank which modify the bank erosion rates of the bank face and toe [183]. Two of the largest scarps are located in region R-1 and were labeled b1 and b2 as shown in Figure 3.6 (a).

Figure 3.6 (b) shows the same bank topography used for C-1 and C-2, thus the scarps remained in both conditions. Since the bed forms were already filtered out for C-1, there is no difference between the bed morphology in region R-1 an R-2.

Figures 3.7 and 3.8 show the shear stresses for case C-1 and C-2, respectively. The bed and bank shear stress magnitudes are between 4Pa and 8Pa for the majority of the bed and bank regions. At the bend, in general, the larger the bed form is the larger the shear stress is exerted at the crest. Thus, there are bed forms at which the shear stresses exerted at the crest ranges from 8 to 12 Pa whereas for the larger bed forms, the shear stresses are higher than 12Pa. On the other hand, at the bank there are patches with shear stresses higher than 10Pa located at the bank toe and at the middle of the bank height. The top of the bank is characterized by a shear stress less than 4Pa. Due to this shear stress distribution at the outer bank, the fluvial or hydraulic erosion will be most active at the middle of the bank height and at some portions of the bank toe. The latter enhances the occurrence of cantilever failures and planar failures. Scarps b1 and b2 show bank shear stresses below 2Pa inside of

them. Based on field measurement, the average critical shear stress inside of the bank scarps is 3.7Pa. Figure 3.6 (c.1) shows that at the toe of these scarps there are some slump blocks. As stated by [170, 108], slump blocks produced by mass failure of river banks modify erosion rates by reducing the shear stress acting on the bank because of a shifting of the locus of high streamwise velocity away from the bank. Also, as said by [132] the impact of the slump blocks on meander migration rates and shapes has not been investigated so far. Based on the field observation and results from the numerical model, it seems that the shape of these scarps have been defined more due to mass failure (planar or cantilever failure) rather than due to fluvial erosion.

Since there were not bed forms on case C-2 the bed shear stress presented a smoother shear stress distribution with a higher zone at the outer bank as expected (ranged from 10 to more than 12 Pa). Also, it is observed patches of high bank shear stress for case C-2 at the middle of the bank height and at the bank toe as well as C-1. However, the range of the patches for higher shear stresses at the bank for C-2 has a lower range (from 8Pa to 10Pa). The fact that the location of the high shear stress patches are at the same position on the bank as in C-1 indicates that the bank shear stress distribution for this bend is independent of the bed forms. Therefore, it can be concluded that although the presence of bed forms in the bend are showing an increment on the bank shear stress the mass failure type could be the same.

In order to compare the bank shear stresses for both cases (C-1 and C-2), a procedure to assess the relative excess of shear stresses when bed forms are present was carried out. A structured orthogonal curvilinear grid was used to map the bank shear stresses for case C-1 and C-2. These values were compared to obtain the percentage that C-2 shear stresses are greater or smaller than C-1 shear stresses. Since C-1 and C-2 meshes have different water surface elevation and therefore different top boundary, the results were mapped only in C-2 mesh which is the shortest domain. This percentage is given by $\Delta\tau_{C-1,C-2} = 100 \left(\frac{\tau_{C-2} - \tau_{C-1}}{\tau_{C-1}} \right)$, where τ_{C-1} and τ_{C-2} are the shear stresses for C-1 and C-2, respectively. Figure 3.9 shows the excess percentage of bank shear stresses for C-1 and C-2. It seems that bank shear stresses are greater in the majority of the bend for the case with bed forms, as hypothesized by [9].

It can be observed from Figure 3.9 both regions (R-1 and R-2) present a top region in which the exceed of shear stress is more than 150% on most of the bank area. However, for the bank toe of region R1 there are two patches where the shear stress for C-1 is 150% higher than C-2 denoted as ss1 and ss2. There is also a zone at which the bank shear stress is more than 25% less in C-2 than in C-1 denoted as ss3 in Figure 3.9. These three zones (ss1, ss2 and ss3) cover an horizontal length of about 50m. Additionally, in region R-2, a zone denoted as ss4 (at the bank toe) shows bank shear stresses that are 25% less in C-2 than in C-1. Zone ss4 has a horizontal length of about 200m. On the other hand, in scarps b1 and b2 the shear stress is exceeded in 150% comparing C-1 and C-2; except at the top, where the shear stress is less than 50% for C-1 than for C-2. Therefore, the increase in bank shear stresses due to bed forms is stronger at the top of the bank than at the toe. However, due to the scarps, this effect is reversed having a lower shear stress because of bed forms. Finally at the bank toe, the shear stresses are higher or lower depending on the bed forms size. More research is need to understand the modulation of different bed form sizes into the bank shear stresses and its importance for planform shapes and migrations rates.

3.3.2 Flow Characterization

[9] proved (at the experimental flume scale) that fluvial bed forms modulate the secondary flow direction in a meandering channel. Herein, the secondary flow is analyzed for a field scale with some differences from the work of [9] such as a non-flat bank surface and two regions of bed forms sizes (R-1 and R-2). To assess the difference in the secondary flow modulation for different bed forms sizes, two cross sections labeled as CS5.1 and CS5.2 were located in region R-1 whereas cross sections CS6.1 and CS6.2 were located in region R-2 (see Figure 3.6 a)). Figure 3.10 shows the velocity vectors between C-1 and C-2 cases for all four cross sections (CS5.1, CS5.2, CS6.1 and CS6.2). The presence of bed forms pushes the flow upward or downward, and their intensities depend on the bed form sizes (see Figure 3.10 a), b), c) and d)). The upward and downward velocity patches are not traveling more than one half of the depth of each cross section and thus the main recirculation zones are preserved for cases C-1 and C-2. However, in C-1 case, at CS6.1 there is a recirculation zone located

between a distance of 280m and 300m from the left bank that does not remain in case C-2. Despite of this, the velocity magnitude is the same on that cross section for both cases. Also for both cases the flow is directed toward the right bank for CS5.1, CS5.2 and CS6.1 (see Figure 3.10 a), b), c) e), f) and g)). On the other hand, at CS6.2, the flow goes toward the left bank which is the reverse direction found in the other cross sections. Therefore, it can be concluded that although the main direction of the secondary flow is not bed form dependent but oriented by the inertia of the flow the bed forms modify the direction of the secondary flow by upward and downward velocity patches. That is why changes in the direction of the secondary flow are observed at specific locations of the bend geometry such as the apex (CS6) and the end of the bend (CS6.2) for both cases. Notice that [9] had a smaller width to depth ratio than the one observed for the Wabash River, thus, the influence of bed forms on secondary flows are different.

In contrast, to [9] experiments, herein, we have a bank morphology that varies three dimensionally. The streamlines found inside scarps b1 and b2 (see Figure 3.6) are shown in Figure 3.11 for C-1 and 3.12 for C-2. The following analysis considers that both cases (C-1 and C-2) will present the same bank morphology. It has to be noted that physically a difference in the bed morphology should result in different bank morphology. However, herein it is considered that the bed morphology is different due to a filtering process. A filtering process can happen indirectly when the bed morphology is surveyed with single beam echosounders instead of multibeam echosounders. In both cases the streamlines follow a spiral upward pattern inside the scarps that changes vertically. For instance, in Figure 3.11 a), the highest streamlines ($z > 113m$) of the main flow travels downward when approaching the scarp and then enters into a spiral motion upward until it exits the scarp and joins the main flow. Whereas, for the lower elevations ($111m < z < 113m$), the streamline travels downward and then upward without entering into a spiral motion before joining the main flow again.

However, since the water depths for C-1 and C-2 are different, the spiral patterns are also different. In Figure 3.12 a) the streamlines for scarp b1 are shown for the C-2 case. The streamlines move downward a shorter distance than for case C-2 (with bed forms). However, the path of the higher ($z > 113m$) and lower ($111m < z < 113m$) streamlines is the same

as for case C-1. Thus, because of the spiral motion caused by the presence of scarps, low velocity recirculation regions are created in which shear stresses are lower. As observed in the field, inside of the scarps, fine sediments are deposited between the slump blocks (see Figure 3.6 (c.3)). The sediment might be deposited due to the mechanism found from the streamlines by traveling from the main channel flow in suspension and trapped inside the scarps until sedimentation is achieved. Once the sediment is deposited the fluvial erosion will not remove it due to low shear stresses as discussed previously. Therefore, a mechanism of aggradation and degradation of the bank occurs because of a recirculation region and mass failure respectively. Judging from the size and shape of the scarps, the bank mass failures remove more sediment from the bank than it can be deposited from the spiral motion of the sediment.

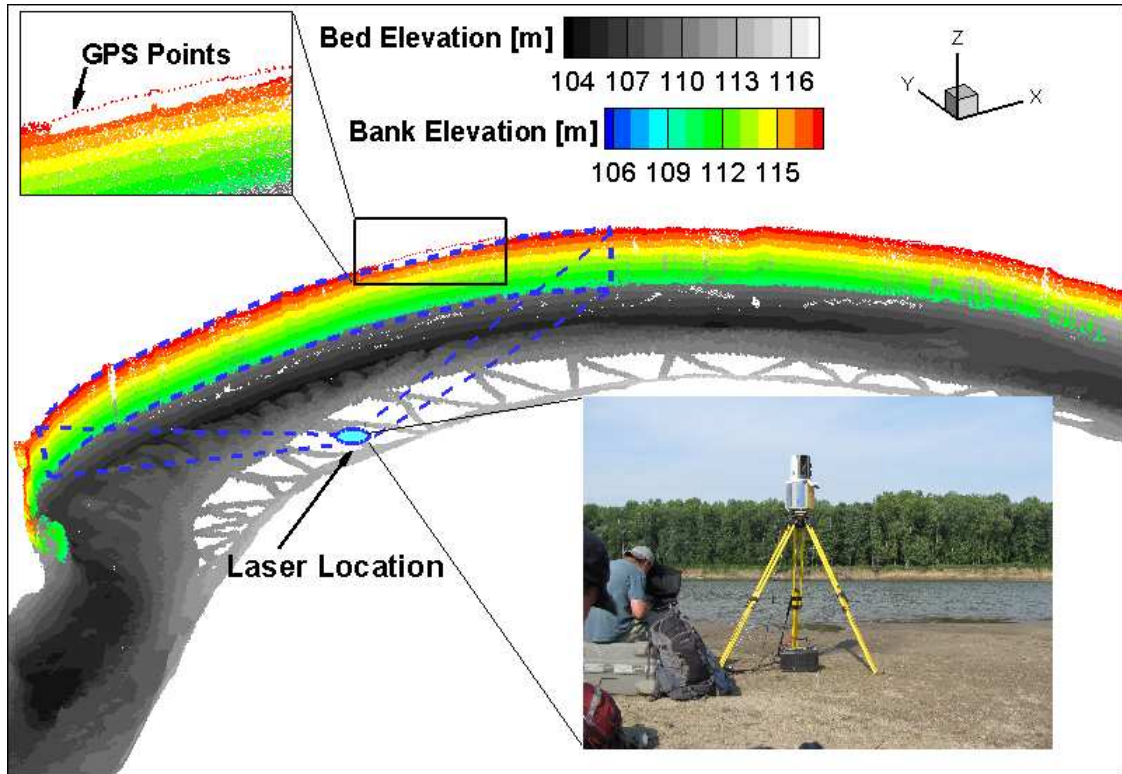


Figure 3.2: LIDAR survey of the bank and MBES survey of the bed for Maier bend. The bank points (LIDAR) are rainbow colored while the MBES points are grayscale colored. To complete the bank surface additional points surveyed with an RTK GPS were surveyed as shown in the detail box on the left top corner. The laser was located in the point bar and is shown in as a cyan circle.

3.4 BANK SHEAR STRESS DUE TO BED FORMS CONCLUSIONS AND FUTURE WORK

In general, the presence of river bed forms increases the shear stress at the bank. The increase in shear stress can be more than 150% which is greater than the value found in an experimental flume scale [9]. One of the reasons of this difference lay in the fact that the bank morphology analyzed herein is fully three dimensional in contrast to the flat surface used in [9]'s condition. Scarps and slump blocks were observed on the bank of Maier bend which affected the distribution of shear stresses and thus influences the bank's rate of migration. Although the shear stresses are greater when bed forms are present, it was observed that the distribution of the high and low shear stress is the same for both conditions C-1 and C-2. The shear stress was higher at the toe and at the middle of the bank height which causes greater fluvial erosion on these areas and therefore enhances mass failures such as cantilever or planar failures. Implications of considering bed forms in a numerical simulation affect predominantly the prediction of hydraulic erosion. A typical situation in which the bed forms are not considered accurately in modeling is when a bathymetry surveying method such as a single beam echosounder is used compared to a fully multi-beam survey. In these cases, it is important to determine the minimum spacing for cross sections needed at which the effects of the bed forms will be minimum.

The bed shear stresses are also modified when bed forms are present. Likewise, when there are no bed forms, the bed shear stresses are smoothly distributed along the bed and when bed forms are present, there are patches of high shear stress at the crests of the bed forms. The values of the shear stresses vary with the amplitude of the bed forms, the largest is the amplitude the highest are the shear stresses. Finally, for Maier bend the bed morphology presented two different bed forms size regions called R-1 (largest bed forms) and R-2 (smallest bed forms). The effect of the bed forms presence at the bank toe is different in these regions. Patches of high shear stresses are found when bed forms are considered, thus [9]'s hypothesis is proved at natural scale. The effect of the bed forms in the secondary flow was analyzed as well. The presence of bed forms create recirculation cells caused mainly by the ejections and sweeps but do not modify the direction of the main

streamflow. This is because the large width to depth ratio might play an important role to determine the interaction of natural curvature-driven secondary flows and bed forms-driven secondary flows. [9] studied the effect of the migration of the bed forms in the secondary flow. In the bend studied in the Wabash River, the bathymetry corresponds to only a single water stage and therefore no implications of the bed forms migration on the secondary flow was discussed. However, for the case with bed forms, in cross section CS6.1 (located at a dune crest - see Figure 3.6 a)) there were recirculation cells that are not present in the case without bed forms (see Figure 3.10 c)). The latter corroborates [9] findings that concluded that the highest modification of the secondary flow occurs when a dune crest passes through a control section.

On the other hand, by visualizing the flow streamlines it was concluded that the recirculation created in the scarps might induce deposition of sediment inside the scarps. This was corroborated from a field visit at which fine sediment deposits were found inside the scarps.

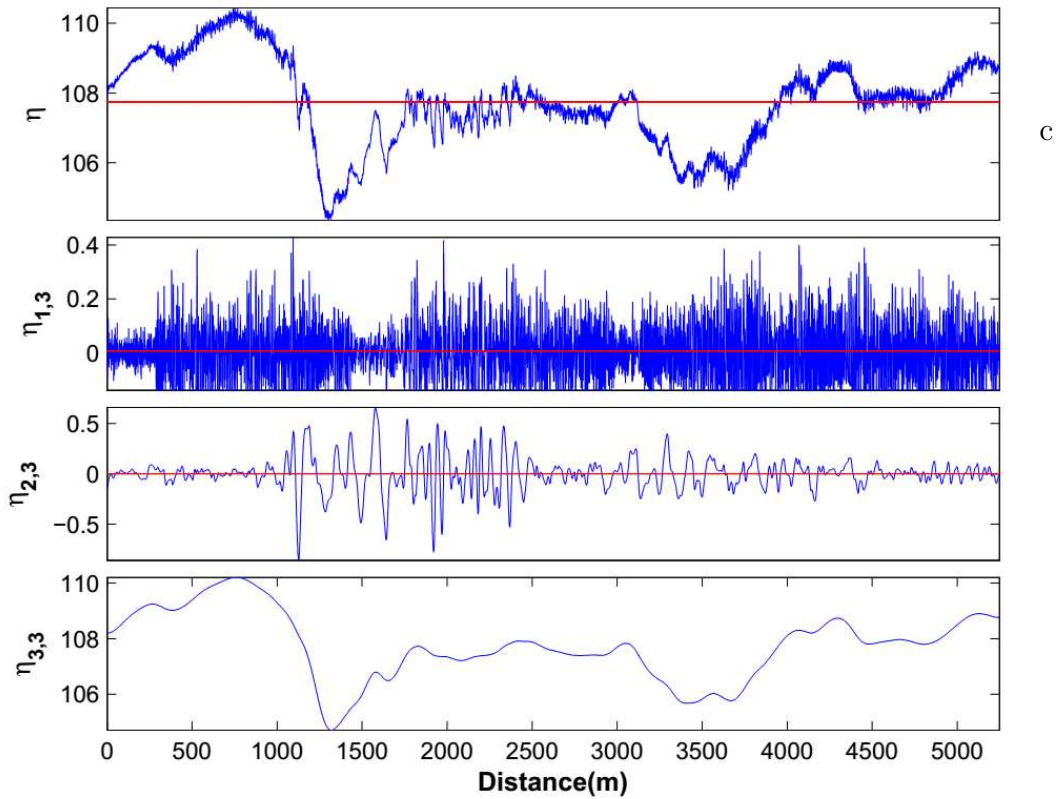
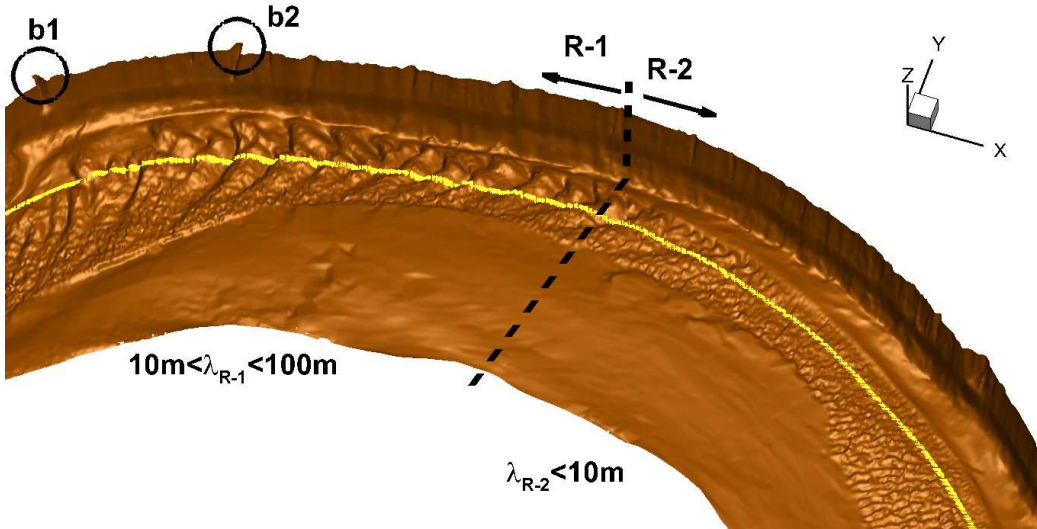


Figure 3.3: Discrimination procedure for a bed profile. (a) Shows the location of the profile processed on (b). λ_{R-1} is the wavelength for the bed forms found in R-1 and λ_{R-2} is the wavelength for the bed forms found in R-2. η , $\eta_{1,3}$, $\eta_{2,3}$ and $\eta_{3,3}$ are the amplitudes for the original, the small bed forms, the large bed forms and the bar signals respectively.

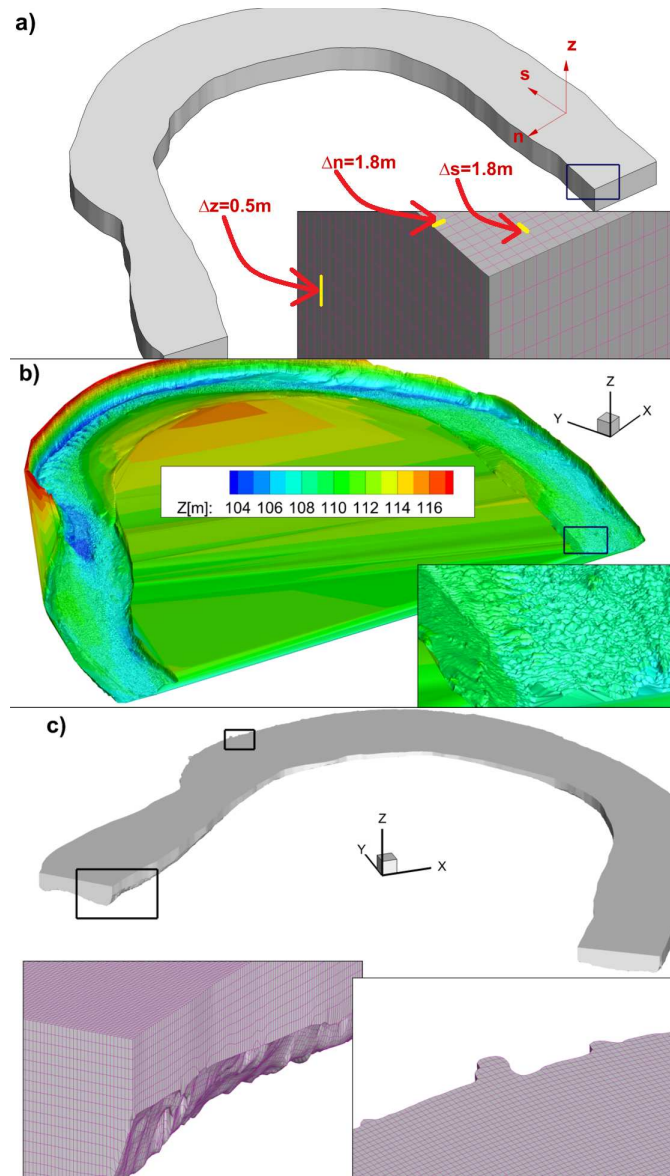


Figure 3.4: Mesh construction procedure. (a) A background mesh made of hexahedral elements was built. The streamwise, spanwise and vertical resolution was 1.8m, 1.8m and 0.5m respectively. (b) An STL surface was used to subtract the background mesh using SHM (see text for details). (c) Final mesh used for the case with bed forms. It is shown the detail of the bed and bank geometry captured by SHM (see the text for details).

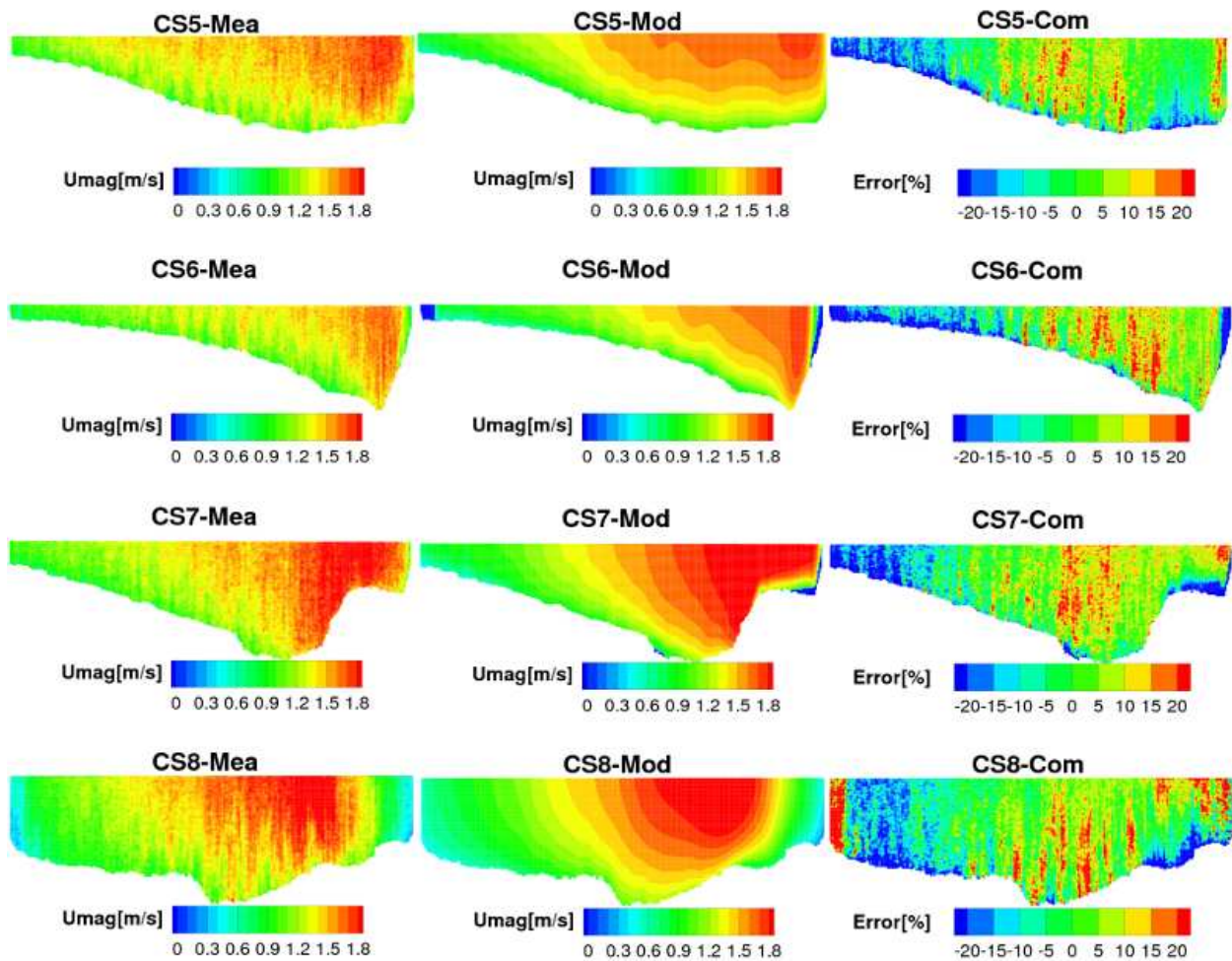


Figure 3.5: Comparison of the aDcp and modeled velocity magnitude. CS5-Mea, CS6-Mea, CS7-Mea and CS8-Mea views show the measured aDcp velocity magnitude contours for CS5, CS6, CS7 and CS8 respectively. CS5-Mod, CS6-Mod, CS7-Mod and CS8-Mod views show the modeled aDcp velocity magnitude contours for CS5, CS6, CS7 and CS8 respectively. Finally, CS5-Com, CS6-Com, CS7-Com and CS8-Com views show the contours of the error in percentage by comparing the modeled velocity magnitude vs. the measured velocity magnitude for CS5, CS6, CS7 and CS8 respectively

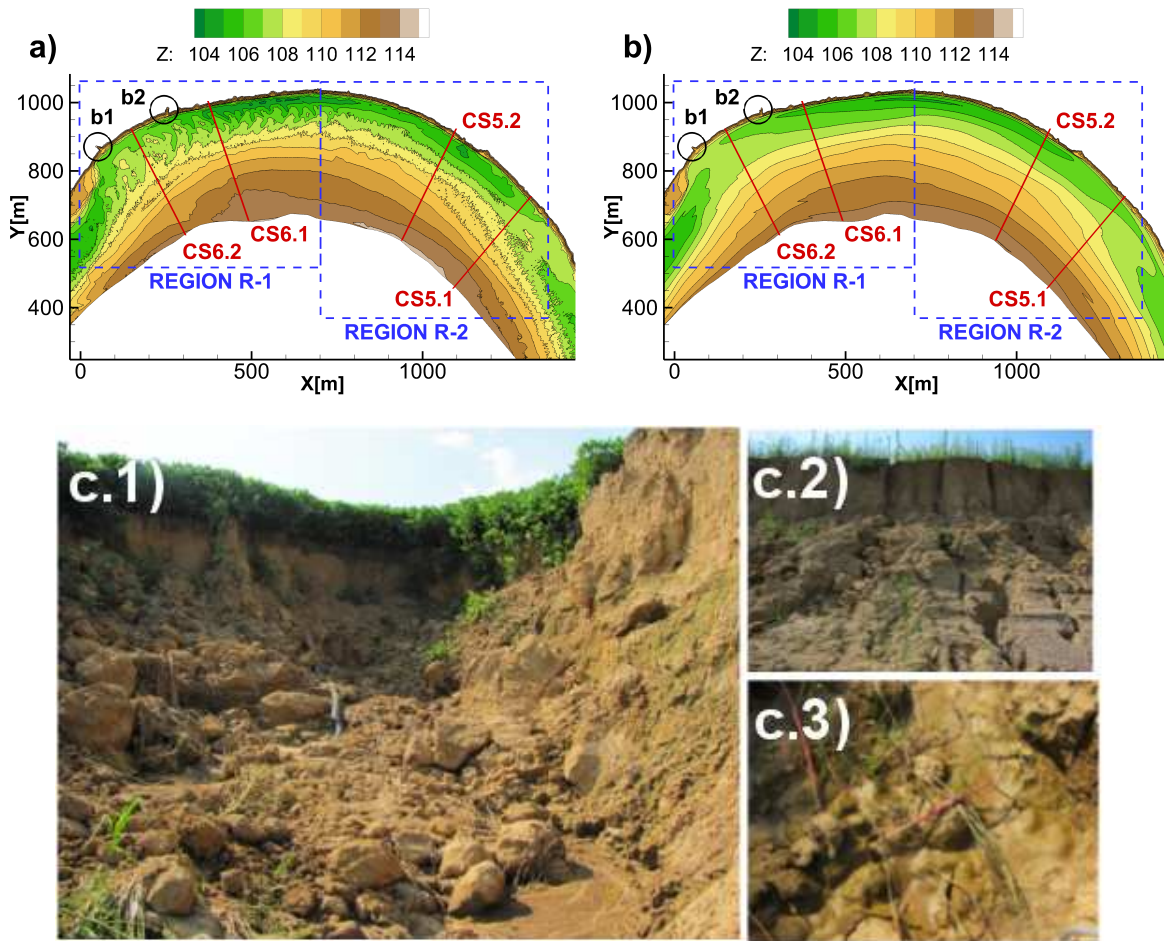


Figure 3.6: (a) C-1 (case with bed forms) bed morphology and location of velocity transects for secondary flow analysis. Bank cavities are circled and labeled as b1 and b2. (b) C-2 (case without bed forms) bed morphology and location of velocity transects for secondary flow analysis. Bank cavities are circled and labeled as b1 and b2. Pictures of the bank morphology found at the bank are showed in (c.1), (c.2) and (c.3). In (c.2) is shown a typical scarp, (c.2) shows the bank top on which a difference in bank slope can be seen. Finally (c.3) shows the deposited material inside one of the scarps.

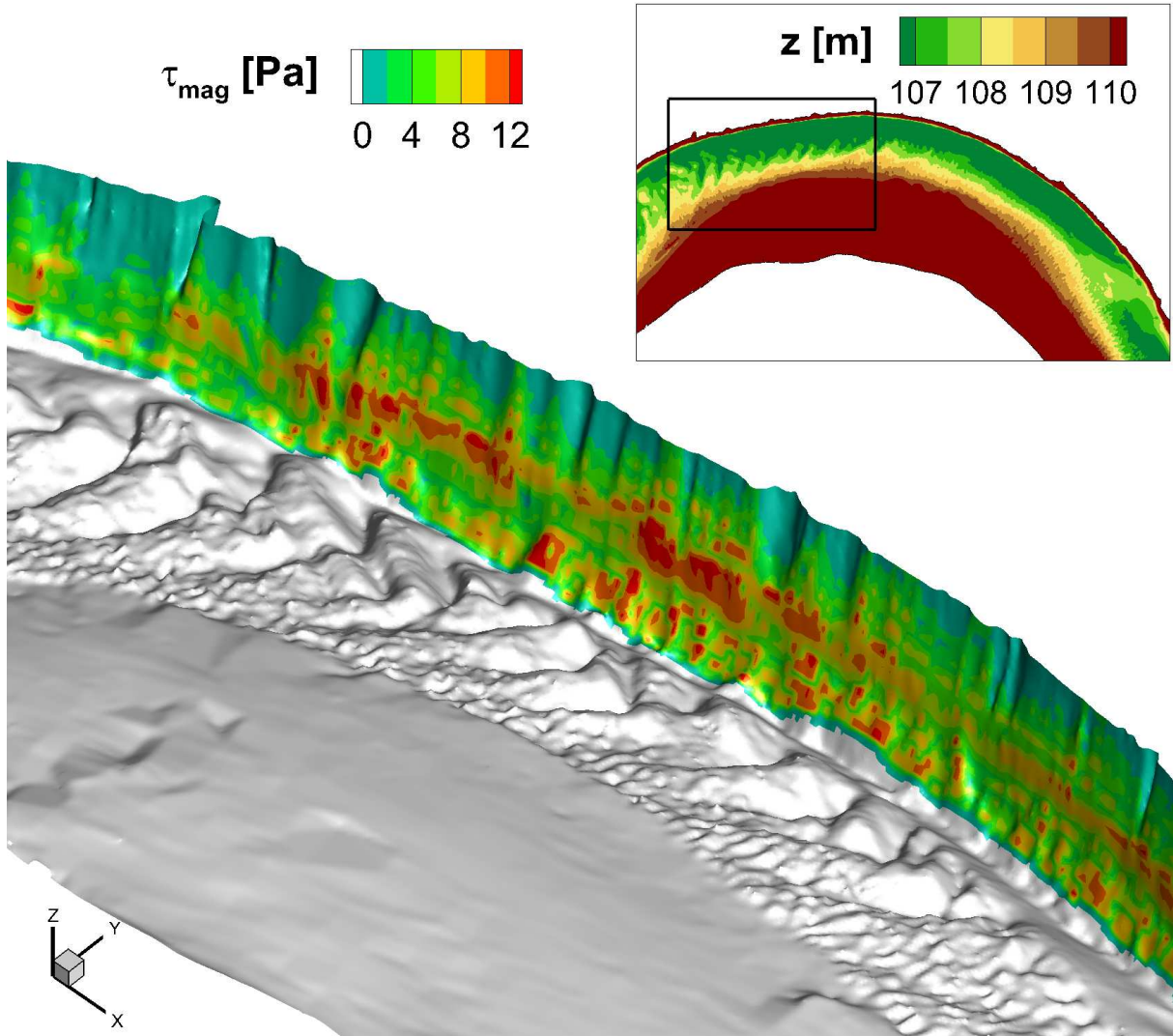


Figure 3.7: Contours of shear stress in Pa of case C-1 (case with bed forms). The top panel shows the bed elevation contours in meters.

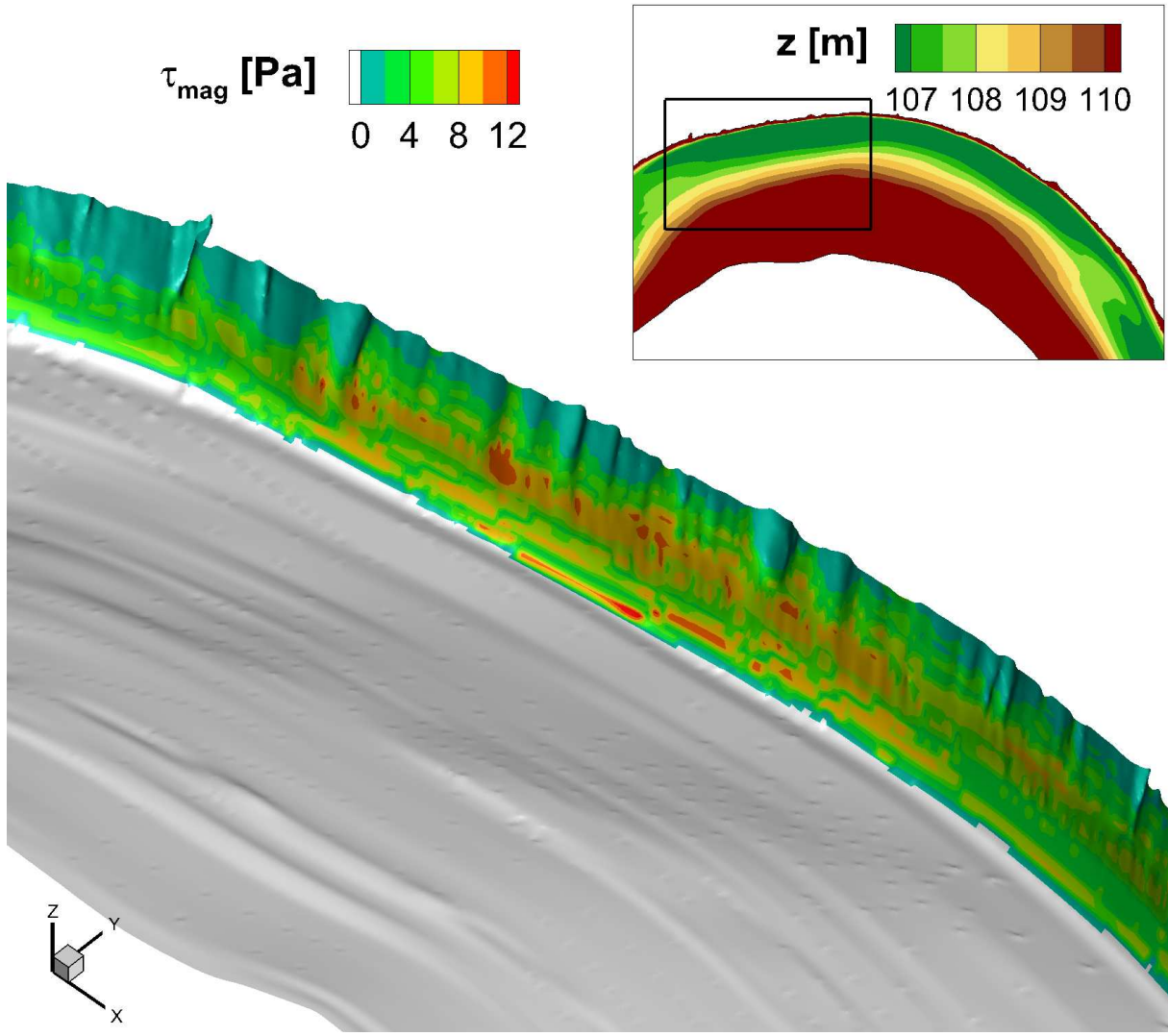


Figure 3.8: Contours of shear stress in Pa of case C-2 (case without bed forms). The top panel shows the bed elevation contours in meters.

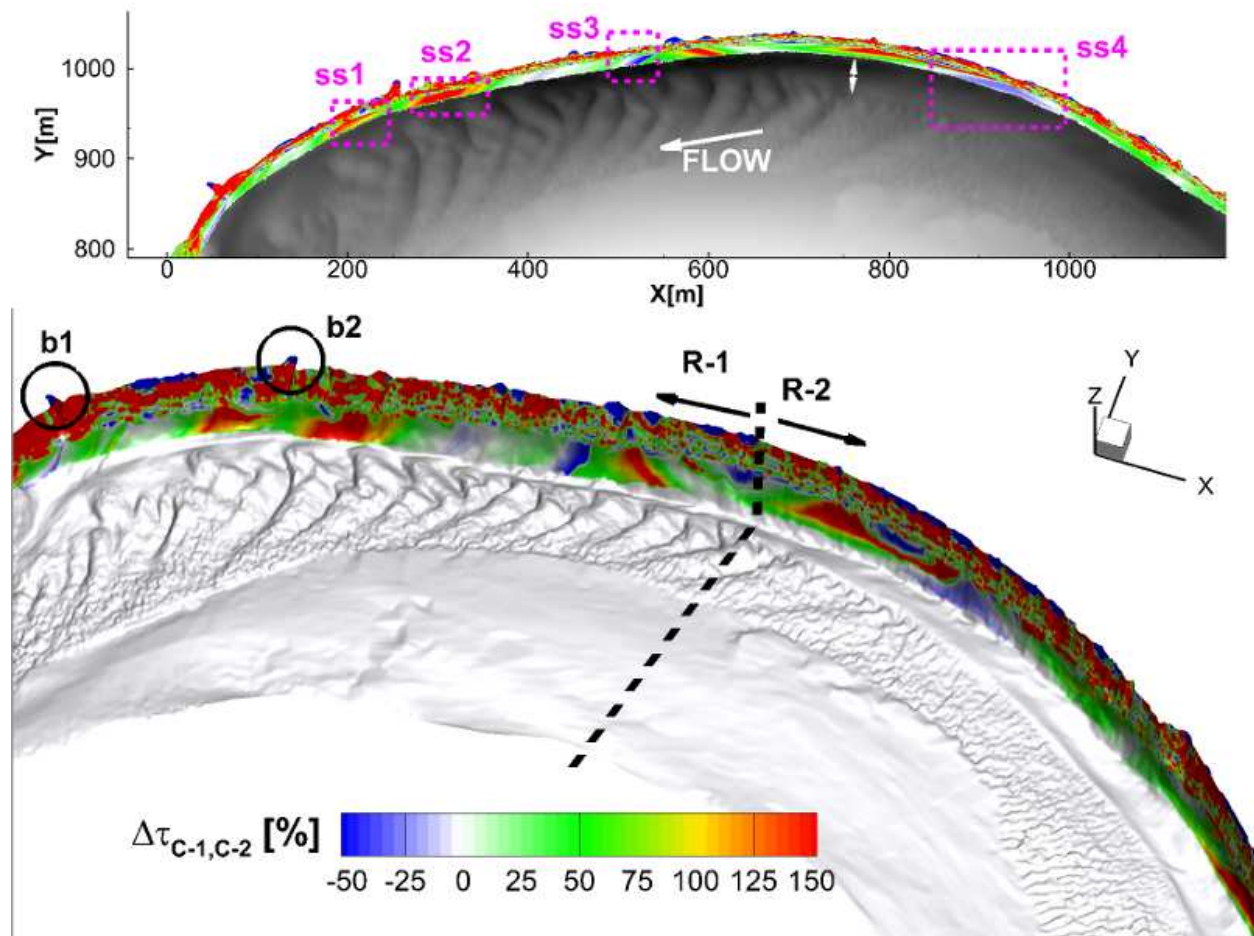


Figure 3.9: Comparison between the bank shear stress of case C-1 and case C-2. The white to red contour colors represent regions at which the shear stress is higher in C-1 than in C-2. Conversely, white to blue contour colors represent regions at which the shear stress is lower in C-1 than in C-2. The top panel shows a plan view of the bank in which boxes ss1, ss2, ss3 and ss4 were selected as patches of higher shear stress in case C-1 than in C-2 (ss1 and ss2) and lower shear stress in case C-1 and C-2 (ss3 and ss4). In the bottom panel the scarps b1 and b2 are showed as well as the regions R-1 and R-2 that represent regions of different bed forms sizes.

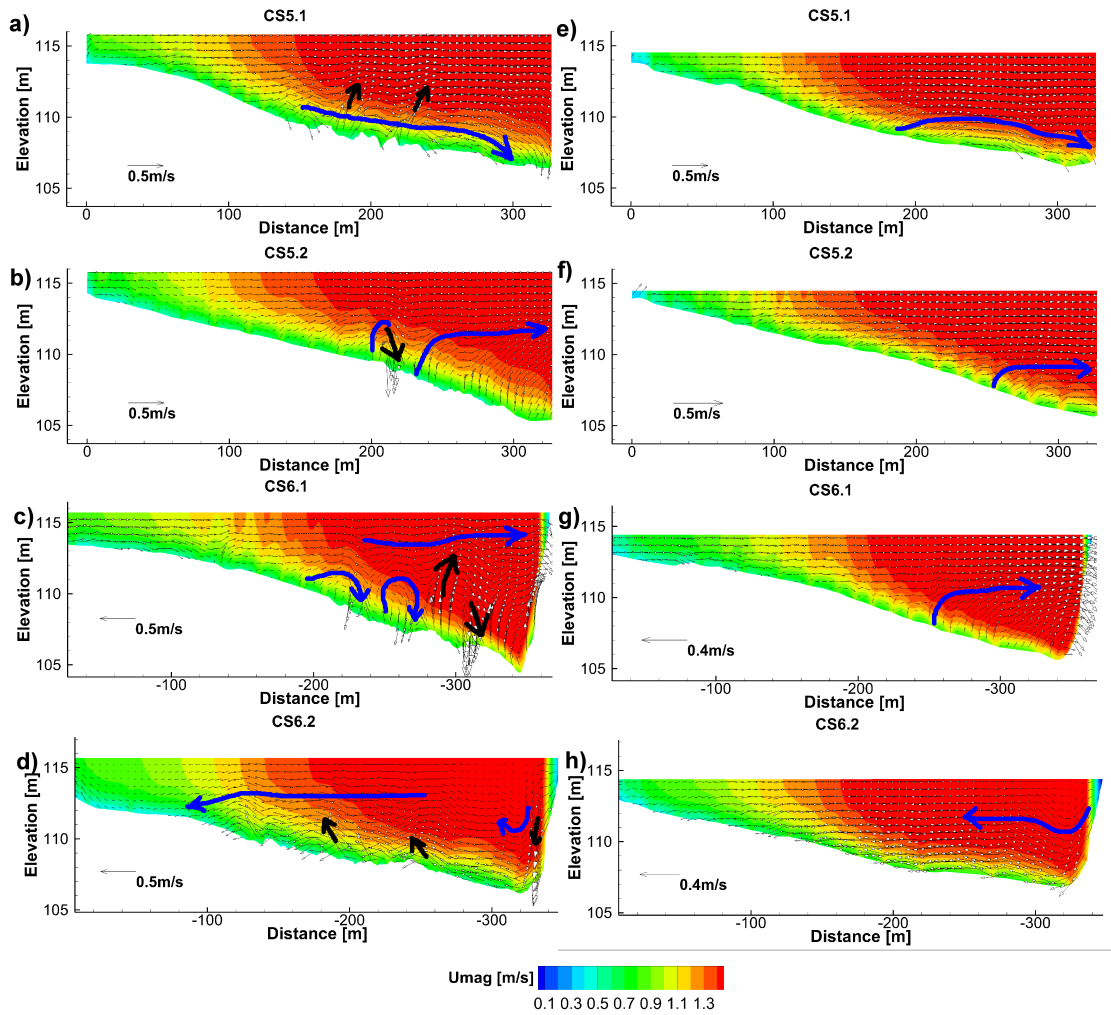


Figure 3.10: Velocity magnitude contours and vectors for C-1 ((a) to (d)) and C-2 ((e) to (h)) at CS5.1, CS5.2, CS6.1 and CS6.2. CS5.1 and CS5.2 are located in region R-2 (smaller bed forms region) and CS6.1 and CS6.2 are located in region R-1 (larger bed forms region). The blue arrows show the recirculation cells of the main flow whereas the black arrows show the upward and downward velocity patches due to the bed forms.

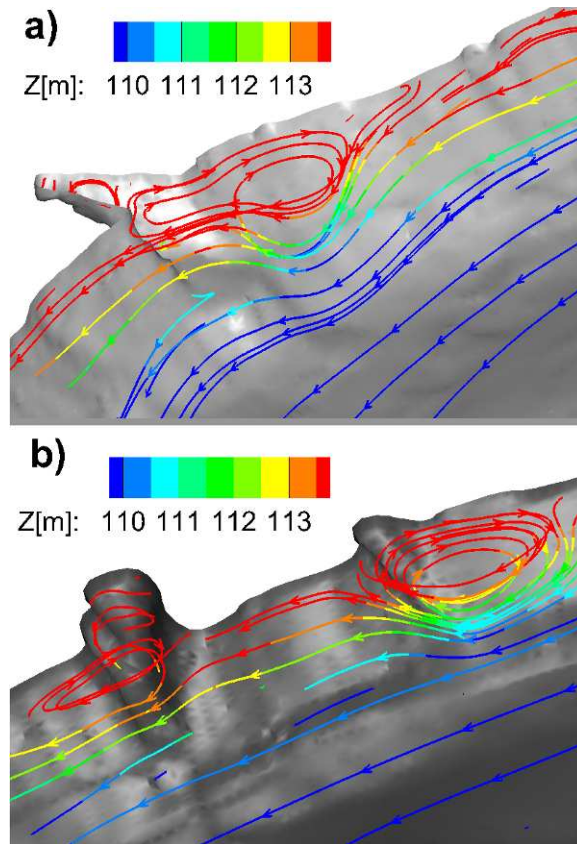


Figure 3.11: Streamlines for case C-1. The streamlines are colored by elevation for (a) scarp b1 and (b) scarp b2.

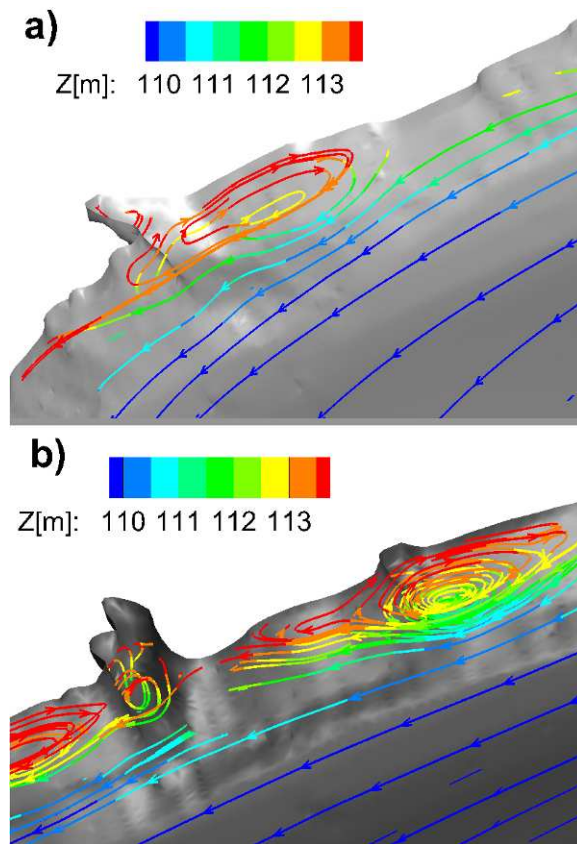


Figure 3.12: Streamlines for case C-2. The streamlines are colored by elevation for (a) scarp b1 and (b) scarp b2.

4.0 HIGH RESOLUTION ANALYSIS OF THE FLOW STRUCTURE MODULATION DUE TO BED FORMS

From past studies [109, 57, 144, 24, 185, 187], it has been observed that the shape of the river bed presents periodic irregularities that can be classified as dunes or ripples according to their size. These dunes and ripples, hereinafter called also bed forms, significantly influence the entrainment, transport and deposition of sediments in river channels. A very interesting feature during the transport and deposition process is the superimposition and subsequent amalgamation of ripples over dunes. [24],[106], and [66] showed that bed forms that are evolving from the superimposed condition to amalgamated bed forms greatly modify the flow field structure. Thus, the knowledge of the dynamics of bed forms has a great importance in the geophysical processes of any natural river or stream [5]. One of the important features that can be characterized by understanding such structures is the approximation of the mean water depth at different times from the sedimentary record [142]. Regarding to the influence of the bed forms on the flow field, [7] described that bed forms produce a modification on the natural secondary flow of a bend. He also states that the shear stresses exerted on the banks due to bed form progression are higher than conditions without bed forms, thus resulting in an increase of 50% on sediment transport due to an increased fluvial erosion rate.

According to [76], four types of creation and destruction of dunes are observed: dune splitting, dune combination, dune diminution and dune creation. Herein, the flow field of the dune combination process called amalgamation is analyzed. It has been demonstrated that the mean and turbulent flow changes distinctly as bed forms amalgamate [24]. Moreover, [106] have described the connection between evolving topography, turbulence and sediment transport by performing experiments with interaction of bed forms. Most of the past studies have focused in the development of the turbulent coherent structures over the dunes [187,

163], and very little has been done to explain the effect of the amalgamation process into the hydrodynamics (except [66, 65]). An important conclusion from [66, 65]’s work is that “the presence of a smaller bed form superimposed on the stoss side of a ripple at the ripple-dune transition produces higher levels of turbulence intensity, turbulent kinetic energy and Reynolds stresses than either over ripples or the amalgamated dune bedstate.”

Turbulent coherent structures are vortex features that present different sizes and locations in time [163]. Since these coherent structures can change the morphology of bed forms, it is important to measure the effect quantitatively by means of laboratory measurements or numerical modeling. However, it is known that due to limitations to obtain spatially resolved instantaneous flow data on experimental and field measurements [180], this characterization is quite challenging. Numerical simulations can overcome this problem by providing instantaneous parameters that can be spatially or temporal resolved to have a better insight of the physical phenomenon. [180] described that conclusions based on experimental measurements cannot be made to explain the role that the turbulence plays in the initiation of bed forms. On the other hand, it has been demonstrated that the sediment transport is enhanced by the variation of the stresses produced by turbulent coherent structures near the bed. The bursting of these structures produce the change in the flow field that allow the re-suspension of sediment and modification of the bed as well as Kelvin-Helmholtz instabilities [180, 60]. On the other hand, concerning the numerical approximations, it has been demonstrated that using large eddy simulations (LES), it is possible to model and describe the behavior of coherent turbulent structures [110].

There are known differences between bed forms observed in the field and in the lab; one important difference to mention is the lack of a recirculation zone on field bed forms in contrast to experimental fixed bed forms [32, 33]. However, despite this difference it has been proven that hydrodynamic parameters such as Reynold stresses and velocities remain similar between field and experimental cases [165]. Herein, the analysis and discussion of the results of LES for the entire amalgamation process (train of ripples, superimposed bed form stage and amalgamated bed forms stage) are presented. This can be considered as a complementary study to the work of [66] and [65] as we further provide an analysis of the water surface interaction with the bed form (upwelling and downwelling structures) as

observed by [138], streamlines' topological characterization and bursting events quantification. Further, the characteristics of the turbulent structures are described by means of the swirling strength iso-surfaces in contrast to the turbulence moments and quadrant analysis performed by [66].

4.1 METHODOLOGY

4.1.1 Hydrodynamic Governing Equations

The LES method demands an intermediate amount of computational resources, more than the Reynolds Averaged Navier Stokes (RANS) method and less than a Direct Numerical Simulation (DNS) approach. The LES methodology filters the Navier Stokes governing equations in order to resolve the intermediate and large scales and to model the small ones [120]. The hydrodynamics of the intermediate and large scales are considered local. Whereas, the behavior of the flow field for the small scales are considered universal and their effect on the large scales can be determined by some parameterization [29]. To differentiate between the large and small scales, a box filter in three dimensions is applied to the velocity field [145]. However, according to [90] the selection of the filter has little effect on the solution of the system.

The filtered Navier Stokes equations used herein are given in the equations shown below:

$$\frac{\partial \bar{u}_i}{\partial x_i} = 0 \quad (4.1)$$

$$\frac{\partial \bar{u}_i}{\partial t} + \frac{\bar{u}_i \bar{u}_j}{\partial x_j} = -\frac{1}{\rho} \frac{\partial \bar{p}}{\partial x_i} + \frac{\partial}{\partial x_j} \left[\nu \left(\frac{\partial \bar{u}_i}{\partial x_j} + \frac{\partial \bar{u}_j}{\partial x_i} \right) - \tau_{ij}^{SG} \right] \quad (4.2)$$

Where $i, j = 1, 2, 3$ describing the Cartesian coordinates, $\bar{u}_1, \bar{u}_2,$ and \bar{u}_3 are the Subgrid-scale (SGS) filtered velocities in the x_1, x_2 and x_3 direction respectively, ρ is the density of the fluid, \bar{p} is the SGS filtered pressure, ν is the kinematic viscosity and τ_{ij}^{SG} is the SGS stress tensor.

The difference between the Navier Stokes equation and the Navier Stokes filtered equation is the addition of the SGS stress tensor τ_{ij}^{SG} . The SGS stress tensor contains the fluctuations for the Subgrid-scale and is given by the following equation.

$$\tau_{ij}^{SG} = \overline{u_i u_j} - \bar{u}_i \bar{u}_j \quad (4.3)$$

In order to solve the system shown by Equations (4.1) and (4.2), a closure model was applied for the SGS stress tensor. These closure models can be categorized as algebraic models, differential sub-grid models, scale similarity models or dynamic models [47]. Among these models, the ones that better reproduce the physics of wall bounded flows, such as channels or pipes, are the differential sub-grid models and the dynamic models [47]. Thus, herein a Smagorinsky dynamic model is used. The major advantage of this model is the adjustment of the coefficient in areas near the wall where it is lowered because of the higher shear stresses.

4.1.1.1 Dynamic Smagorinsky model A major problem that has been discovered in the plain Smagorinsky SGS model is the disadvantage of considering the SGS viscosity in regions very close to the wall where the flow is no longer turbulent [110]. To address this problem a dynamic model that allows the Smagorinsky constant C_s to vary in time and space was needed. A dynamic model could be considered as a procedure instead of a model since it can be applied to any of the algebraic models, scale similarity or differential SGS models [47]. It assumes that the behavior of the resolved scales is similar to the SGS scales [47]. In order to differentiate the zones close to walls (or zones of high shear stress) and the rest of the domain, a test filter is defined. The test filter is denoted as $\tilde{\Delta}$ and it is equal to double size of the original filter width ($\tilde{\Delta} = 2\Delta$). If this test filter is applied to the Filtered Navier Stokes equations (4.2), then a new sub-grid stress T can be modeled as shown by Equation (4.4).

$$T_{ik} = \widetilde{u_i u_k} - \tilde{u}_i \tilde{u}_k \quad (4.4)$$

At this point, the Germano identity shown in the following equation is used to calculate the model coefficients needed for the method.

$$L_{ik} = T_{ik} - \tilde{\tau}_{ik} \quad (4.5)$$

Where L_{ik} is the Leonard stress ($L_{ik} = \widetilde{\widetilde{u_i u_k}} - \widetilde{u_i u_k}$) and $\tilde{\tau}_{ik}$ is the test filter stress. A detailed explanation for the use of the Germano identity to obtain the model coefficients can be found in [47]. In summary the model coefficient is given by the following equation.

$$C_d^2 = \frac{\langle L_{ij} M_{ij} \rangle}{\langle M_{kl} M_{kl} \rangle} \quad (4.6)$$

$$\text{Where } M_{ij} = 2\Delta^2 \left(\overline{|\tilde{S}| \tilde{S}_{ik}} - \left(\frac{\bar{\Delta}}{\Delta} \right)^2 \overline{|\tilde{S}| \tilde{S}_{ik}} \right).$$

4.1.2 Computational Setup

Three cases were considered, a periodic train of simulated ripples (RUN I), a bed form superimposed on one of the simulated ripples (RUN II) and a complete amalgamated bed form over the simulated ripples representing a dune-size larger bed form (RUN III). For all the cases a water depth, \bar{d} of 0.10m was used. The geometry of the cases was based on the work of [65]. Thus, for RUN I each ripple had a leeside slope angle of 25° , a wavelength, λ_L , of 0.30m and a crest height, h_s of 0.015m. For RUN II, a smaller bed form was superimposed with a wavelength, λ_s , of 0.10m and a height, h_s , of 0.01m (see Figure 4.1). For RUN III, an amalgamated bed form with a bed form ratio, $\bar{d} : h_s$, of 4.00 was used. All the cases considered a flume with a width of 300 mm, a height of 200 mm and a length of 900 mm. For all of these cases, three complete bed forms were located in the computational grid and the analysis was performed in the middle bed form. The simulations were carried out using structured computational grids. The grid spacing was selected following [163]'s configuration. This spacing is determined using the wall units shown in the following equation [145].

$$x^+ = \frac{u^* x}{\nu}, \quad y^+ = \frac{u^* y}{\nu}, \quad z^+ = \frac{u^* z}{\nu} \quad (4.7)$$

where x^+, y^+, z^+ are the wall units, ν is the kinematic viscosity and u^* is the shear velocity.

As [145] states on wall bounded flows the domain can be divided in viscous wall region ($z^+ < 50$) and outer layer ($z^+ > 50$). Within the viscous wall region it is located the viscous sublayer $z^+ < 5$. Then the grid spacing is calculated from the wall units distance expressed as $\Delta x^+ = \frac{u^* \Delta x}{\nu}$, $\Delta y^+ = \frac{u^* \Delta y}{\nu}$, $\Delta z^+ = \frac{u^* \Delta z}{\nu}$.

Thus $\Delta x^+ \approx 20$ in streamwise direction, $\Delta y^+ \approx 19$ in spanwise direction and $\Delta z^+ \approx 1$ near the bed form surface. The grid spacing in the y and z direction presents the finest value at the walls and at the water-air interface ($z \approx 100\text{mm}$). An example of the computational grid (around 11 million of nodes) for the RUN II (superimposed bed forms) is shown in Figure 4.1. The CFD model used for the simulations was OpenFOAM [141] which is an open source code that treats the two fluid stages (water and air) with a Volume of Fluid (VOF) approach. The algorithm used to solve the Navier Stokes equations was the Pressure Implicit with Splitting of Operators (PISO) algorithm. The simulations were run in parallel using 64 cores with a total computing time of 27,000 hours per case approximately. The computing time is distributed among the 64 cores which results in about 18 days of computing time per case.

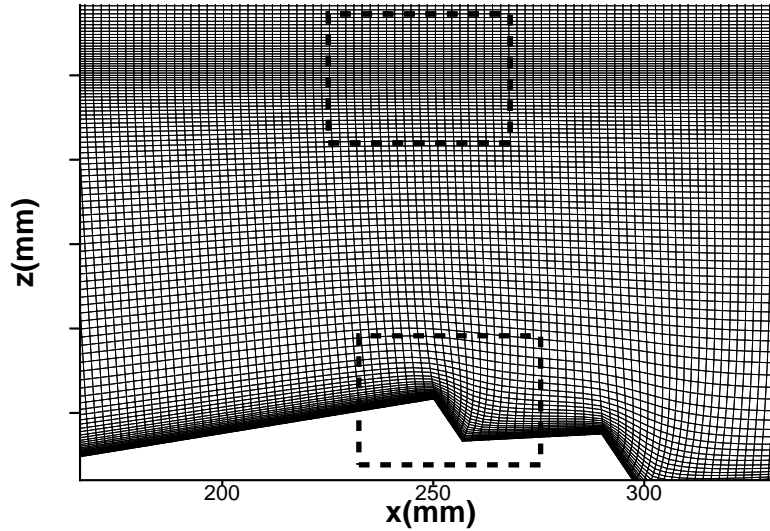


Figure 4.1: Computational grid for RUN II. The mesh has been refined at the water-air interface and near the wall. The dashed rectangles show the refined regions for the interface and near the wall.

4.1.3 Boundary and Initial Conditions

Boundary and initial conditions were given for the velocity, pressure, SGS dynamic viscosity, turbulent kinetic energy (TKE) and the fluid fraction function (α). The fluid fraction function is used in the VOF method to track the fluid contained in each cell ($\alpha = 1$: water, $\alpha = 0$: air, $\alpha = 0.5$: interface). The equation to be solved for the fraction function is a scalar transport equation given by the following equation.

$$\frac{\partial \alpha}{\partial t} + u_i \frac{\partial \alpha}{\partial x_i} = 0 \quad (4.8)$$

The inlet boundary condition for the velocity was a logarithmic profile with initial random fluctuations following the procedure described by [110]. The logarithmic profile is given by the following equation.

$$u = \frac{u^*}{\kappa} \ln \left(\frac{9.05z u^*}{\nu} \right) \quad (4.9)$$

where u^* is the shear velocity (m/s), z is the vertical direction coordinate (m), ν is the viscosity of the water ($10^{-6} m^2/s$) and κ is the von Kármán constant (0.41).

In order to have a flow rate equal to the flow rate reported in each case according to [66] and [65], the shear velocity to be used in equation (4.9) was calculated. This shear velocity is different from the one reported by [65] since it is not a spatial average on the entire domain but a value used to get the same inlet flow rate of the experimental cases using equation (4.9). The parameters for equation (4.9) are presented in Table (4.1).

Table 4.1: Logarithmic inlet profile parameters, where \bar{u} is the streamwise depth averaged velocity (m/s), u^* is the shear velocity (m/s) and Q is the flow discharge (m^3/s)

RUN	I	II	III
u^*	0.0182	0.0182	0.0177
\bar{u}	0.372	0.374	0.363
Q	0.0111	0.0112	0.0108

The walls were simulated as a no-slip boundary condition for velocity. At the outlet, different patches were created for the outlet of the air and the outlet of the water. Addition-

ally a wall simulating a weir was placed in order to preserve the water surface elevation for average flow and the pressure distribution. The pressure for the water patch at the outlet was a zero Dirichlet boundary condition ($p = 0$) while, for the rest of the variables, a zero gradient was considered for the water and air patches. Thus, the outlet boundary condition works as a Poisson equation, in which the pressure is calculated at the outlet. In order to let the flow exit at the top region a boundary condition that switches the zero gradient ($\frac{\partial u}{\partial x} = 0$) and zero value ($u = 0$) according to the direction of the velocity was used. For the pressure, a Dirichlet boundary condition that represented the total pressure ($p + \frac{1}{2}\rho u^2$) was used. The initial conditions were obtained from a previous simulation in a coarser mesh. The coarser mesh simulation was run for 100 seconds in only one of the cases (RUN I). Next, the results were mapped to be used as input for the three cases.

4.2 RESULTS, ANALYSIS AND DISCUSSION

4.2.1 Validation of the LES modeling

For the validation, only comparisons for RUN II (superimposed bed forms) are described, since this case presented a more complex geometry and flow structure. Thus, Figure 4.2 shows the modeled average streamwise velocity for RUN II. The contours show a region of high velocity and one where the flow recirculates (negative values).

The computed streamwise average velocity and the computed Reynolds stresses were compared with the experimental data as shown by Figures 4.3 and 4.4, respectively. Overall the streamwise average velocity values are in agreement with the experimental data at the zone near the bed (inner layer). However, it can be seen that in the numerical results there is a trend to exceed the average velocity obtained experimentally at zones above the outer layer ($z > 30\text{mm}$) and between cross sections 280mm to 364mm, which is associated with the effect of the air-water interface modeled using the VOF method. On the other hand, the results for Reynolds stresses showed similar patterns as those from the measurements. Some differences are observed near the inner layer between cross sections 334mm and 364mm.

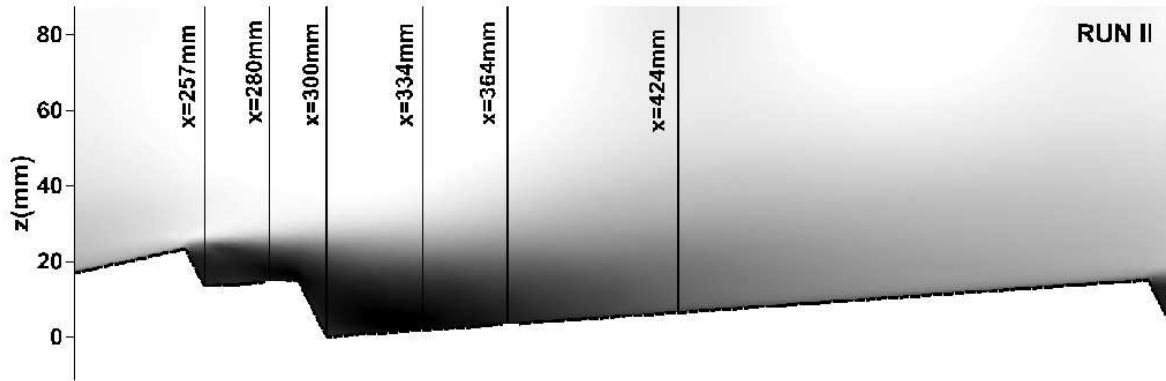


Figure 4.2: Average streamwise velocity \bar{u} (m/s) for the three cases. The contours show only the water region portion. Six cross sections are used for comparison against experimental measurements.

4.2.2 Flow field structure

In contrast to previous studies such as [163], [188] or [75], the RUN II involves two crests. Figure 4.5 shows the average streamlines for the three cases. It can be seen that the nodes, saddle, and half-saddle topology signatures described by [88] are presented in RUN I and RUN II, while RUN III shows only nodes and saddles. The reattachment length increases by about 75% once the bed forms are amalgamated as shown in Figures 4.5 (a), (b) and (c).

According to the streamlines shown in Figure 4.5 and the topology description given by [88], it is observed that for RUN I, a single saddle is formed. On the contrary, RUN II and RUN III presented two saddles. For all the cases the reattachment point is defined by a half-saddle structure. The saddles separate the recirculation zone. The center of each recirculation zone is described by a node for all the stages. Thus, for the train of ripples stage (RUN I) we have three recirculation zones of different sizes. The largest one is located closer to the reattachment point. For the superimposed bed forms stage (RUN II) four recirculation zones are observed. The largest one is located again closer to the reattachment point. For the amalgamated bed forms stage (RUN III) three recirculation zones are observed. However, two of these recirculation zones are very close to each other and can be considered as one.

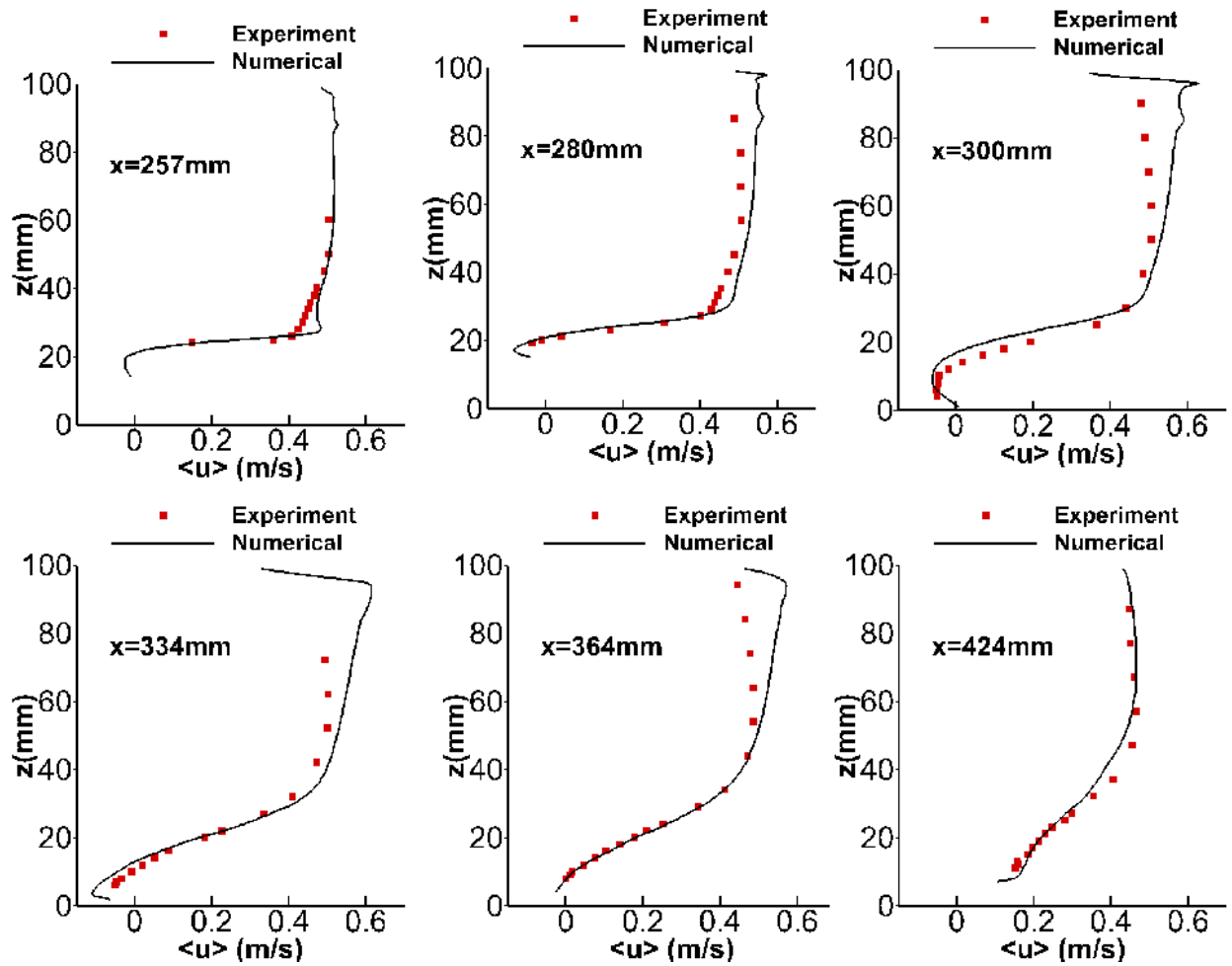


Figure 4.3: Experimental and numerical results for the average streamwise velocity (m/s) for selected cross sections in RUN II. Experimental results were obtained from a vertical profile on case RUN II in [65].

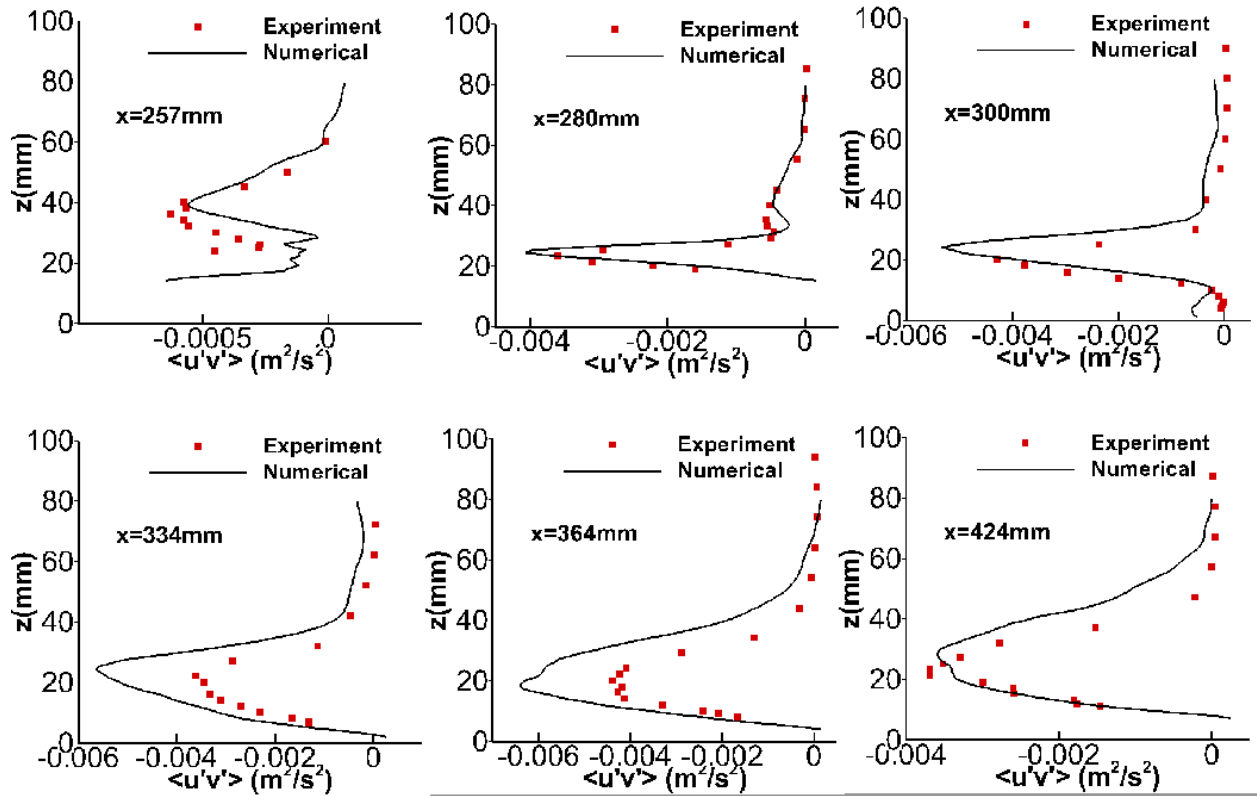


Figure 4.4: Experimental and numerical results for the Reynolds stresses $\langle u'v' \rangle$ (m^2/s^2) for selected cross sections in RUN II. Experimental results were obtained from a vertical profile on case RUN II in [65].

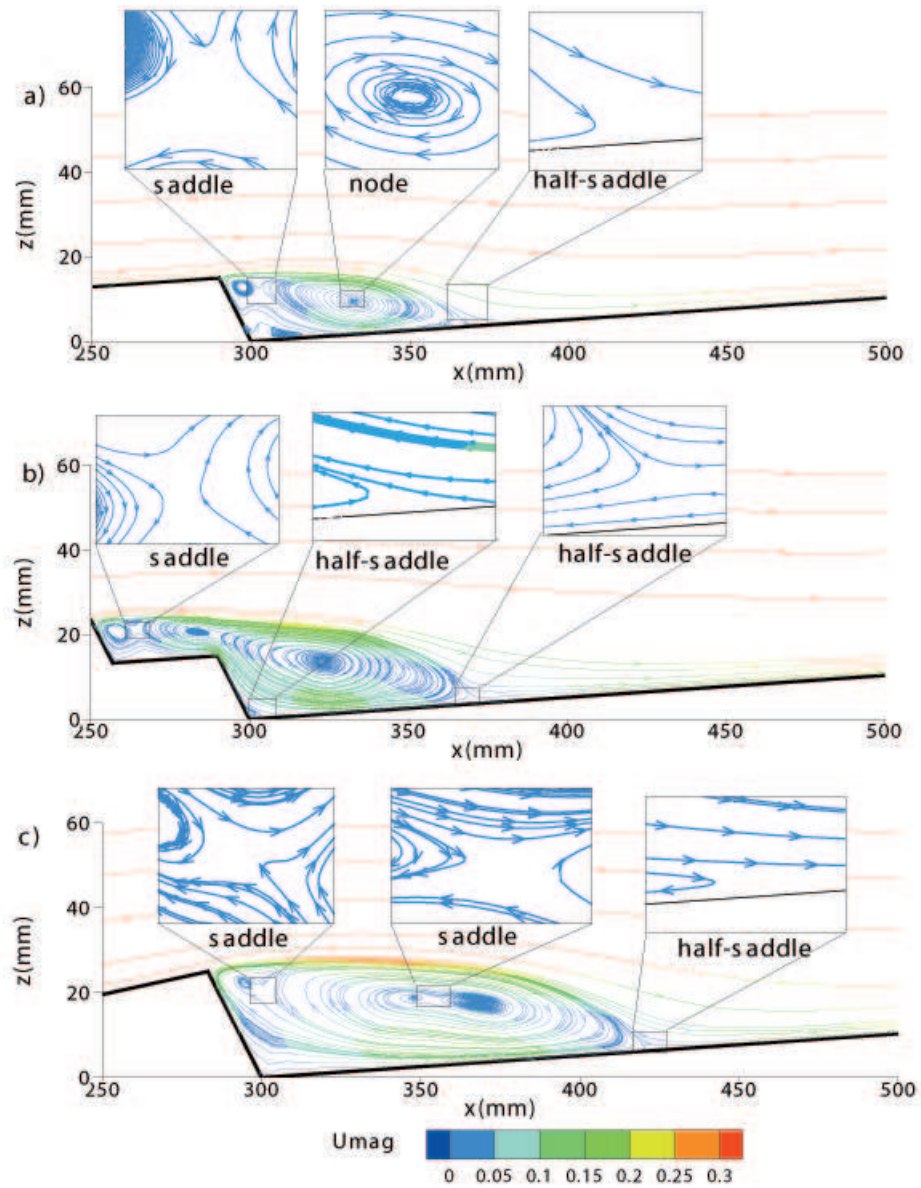


Figure 4.5: Average flow streamlines colored by average velocity magnitude (m/s) for a) RUN I b) RUN II and c) RUN III. The saddles, nodes and half saddles structures are shown for RUN I, RUN II and RUN III respectively. The reattachment point is located at a half-saddle for all the cases.

Therefore, it can be said that RUN III is composed by two main recirculation zones. For RUN II, one of the saddles is located above the lower crest separating the largest recirculation from the two other recirculation zones in between the crests. Although, these results are for a fixed bed model, some preliminary conclusions related to the sediment transport can be done based on the flow field. Thus, it is due to this separation in the recirculation zone that suspended sediments might not be trapped in the vortices and thus deposited on the stoss side of the downstream bed form. Additionally, this mechanism produces the migration of the superimposed ripple by transporting sediment grains from the ripple's stoss side onto the dune's stoss side. At the same time, deposition processes are occurring at the leeside of the larger and smaller bed form until a complete amalgamation can be reached.

From a different point of view, the amalgamation process starts with two recirculation zones that are stretched upstream when the bed forms are superimposing. That is why the resulting topology at RUN II is two small recirculation zones between crests and one main recirculation zone downstream of the largest bed form crest. Next, the migration of the small bed form on the larger bed form (amalgamation) pushes the stretched recirculation zone back into a similar topology as in RUN I but with larger dimensions. In other words, the amalgamation process will produce an oscillating topology in which the sizes of the recirculation zones will be determined by the location of the superimposed bed form crest.

4.2.3 Interaction ripple-dune structure and turbulence

To understand the interaction of the ripple-dune structure with turbulence, a visualization of the velocity fluctuations and invariants of the velocity gradient polynomial [89, 80] was performed. Figure 4.6 and Figure 4.7 depict the turbulent coherent structures using the swirling strength parameter ($\lambda_{ci} = 25$) for the three cases at a selected time step. The swirling strength is defined as the imaginary part of the eigenvalue of the velocity gradient (∇U) [11, 12]. For more information regarding to the definition of this parameter the reader can refer to [11, 12].

These turbulent coherent structures, due to their similarities at different scales, are given by fractal laws as stated by [88]. The contours in Figure 4.6 are colored by value of elevation

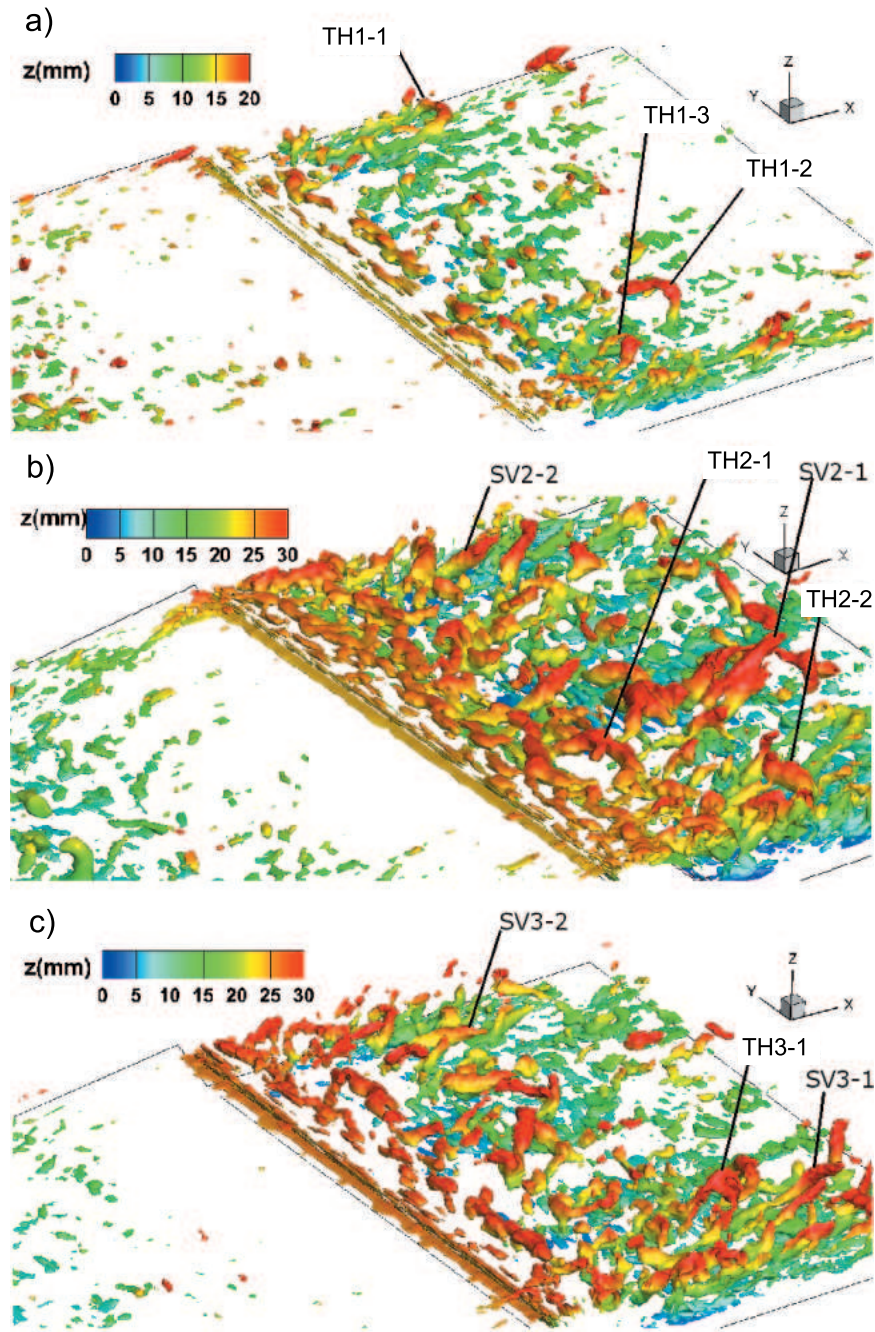


Figure 4.6: Swirling strength isosurfaces with elevation contours (mm) for a) RUN I, b) RUN II and c) RUN III.

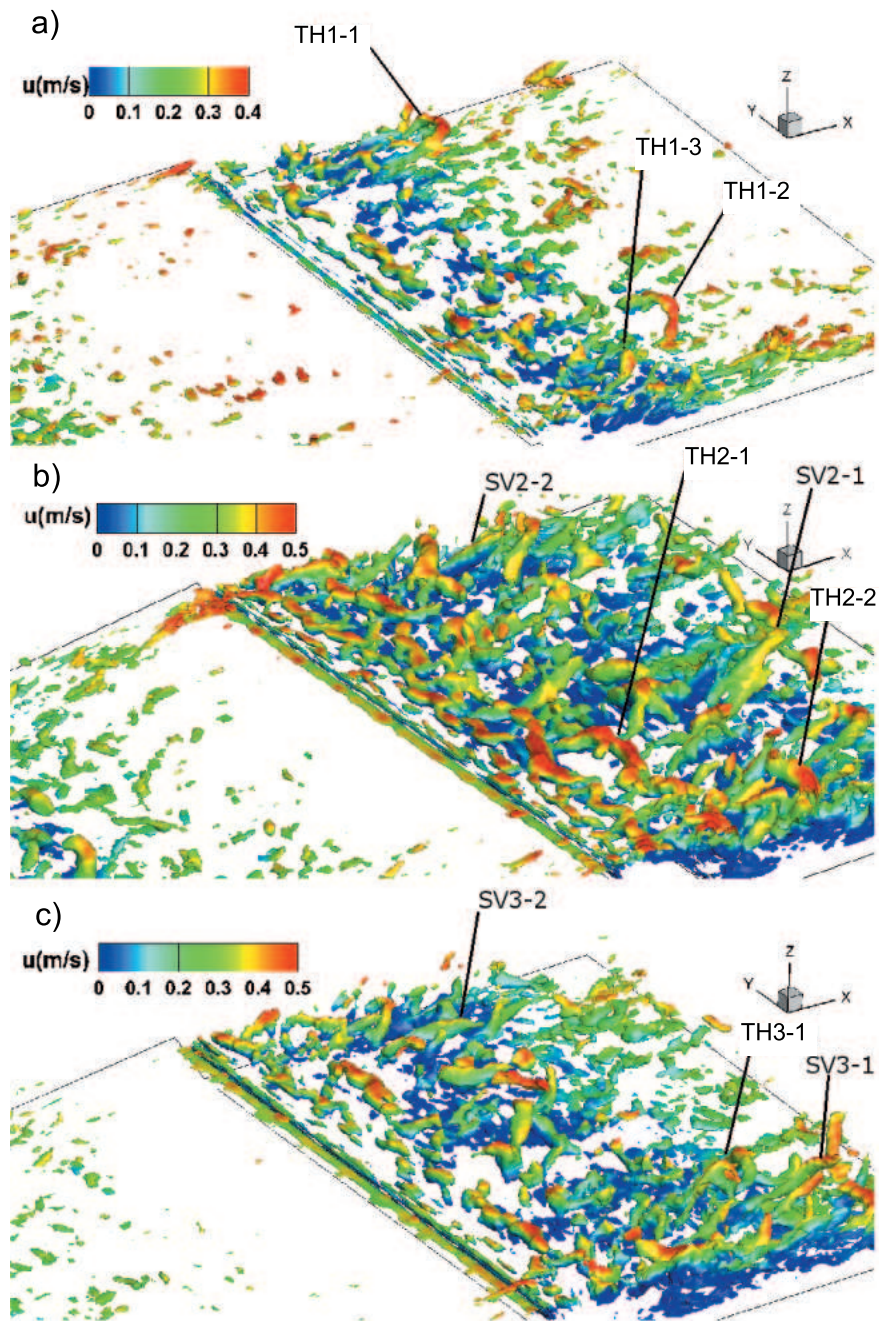


Figure 4.7: Swirling strength isosurfaces with velocity contours (m/s) for a) RUN I, b) RUN II and c) RUN III.

to show the three dimensional shape of the structures and by velocity magnitude in Figure 4.7. Based on the swirling strength isosurface visualization, it seems that the turbulence Horseshoes Vortices (THV) [85, 61] are created downstream of the bed form's leeside but not observed at the vertical plane located at coordinate $y=0$. Instead the THV tend to appear toward the side walls in periodical bursts. The turbulent structures present a more chaotic behavior along the amalgamation process (from RUN I to RUN III). The THV are labeled as TH1-1, TH1-2, TH1-3 for RUN I, TH2-1, TH2-2 for RUN II and TH3-1 for RUN III. On the other hand, the streamwise roll vortex structures are labeled as SV2-1, SV2-2 for RUN II and SV3-1 and SV3-2 for RUN III. The distribution of these structures presents a more chaotic behavior along the amalgamation process. It is observed in RUN I that the streamwise rolls are not as noticeable as those in RUN II and RUN III. By contrasting the contours of elevation and velocity from Figures 4.6 and 4.7, it is clear that the majority of the low elevation structures coincides with the low speed structures, also known as low speed streaks [161, 11, 15]. For the case of RUN II, the range of velocity for the streamwise rolls SV2-1 and SV2-2 (0.2 to 0.3 m/s) is lower than the upper part of the THV such as TH2-1 and TH2-2 (0.4 to 0.5 m/s). However, for RUN III, the values of velocities for TH3-1 and SV3-1 (0.2 to 0.45m/s) are almost in the same range in contrast to the SV3-2 structure, which is between 0.1 to 0.3 m/s. The latter is again related to the height of the structures, thus showing that the higher the coherent structures, the faster they are. This plays an important role on the rate of sediment transported to the outer layer. The streamwise rolls are a consequence of broken THV, thus, the sequence is characterized starting from low speed streaks to high velocity THV, then to low speed streamwise rolls. The streamwise rolls reduce the velocity compared to the THV due to the energy that is lost when a THV breaks. Finally, the height of the structures for the three cases is approximately 15% to 25% of the average water depth of 100mm. This height is considered to be related to the bursts that transport the sediment from the viscous and inner layer to the outer layer.

4.2.4 Interaction bed form and water surface elevation

In Figure 4.8, the spanwise instantaneous velocity fluctuations are shown. The vertical inclined flow structures reported by [163] were encountered for the three cases. These inclined structures alternate between high and low spanwise instantaneous velocities in the longitudinal direction. The angle increases slightly with respect to the horizontal as the amalgamation process progresses (RUN I to RUN III).

These structures are related to the location and scope of the so-called “ejection rollers” due to a THV instability. These “ejection rollers” reach the water surface creating the well-known kolk-boil structure. These kolk-boil structure generate the up- and downwelling water surface shape that is shown in Figure 4.9 for the three cases (undulations, [18]). The deformation of the instantaneous water surface (Figures 4.9) is strongly associated to the bursting events. The instantaneous water surface presents small perturbations with respect to the average water surface, where the downwelling and upwelling structures are well defined. The difference in elevation between the upwelling and downwelling structures for RUN I is in the order of 1 to 2mm, whereas for RUN II and RUN III these fluctuations are approximately greater than 5mm. For RUN I, the downwelling structure is located exactly above the single crest, while for RUN II, it is located at the lowest crest. For RUN II, the highest crest influences the rise of the water surface creating an upwelling structure above it. For RUN III, the downwelling structure is located downstream of the crest of the bed form. Thus, it is shown that the amalgamation process modulates the perturbations in the water surface elevations and therefore the upwelling and downwelling structures.

4.2.5 Shear stress, bed sediment transport and bursting events

Several researchers [63, 24, 144, 31, 160] stated that the bed shear stresses play an important role in the bed sediment transport and the bed evolution. The amalgamation process is strongly related to the sediment transport processes which is related to the bed shear stress, thus a characterization of the spatial variability of the bed shear stresses is required. Figure 4.10 shows the bed shear stresses for all cases. A region of high shear stress denoted as HSS and a region of low shear stress denoted as LSS are observed. The LSS region is located

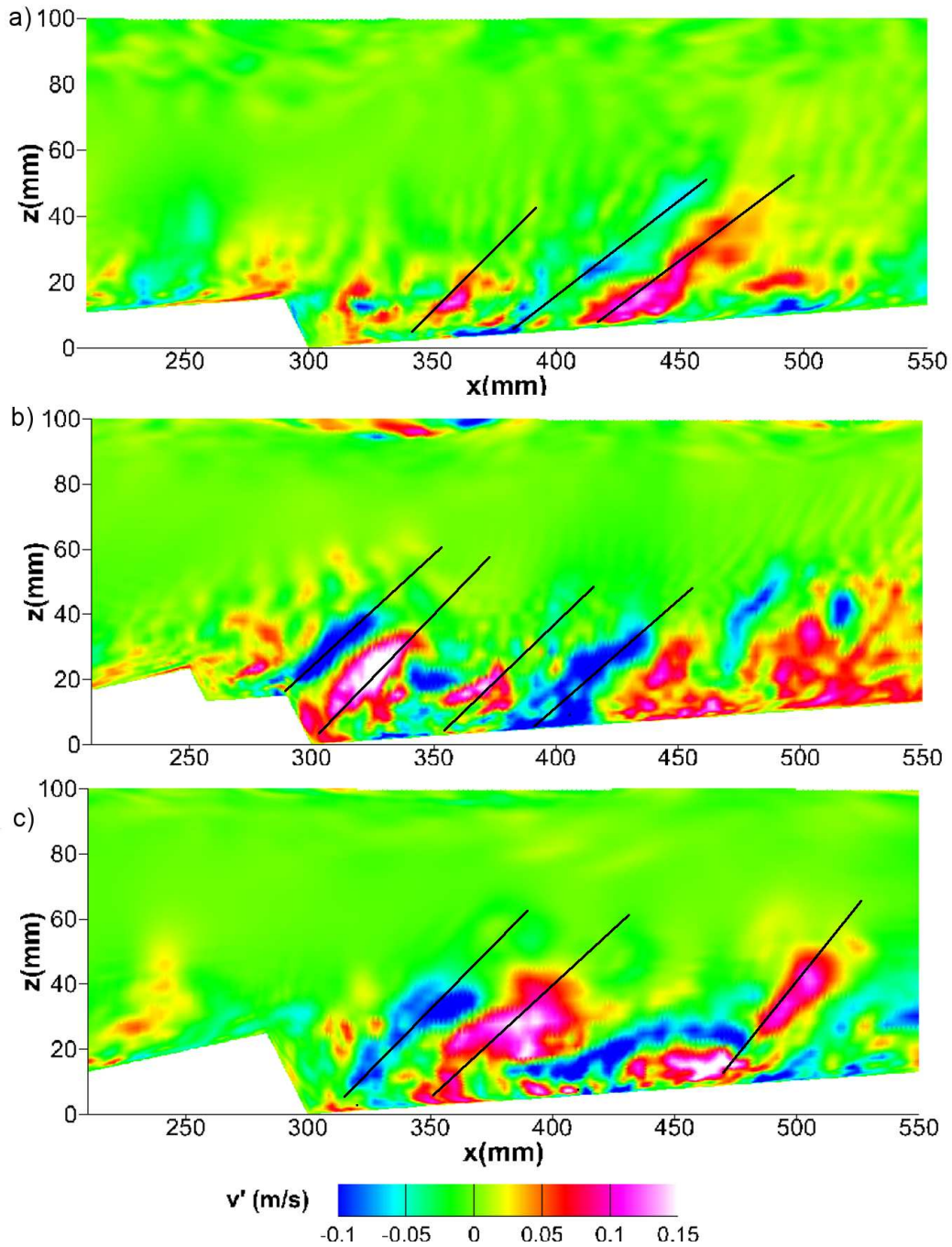


Figure 4.8: Spanwise velocity fluctuations contours for a plane located at $y = 0$ a) RUN I b) RUN II and c) RUN III.

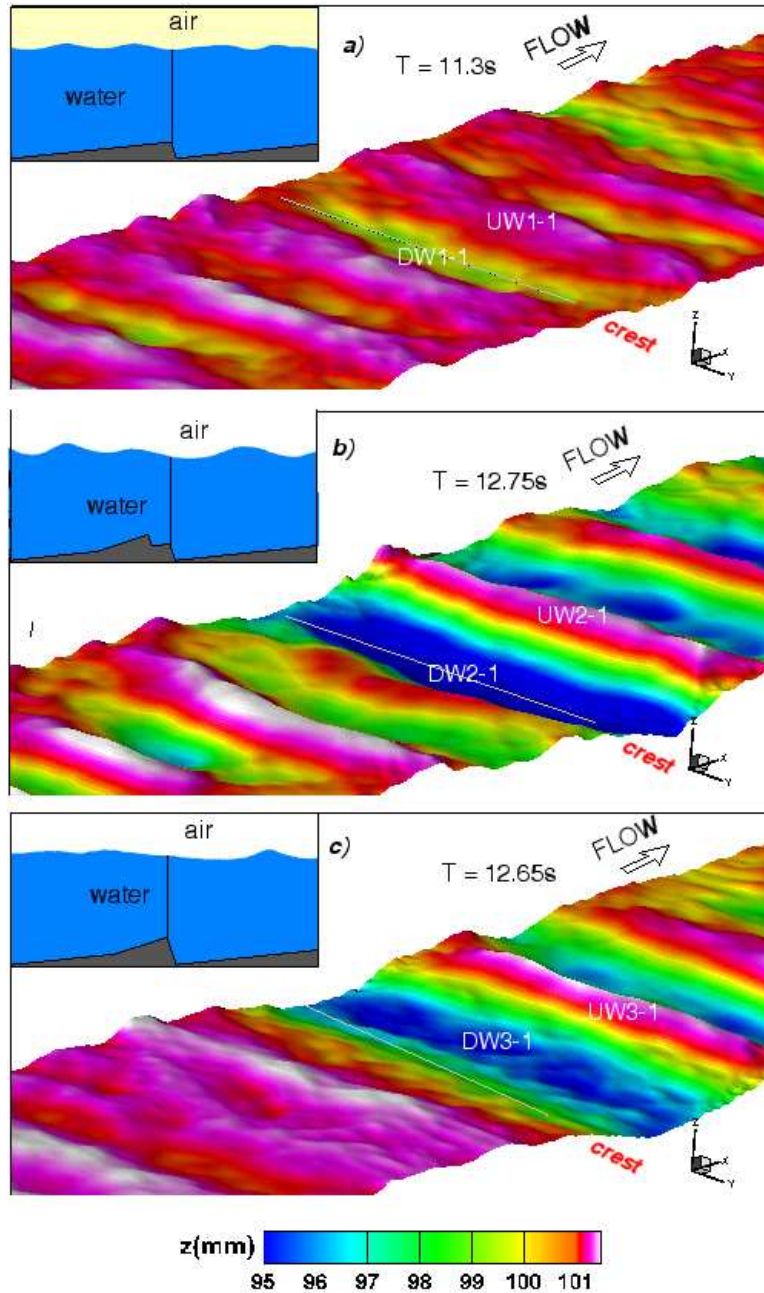


Figure 4.9: Instantaneous water surface at selected time steps for a) RUN I b) RUN II and c) RUN III. The upwelling structures on the water surface are denoted as UW1-1, UW2-1 and UW3-1 for RUN I, RUN II and RUN III respectively. The downwelling structures on the water surface are denoted as DW1-1, DW2-1 and DW3-1 for RUN I, RUN II and RUN III respectively.

between the first crest (highest crest for RUN II) and the reattachment point. Whereas, the HSS region is located after the reattachment point. It is well known that the HSS regions are related to erosion processes whereas the LSS regions are related to depositional processes [24]. As explained previously, the distance from the crest to the reattachment point increases with the amalgamation process (from RUN I to RUN III). Therefore the area of the HSS region decreases with the amalgamation process as observed in Figure 4.10. This behavior influences the bed sediment transport rate, manifesting that along the amalgamation process, the sediment flux might be reduced. In the HSS region, the values of shear stress alternates between low and high shear stress strips. This alternation will produce “trails” on the stoss side of the bed form located downstream. The evolution of these “trails” will be modulated by the streak coherent structures (alternation of low and high velocity fluctuations regions [163]).

To get a better insight into the influence of bed shear stresses and near-bed turbulence on sediment transport processes, a visualization of the streamwise velocity fluctuation near the bed (plane parallel to the bed at $z^+ = 2$) was obtained (Figure 4.11). It is observed that a line of negative velocity fluctuations divides the zone of HSS and LSS. As pointed out by [163], in the zone of HSS there is an alternation of low and high speed streaks. The high speed streaks are less spaced at the wall than at the middle zone. For RUN I, the streaks are more defined than for RUN II and RUN III, due to a more defined THV encountered for RUN I.

To quantify the bursting events, techniques such as quadrant analysis [66, 65] and threshold crossing schemes such as U-level or modified U-level methods have been applied in previous studies [25, 88, 130, 154]. Another threshold technique is the Variable Interval Time Average or VITA method [88]. Herein the modified U-level method is used to determine the duration of the bursting events and the time between their occurrences. The results of this method are shown in Figure 4.12. The burst event is related to a strong negative streamwise fluctuation (u') [130] in a specific point of the flow domain, the location of which is detailed below. The method consists of detecting the moment at which the signal crosses a lower threshold (beginning of the event or leading edge) and a upper threshold (end of the event or trailing edge) [121]. The value of the lower threshold is typically one standard deviation

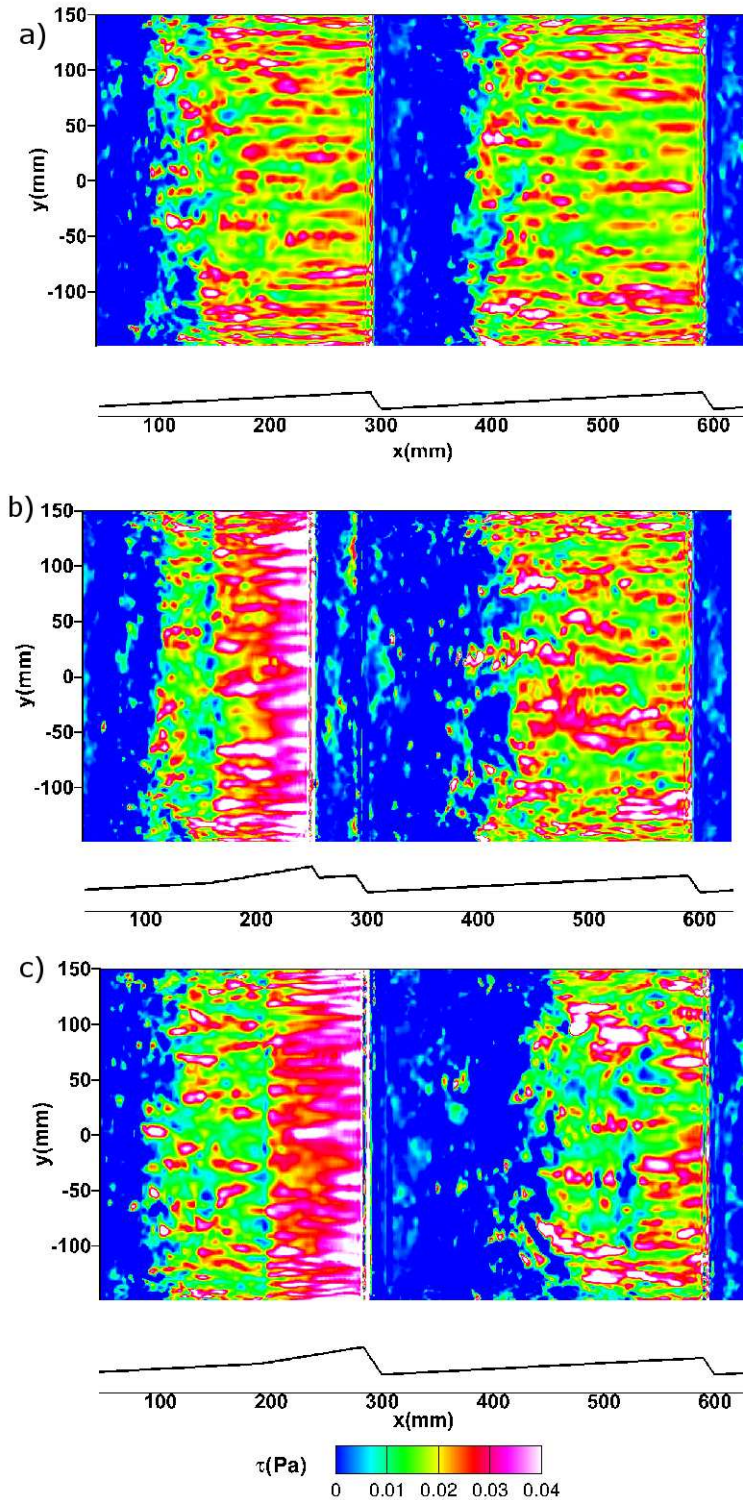


Figure 4.10: Bed shear stress contours for a) RUN I b) RUN II and c) RUN III. It is observed that the bed is divided in a high shear stress region (from 0.03 to 0.04 Pa) and a low shear stress region (from 0 to 0.01 Pa).

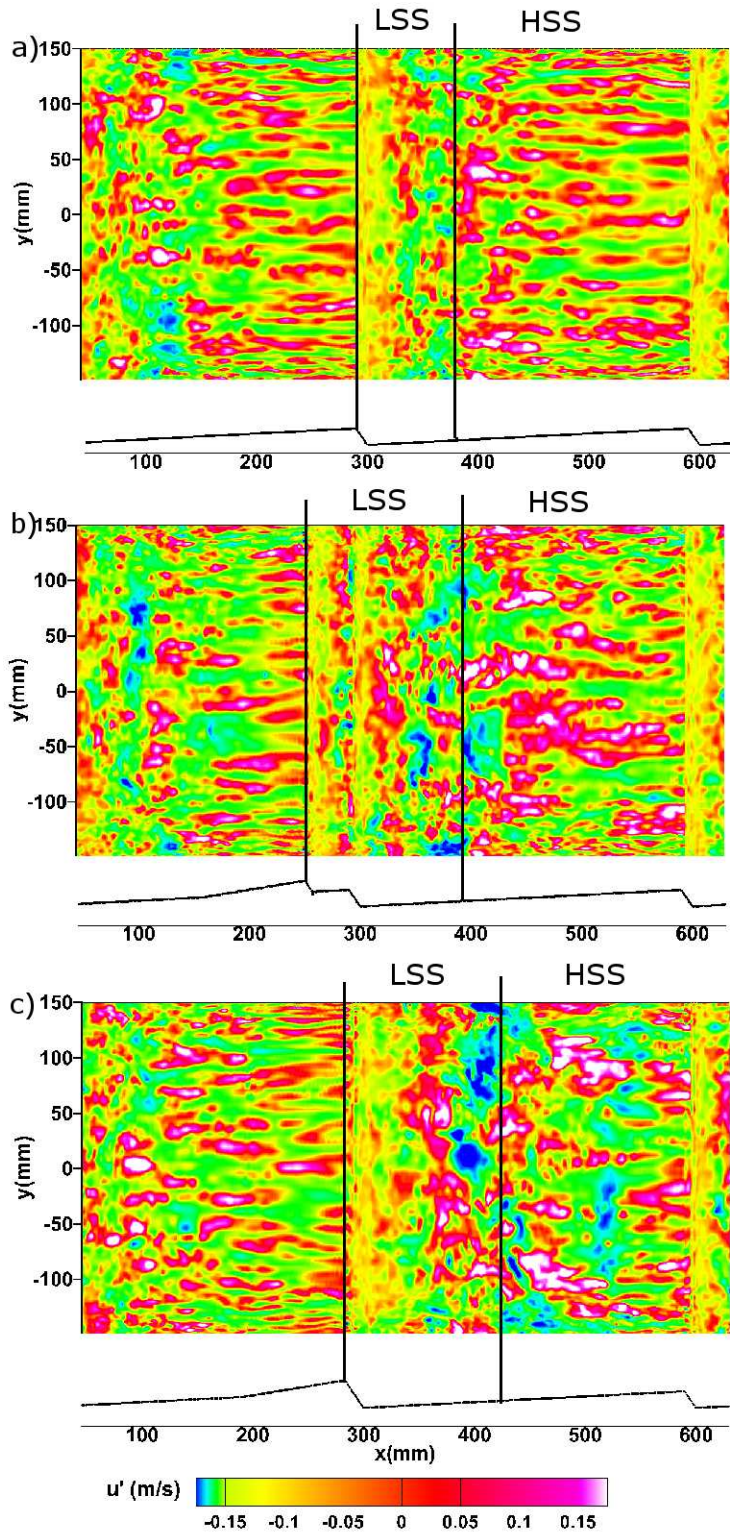


Figure 4.11: Streamwise velocity fluctuations contours (m/s) for a plane parallel to the bed at $z^+ = 2$ for a) RUN I b) RUN II and c) RUN III.

of the signal ($-\sigma_u$) and the value of the upper threshold is set to $-0.25\sigma_u$. Once the events are detected it is possible to average the duration of each event and the time between events. For all cases, a time series of 10 seconds was selected. The point was located at $x=330\text{mm}$, $y=0\text{mm}$ and $z=15\text{mm}$. The location of the point was selected in order to consider a point that falls inside the shear layer for the three cases. The average burst event duration is 0.15s, 0.33s and 0.28s for RUN I, RUN II and RUN III, respectively. On the other hand, the time between events is 0.77s, 1.28s and 1.20s for RUN I, RUN II and RUN III, respectively. These results indicate that there is a trend to decrease the rate of the bursts with the amalgamation process. However, once the bed reaches to the amalgamated state (RUN III) the bursting rate increases by 15% approximately. The time between events follow the same pattern as the duration of the even; it increases during the amalgamation process but once it is amalgamated it decreases by approximately 7%. This is related to the migration rate of the ripple formed at the stoss side of the downstream dune as previously described.

A visualization of the bursting processes for all cases is shown by Figure 4.13. The time steps selected for this visualization were taken from two time steps before the bursting event, as detected by the modified U-level algorithm. On these time steps a decomposition of the flow in two stages was observed. These stages can be summarized as 1) a flow within a structure given by the vortex (Figures 4.13 (a.1), (b.1) and (c.1)), 2) a transient evolution of the vortex skeleton from its formation to its decay (Figures 4.13 (a.2), (b.2) and (c.2)) and 3) a downstream convection of the whole structure. Once the flow reaches the last stage the instantaneous velocity vectors do not show any relevant recirculation pattern and, therefore none are shown herein. The time evolution is as follow, the vortex skeleton begins with a core of negative velocities (recirculation) and starts to travel downstream (for 4.13 (a.1), (b.1) and (c.1)) this vortex has already traveled up to a distance of $x= 350\text{mm}$), next, this vortex “explodes”, or bursts, forming a structure of positive velocity flow (between 0.1 to 0.2 m/s). The vectors showed that this structure pushes the flow upwards and thus boils appear at the water surface. The height of the vortex skeleton bursting structure is greater for RUN II than for the other two cases (approximately twice the height for RUN I and RUN III, 40mm in contrast to 20mm). It is assumed that this behavior is due to the presence of two shear layers caused by the ripple superimposed over the dune. In general, the bursting

process is associated with the time scale of the ejections and sweeps, which are independent of viscosity [84, 18]. Hence, the bursting process is associated with the sediment transport and bed morphology evolution as well as the shear stresses as explained previously by [24].

4.3 HIGH RESOLUTION MODEL OF BED FORMS AMALGAMATION PROCESS CONCLUSIONS

The flow field in a bed form amalgamation process was characterized by means of Large Eddy Simulations over fixed laboratory conditions [66, 65].

The recirculation area of the three stages (train of ripples, superimposed bed forms and amalgamated bed forms) is divided by saddles. These structures (topological signature) are located at different locations along the stoss side of the bed form for RUN I and RUN III. It was observed that the location of the saddles tends to oscillate. At the train of ripples stage there are three recirculation zones, two of them are later at the superimposed bed stage stretched downstream. At this stage four recirculation zones are defined to return to a two recirculation zones stage at the amalgamation stage. Moreover, there is an increase in the reattachment length as amalgamation process progresses, as observed by [65].

Turbulent coherent structures denoted as THV, streamwise rolls and streaks were described for the amalgamation process. Contrasting the velocity field and the elevation of the THV for the three cases, more chaotic behavior was observed once the ripple is amalgamated (RUN III). From the velocity contours (isosurface) it has been concluded that the structures starts from low speed streaks to high velocity THV that burst and form low speed streamwise rolls. Additionally, the structures tend to move toward the walls during the bursting events. This movement, indicates that these structures might influence the reshaping of alluvial banks. These turbulent coherent structures are directly related to both bedload and suspended sediment transport processes.

The inclined structures caused by plotting the spanwise velocity fluctuations and the alternation of low and high velocity streaks together with the alternation of bed shear stresses can cause complex bed morphology (e.g. trails or strips of sediments on the zone of erosion due to high shear stresses).

Using a U-level method, the bursting events were described. The bursting events and the time between them increase in frequency as the amalgamation process evolves. However, this frequency is decreased once the ripples are superimposing (RUN II). These bursting events are associated with the shear stresses, sediment transport, the deformation of the water surface and the bed morphology evolution.

The use of LES has tremendously aided to understanding of the instantaneous and mean flow structures, both temporarily and spatially, overcoming some of the limitations of experimental studies. Furthermore, with the detailed understanding of the hydrodynamics around superimposed bed forms and the amalgamation stage, more insight into sediment transport and fluvial geomorphology is obtained.

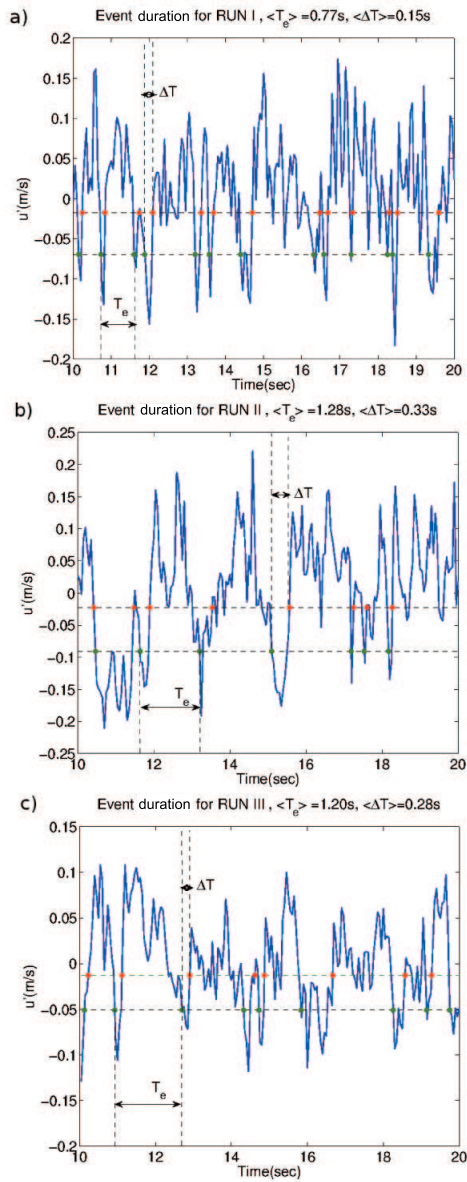


Figure 4.12: Burst frequency for a) RUN I b) RUN II and c) RUN III. Where ΔT is the duration of a single event, $\langle \Delta T \rangle$ is the average event duration for each case, T_e is the time between single events and $\langle T_e \rangle$ is the average time between events for each case.

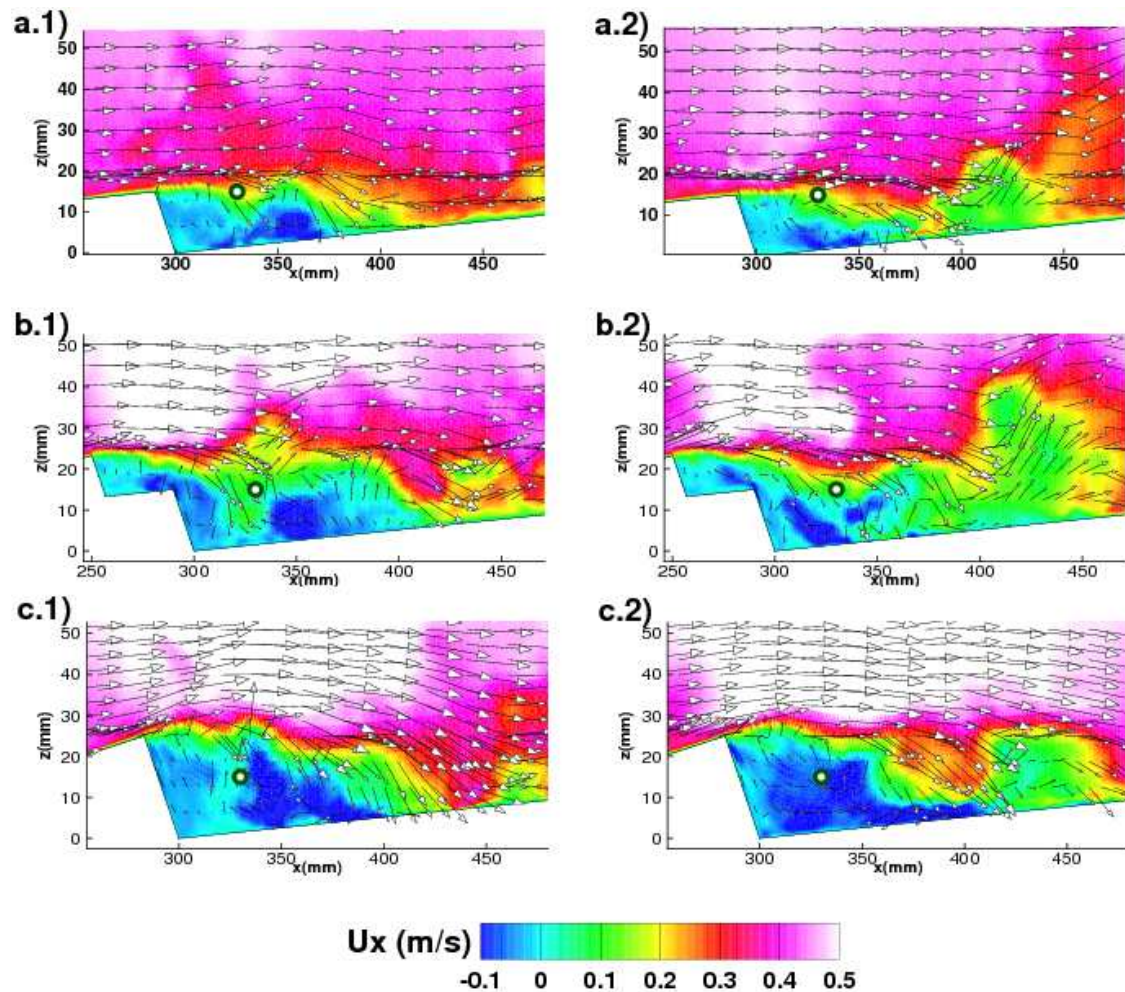


Figure 4.13: Instantaneous streamwise velocity contours and instantaneous velocity vectors for different times. The figure shows the evolution of the bursting process from one time step before the burst occurs and one time step at the onset of the burst. a.1) RUN I, Time = 10.95s, a.2) RUN I, Time = 11.3s ; b.1) RUN II, Time = 12.45s, b.2) RUN II, Time = 12.75s; c.1) RUN III, Time = 12.15s, c.2) RUN III, Time = 12.65s. The point located at $x=330$ mm, $y=0$ mm and $z=15$ mm is denoted as a white circle.

5.0 GENERAL CONCLUSIONS AND FUTURE WORK

Current models for multichannel network rivers have considered that anabranching river planforms can be obtained by reduced complexity hydrodynamics approaches, sediment routing and island residence time laws. Although they reproduce very realistic planforms, many internal physics involved in the formation of anabranching planforms are still not well understood. To summarize the findings of this thesis a list of research questions answered by it is presented below.

- **It has been observed that when the river creates an anabranching structure it splits in a main channel and some secondary channels. Is there any relationship among the width, sinuosity or migration rates between the main and the secondary channels?**

The metrics of two anabranching structures that represent three main channel sinuosity stages with time were studied using satellite imagery. It was observed that the medium sinuosity stage has a faster change in sinuosity than the low sinuosity stage. Also for all of the stages the migration is carried out by the main anabranch which is most likely triggered by extreme hydrology events (see Appendix C). On the other hand, for a low sinuosity stage the width of the secondary anabranches is inversely correlated to the main anabranch width and sinuosity. Finally a threshold of 200m of channel width at all sinuosity stages was found. After this threshold is reached the anabranch may disappear in following years. However, is important to note that all these observations are for anabranching structures in which bifurcation and confluence locations do not change with time. An example of a structure with non-fixed bifurcations and confluences can be found in Appendix C.

- **Do the anabranching rivers behave similarly to any other multichannel network systems such as a braided river or anastomosing river? If so, what are the characteristic processes observed in the planform development of these rivers?**

[100, 16] considered that for braided rivers the channels behave as meandering channels with erosion at the outer bank and deposition at the inner bank. The bathymetry and simulated flow field for two anabranching structures sites proved that the secondary channels do behave as meandering channels, similar to the channels found in braided systems, but they are not fully developed. This is because the secondary channels end abruptly at a confluence with another secondary channel or the main channel. The anabranching structures selected represented different main channel sinuosity stages. Also, [100, 16] considered that for braided rivers the main processes are channel width adjustment and mid-channel bar formation, channel migration and branch abandonment. From multi-temporal satellite imagery analysis of the selected anabranching structures all of these processes were observed, but with some differences. For example, instead of a mid-channel bar formation, a bare-soil island formation was identified in which the islands are flooded every maximum hydrology event until vegetation is consolidated on them and thus they become permanent. The latter is considered also in [139]'s model however a vegetation residence time is still needed to compute and, considering the amount years of satellite imagery available, it would be still too early to make any conclusion.

- **Recently it has been proposed that in a meandering river the presence of bed forms modulates the bank shear stress and therefore the migration rates. The largest rivers in the world are anabranching. Is this happening at a large anabranching river scale? If so, how do the bed forms modulates the bank shear stress?**

Since the channels in the anabranching structures were found to be behaving as a meandering channel, a similar size meandering channel was selected to develop the methodology to study the influence of bed forms in bank shear stress. The site studied was a bend located in the Wabash River. It was found that indeed the presence of bed forms increases the bank shear stress by more than 150%. Also, high shear stresses at the

middle height and toe of the bank were observed. The latter implies that the cantilever and planar failures will be enhanced. In particular, as reported by [37] and observed from field visits, the bank erosion occurs when the soil located at the top of the bank fails by gravity. This is probably because when the water was higher the fluvial erosion took most of the fine sediment from below the top of the bank. On the other hand, the bank shear stress is correlated with the size of the bed forms. The bigger the bed form is, the larger the shear stress is that is exerted on the bank as shown from a comparison between a bed with bed forms and a bed without bed forms.

- **In previous research it was observed that the amalgamation process from a train of ripples to a dune size bed form represent a stage of high Reynolds stresses which implies a very important feature in sediment transport. On the other hand, previous studies have explained the important role of turbulent coherent structures in sediment transport. However, up to date there is no assessment on what type of turbulent coherent structures are present during the amalgamation processes. If it is found that bed forms modulates the bank shear stress on large anabranching rivers, what is the effect of bed form amalgamation on the turbulent coherent structures?**

A Large Eddy Simulation to study the turbulent coherent structures due to bed form amalgamation along with other parameters was carried out. From it, observations such as that the recirculation area of the three stages is divided by saddles and that when the ripples are amalgamated a more chaotic turbulent horseshoe vortices were observed. Also it was noticed that the bursting events and the time between them increase in frequency as the amalgamation process evolves. Although this process has been studied for a two dimensional experimental flume it was possible to study the phenomenon in three dimensions. It is expected that future LES models on an anabranching flume with three dimensional bed forms will give a better insight of the amalgamation process for the bed forms found in anabranching structures.

To the best of my knowledge, this is the first time the dynamics of a large anabranching river have been scaled up from turbulent coherent structures to anabranching structures at the field scale and analyzed. Physics related to the sinuosity stages of the main channel and

typical morphodynamics processes involved in the development of anabranching patterns have been studied. Also the role of bed forms in the hydrodynamics and bank processes were assessed. However, there are several questions still to be addressed in future research. Differences and similarities have been pointed out between the migration and multi-temporal geometry of the main channel and the secondary channels . Also it was concluded that the bed forms modify the bank shear stress. The question is then, is there any difference between the bed forms found in the main channel and the secondary channels? To answer this question it is proposed to study the bed morphology of an anabranching structure flume. This flume is under construction and details of its progress can be found in Appendix B. On this flume, mobile bed experiments will be carried out for different cases as explained in Appendix B. Additionally, by doing a Large Eddy Simulation of the results obtained from this flume it would be possible to study the interaction of the bed forms and the flow field at a high resolution scale.

On the other hand, secondary flow has proved to be driven more by inertia than by the presence of bed forms for a field scale. However the differences between the main channel and secondary channels secondary flow in anabranching structures have not been studied yet. In this regard, a study of the Madeira River has started. In Appendix A a progress report of the field data collection campaign carried out on 2012 and 2013 at this river is given. With the bathymetry and velocities measured on those campaigns a three dimensional model will be built to characterize the secondary flow on the main and secondary anabranches of two sites. As a complimentary work it is proposed to analyze the downstream effect of a dam constructed using a two dimensional model and explain if the deep cross sections at the bends have any relationship with the construction of the dam.

Finally, the location of the bifurcation and confluences of the anabranching structures studied herein were fixed with time. This is not always the case in the anabranching structures observed in the Upper Amazon River Basin. For example at Iquitos (the largest city in the Peruvian Amazon rainforest) the anabranching structure presents bifurcation and confluence points that are changing with time. This particular structure has been studied by the EPEF (Earth Processes and Environmental Flows) group of the University of Pittsburgh. The results have been submitted to the Journal of Geomorphology and can be found

in Appendix C. Some important conclusions are the fact that there is a high correlation of migration with rapid increase of water levels and that wider channels will have a higher capacity of erosion of near bank areas during conditions of high water levels on the river. Since water level represents such an important parameter for the dynamics of anabranching structures with temporal variability of bifurcations and confluences, a methodology to measure water stages at various points should be designed. Herein a GPS surveying to calculate the water slope for a main channel high sinuosity stage was used. However this is useful only when an average of a single day of measurements is needed. For a continuous set of data it is suggested to implement gaging stations at the beginning, middle and end of each channel. The best way to implement this is by defining a datum in one of the inner banks and place a pressure sensor to measure the water depth. A setup like that will be also useful for navigability purposes.

APPENDIX A

MADEIRA RIVER FIELD THREE DIMENSIONAL MODEL. FIELD CAMPAIGN REPORT.

A.1 OBJECTIVE

Collect field data to be used for modeling of three sites at the Madeira River, Porto Velho, Brazil. The models will be used for 1) explain why there are unusual deeper cross sections and high transversal slopes along the bends of the Madeira River 2) study the secondary flow on main and secondary channels of anabranching structures and 3) assess the effect of a dam building in progress on the bed morphology of the river.

A.2 INTRODUCTION

The Madeira River is a tributary of the Amazon River. It has an annual discharge of 32,000 m^3/s , a drainage area of 1.36 million km^2 and an average annual sediment yield of 330 $tons/km^2$ per year [118]. Two dams are planned to be built in the Madeira River, the San Antonio Dam and the Jirau Dam. Both dams are run-of-the-river projects and therefore there is no a large reservoir impoundment planned for them. Because of this, there has not been a strong opposition in their construction. However, the implications that these structures will have in the Madeira River sediment transport and therefore planform and bed morphology change is still unanswered. The Madeira River planform show anabranching patterns which

is typical in large rivers such as the Amazon River, Orinoco River or the Brahmaputra River. Previous work to explain the morphodynamics on these types of rivers has been carried out by [72] and [124]. On these studies two dimensional numerical models and satellite imagery were used.

On the 2012 and 2013 field campaigns at the Madeira River it was observed from the bathymetry survey that the water depth was too high at the outer bank of main channel bends. It is believed that this fact is due to the recent construction of the San Antonio Dam located 6Km southwest of Porto Velho in the state of Rondonia, Brazil. To gain a better insight of this phenomenon additional field data such as velocity transects and sediment samples were collected to be used in numerical modeling of three locations downstream of the San Antonio Dam.

A.3 FIELD CAMPAIGN

On December of 2012 a field campaign to collect bathymetry, velocity transects and sediment samples were carried out. The bathymetry was surveyed using a DGPS Furuno echosounder (see A1). and the velocity transects were measured with a Teledyne aDcp (acoustic Doppler current profiler) (see A2). Three sites named FS, SS and TS were selected as shown in A3. At FS and SS are located in anabranching structures of the Madeira River whereas TS is located at a straight portion of the Madeira River and is the closest to the San Antonio dam

From A4, A5 and A6 it is observed that as farther downstream the site is located the water depths are lower. A possible cause of this phenomenon is the decrease in sediment transport due to the dam immediately downstream of it by December of 2012. Thus, the effect of the dam on the sediment transport decreases further downstream of it and therefore water depths in FS is almost 50% of TS. This hypothesis must be corroborated by numerical modeling of the bed morphology for different scenarios. On the other hand, aDcp data was surveyed for the three sites. An example of velocity transects for sites FS and SS are shown in A7 and A8 respectively. Almost all the cross sections were surveyed 4 times to ensure secondary flow is captured correctly. This information will be used to validate the numerical



Figure A1: Furuno Echosounder.



Figure A2: Teledyne Workhorse Monitor aDcp.



Figure A3: Madeira River Study Site Map.

models. However, not all the aDcp as georeferenced and therefore additional process is still to be addressed to locate all the velocity points surveyed. Also bed sediment samples and samples at the water surface were collected. The procedure used to collect bed sediment samples was an in-house metal apparatus that was tossed in the water and pulled by the boat until enough amount of sediment was collected (see A9). Finally, the water surface slope was obtained by measuring the water elevation at two points showed in A10. The average precision on the vertical was 4cm which gave a water slope of 0.0072%. This water surface slope will be used to calculate the bed elevation of the three sites by subtraction. The procedure to be used will be the same as [72].

On 2013 another campaign was held in the Madeira River. The data collected was the same as the one collected for 2012. However, since it was collected for the wet season a deepest water depth was registered as shown in A11. On this Figure it can be seen that the water depth is surprisingly high and with maximum values of about 82m. Although the field campaign season was different the increase in 4 times the maximum water depth found for the second campaign let us hypothesized that the effect of the dam is propagating and now in site SS the bed has been increasingly eroded in less than a year. Implications of

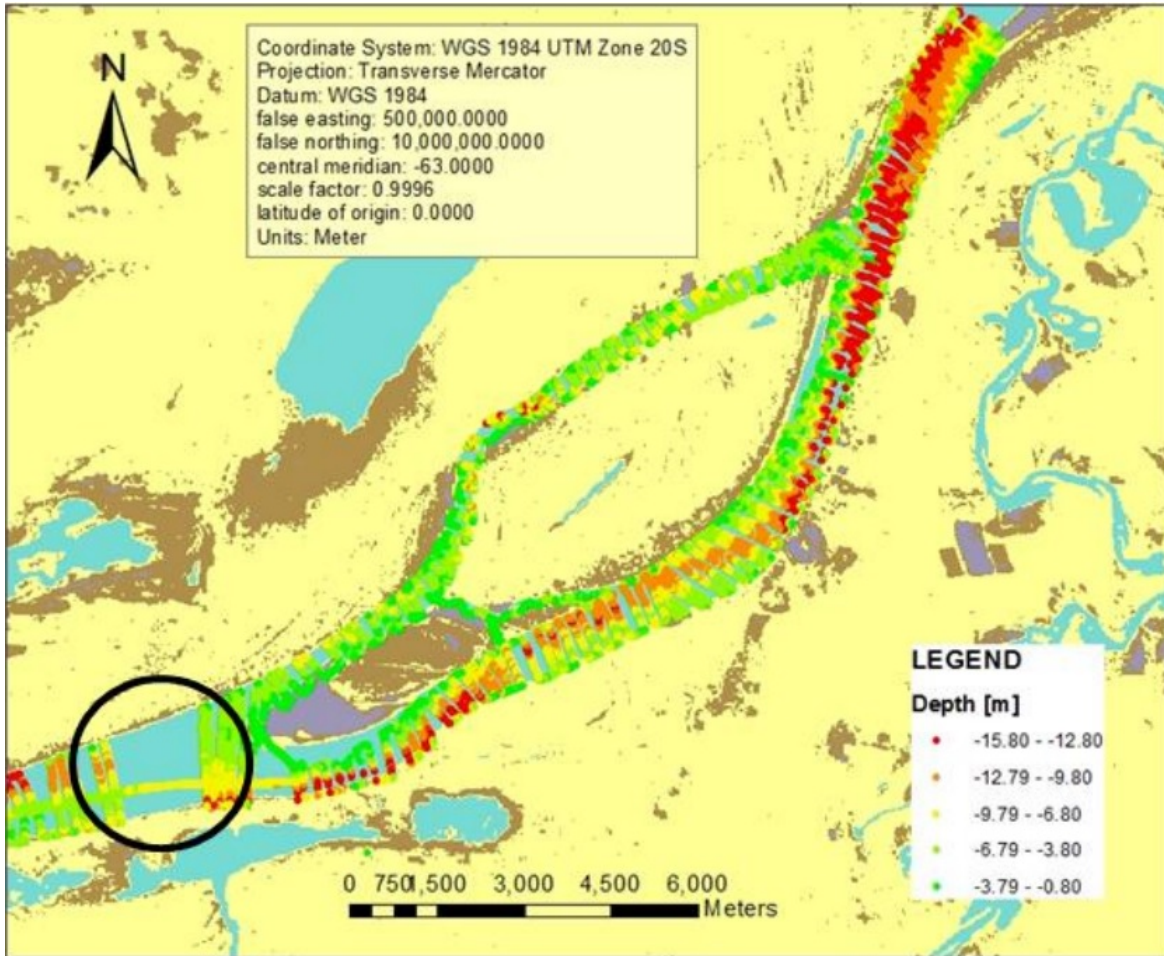


Figure A4: FS 2012 Bathymetry. There is a data gap in the area inside the circle. Cross sections are spaced at least every 200m.



Figure A5: SS Site 2012 Bathymetry. There is a data gap in the area inside the circle. Cross sections are spaced at most every 300m on the secondary anabranches and 500m on the main anabranch.

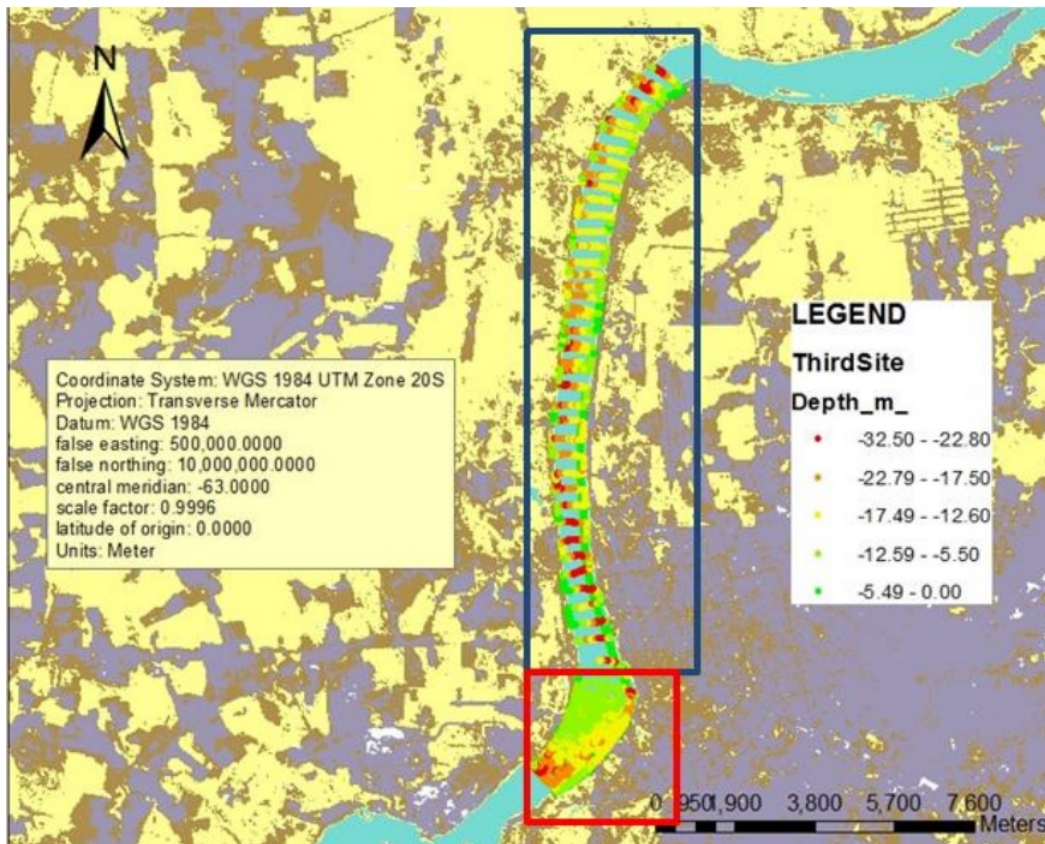


Figure A6: TS Site 2012 Bathymetry. Cross sections are about 400m at the coarse resolution region (blue rectangle) and about 150m at the fine resolution region (red rectangle).

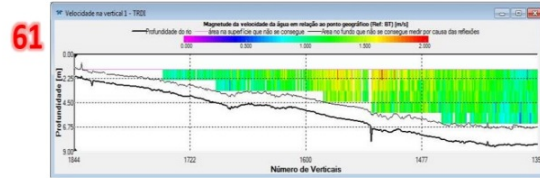
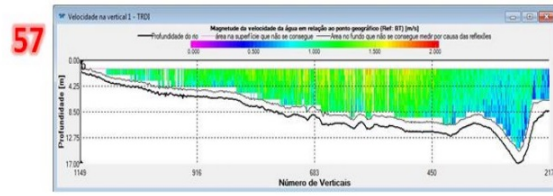
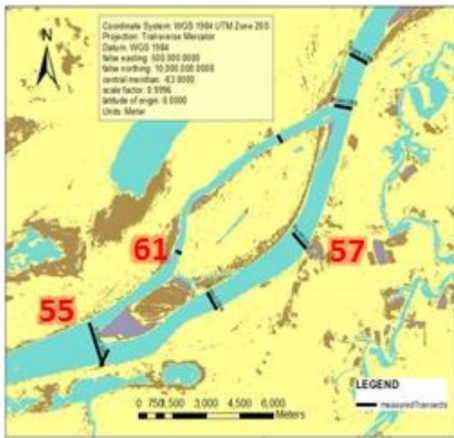


Figure A7: FS Site aDcp transects. GPS was not available at most of the transects surveyed on this site.

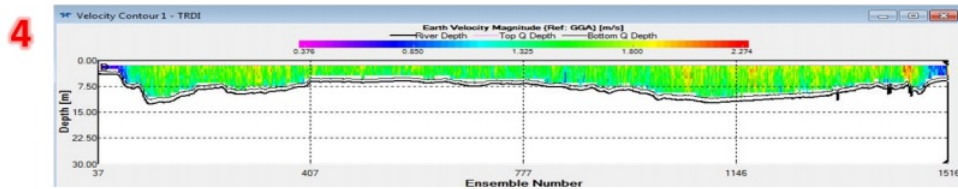
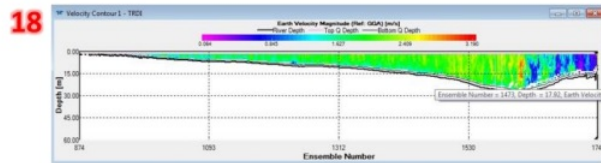
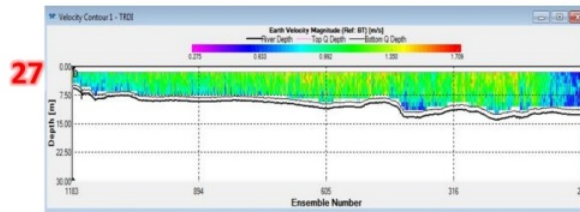
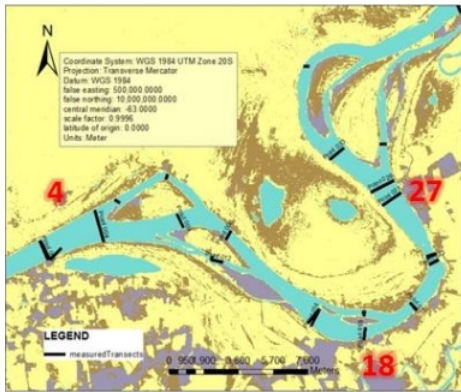


Figure A8: SS Site aDcp transects. GPS was available at most of the transects surveyed on this site.

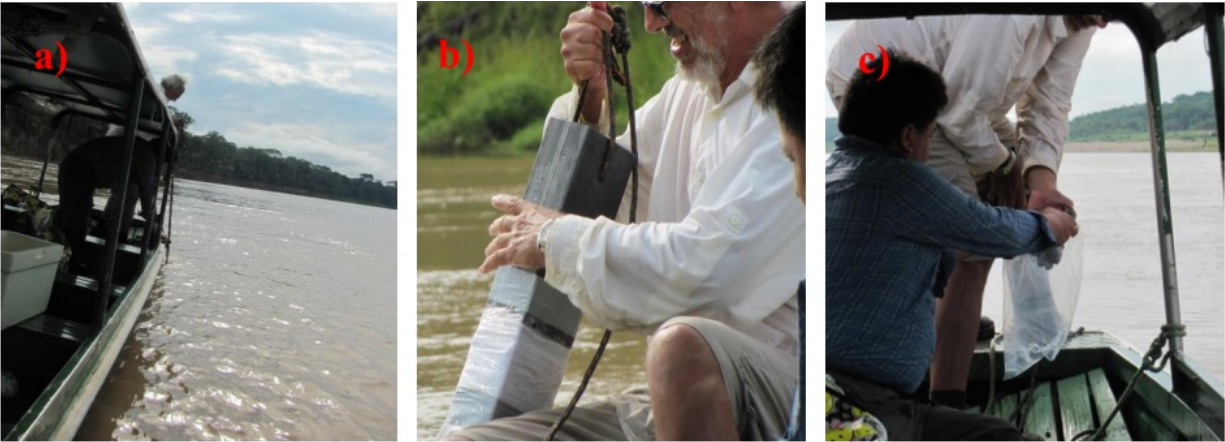


Figure A9: Bed sediment sampling. (a) The sampler is tossed in the water and the boat drag it until enough sediment is collected. (b) The sampler is pulled back in the boat. (c) The collected sediment is saved in plastic bags.



Figure A10: GPS points used to compute the water surface slope. The distance between them is approximately 12.3km and the difference in elevation between them is 1m.

this phenomenon are the change in sediment nutrients downstream of the dam and also the perturbation in the river planform stability. The latter is reflected in higher bend average migration and mid-channel bar creation as well as channel widening as observed by [72]. However, this hypothesis needs to be corroborated with a quantitative comparison between 2012 and 2013 morphology as well as with three numerical simulations of sites FS and SS. On the other hand, the water slope used points located along the three sites in contrast to the only two points used for the 2012 campaign.

A.4 CONCLUSIONS AND FUTURE WORK

From the field data collected in campaigns 2012 and 2013 it has been observed that the dam is affecting the morphodynamics of the Madeira River downstream of it. However it was expected that since this is a run-of-the-river structure the impact of it should be minimal. With the data collected on both campaigns is possible to carry out two dimensional and three dimensional numerical models. However, there is still needed to prepare the data for mesh construction and validation. Based on previous work in numerical modeling of large rivers [71]. it is proposed the use of OpenFOAM for the three dimensional model. With this numerical model it will be possible to characterize the secondary flow on sites FS and SS. The numerical model will extend the scope of the velocity measurements by visualizing velocity patterns in several locations. Moreover, to study the downstream effect of the dam it is proposed to carry out a numerical model for selected mobile bed scenarios. The model to be used for this purpose will be TELEMAC 2D coupled with SYSIPHE. By using these two models it will be possible to simulate the hydrodynamics and bed deformation of the straight channel at site TS. The following tasks are needed to convey for the goals specified above:

- Obtain bed elevation surface and build numerical meshes for OpenFOAM and TELEMAC 2D using the procedure explained in [71] (other data needed to do this will be water surface and digitalized banks from satellite imagery).

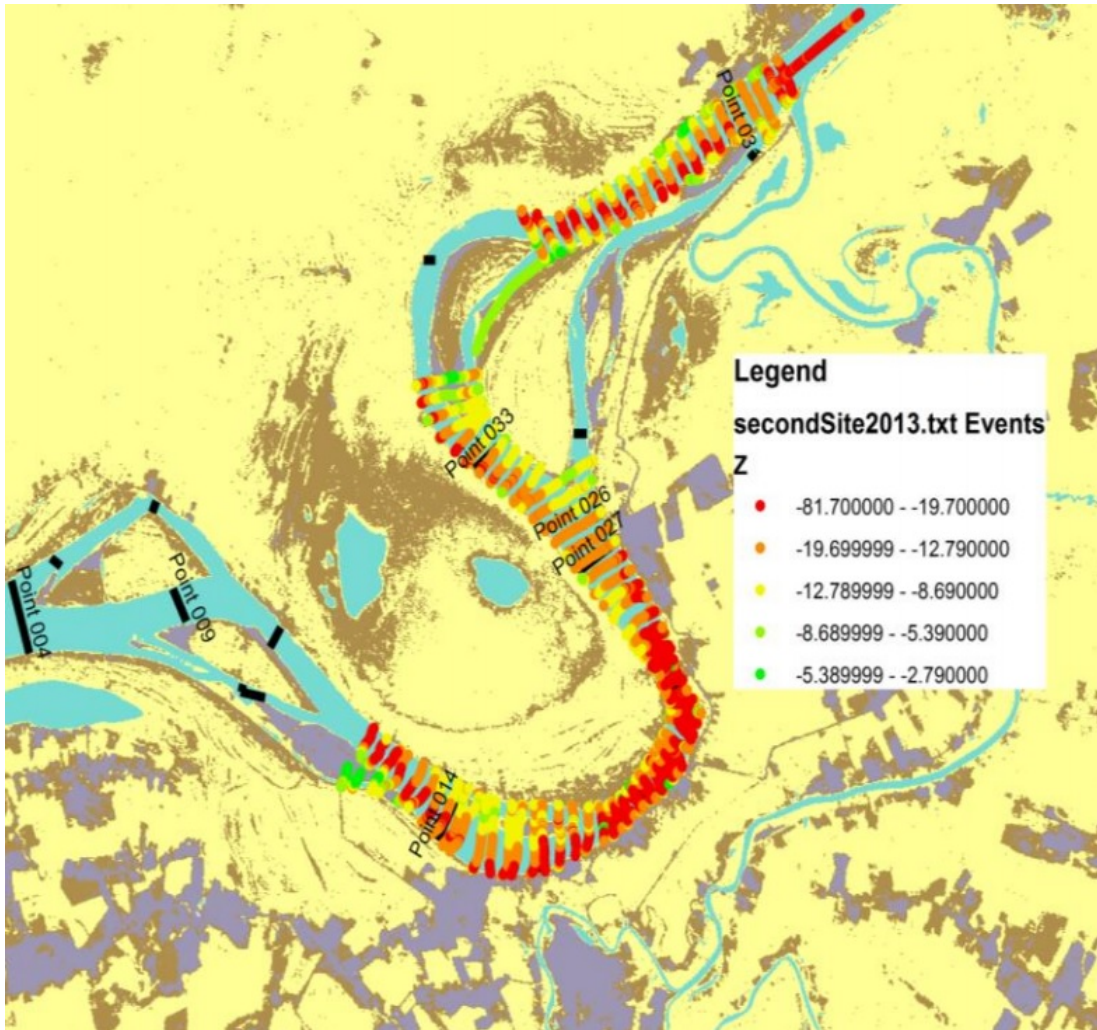


Figure A11: SS Site 2013 Bathymetry.

- Elaborate code and/or programs to automate the process of georeferencing the aDcp cross sections with missing GPS information.
- Validate the numerical models by comparing the measured velocity data and the modeled velocity at selected cross sections. Also the water surface elevations will be used to validate the two dimensional models.
- Determine the sediment rates to be used in the different scenarios of the numerical simulations for site TS. Since no validation data is available for the sediment transport an statistical method could be performed to assess the veracity of the results. Perhaps Montecarlo method could be used in this regard.

APPENDIX B

ANABRANCHING FLUME. CONSTRUCTION PROGRESS REPORT

B.1 OBJECTIVE

Build a flume that resembles an anabranching river planform to study the interaction between the main and secondary channels bed morphology. The flume is to be placed in the University of Pittsburgh EPEF (Earth Processes & Environmental Flows) lab. The entire design and construction of the flume will be carried out by the EPEF group.

B.2 INTRODUCTION

Up to date multichannel river networks have been studied with experimental flumes that resemble braided channels [16] and flumes that study meandering chute cutoffs [174]. A very special type of multichannel river network is the so called anabranching planform. This type of river planform has captured the attention of the fluvial geomorphology research community since is characteristic of the largest rivers in the world [118]. Recent studies have shown the importance of the planform migration interaction between main and secondary channels in a anabranching structure [72, 124]. Although, these studies helped to understand the dynamics in multichannel rivers, very little has been done to characterize the relationship between main and secondary channels bed morphology. To do the latter on a field scale it would be needed to have high resolution bathymetry data such as the one obtained by using multibeam

echosounders. However, due to logistic and budgets constraints this methodology is expensive and will represent a great endeavor to survey large rivers such as the ones where anabranching structures are present. Likewise, the fact that the bed morphology migrates and interacts dynamically in these channels adds another complication in studying bed morphology by using field data.

Herein a flume that resembles an anabranching structure found in the Upper Amazon River Basin is proposed to study the relationship between the main and secondary channel bed morphology. The anabranching structure selected is located upstream of Iquitos, the largest city in the jungle of Peru as shown in [B1](#). This anabranching structure has a high sinuosity main channel as shown by [\[72\]](#) and three secondary channels by 2012. The current report details the design of the planform and construction of this flume.

B.3 HEAD AND TAIL TANK CONSTRUCTION

The tanks were built with plastic sheets and placed as shown in [B2\(a\)](#). The tail tank was reinforced with wood beams surrounding the tanks (see [B2\(b\)](#)). Whereas, the head tanks were reinforced with plastic sheets on the top in such a way that the flexural strength at the tank walls were sufficient to balance the force exerted by the hydrostatic pressure. The dimensions of the head tank are 0.5m x 2.4m x 0.6m while the dimensions of the tail tank are 0.9m x 0.6m x 2.3m. Both tanks were filled up with water to detect any leak. The head tank did not show up any leak whereas the tail tank leaked on the area around the inlet pipes for water and sediment. The leaks were fixed with silicone RTV successfully.

B.4 PIPING SYSTEM

The piping system consisted of two separate pipelines for sediment and water. The water pipeline recirculated the water with a 5.5KW pump. Thus, the water was diverted from the tail tank to the head tank continuously and keeping a constant flow rate in the system. On



Figure B1: Anabranching structure selected for the experimental flume planform.

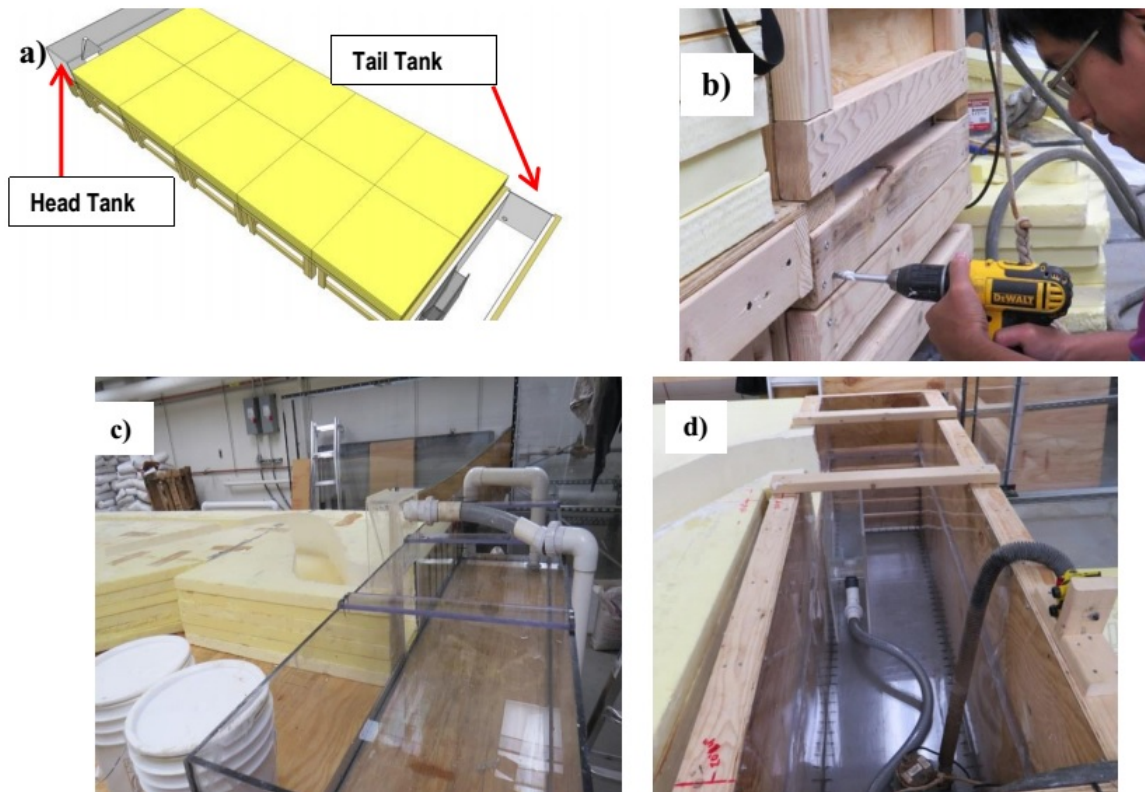


Figure B2: Head and Tail tanks. (a) Location of the tanks. (b) Construction of the tail tank wood frame. (c) Head Tank and sediment entrance. (d) Tail tank with sediment trap inside and laser level on top.

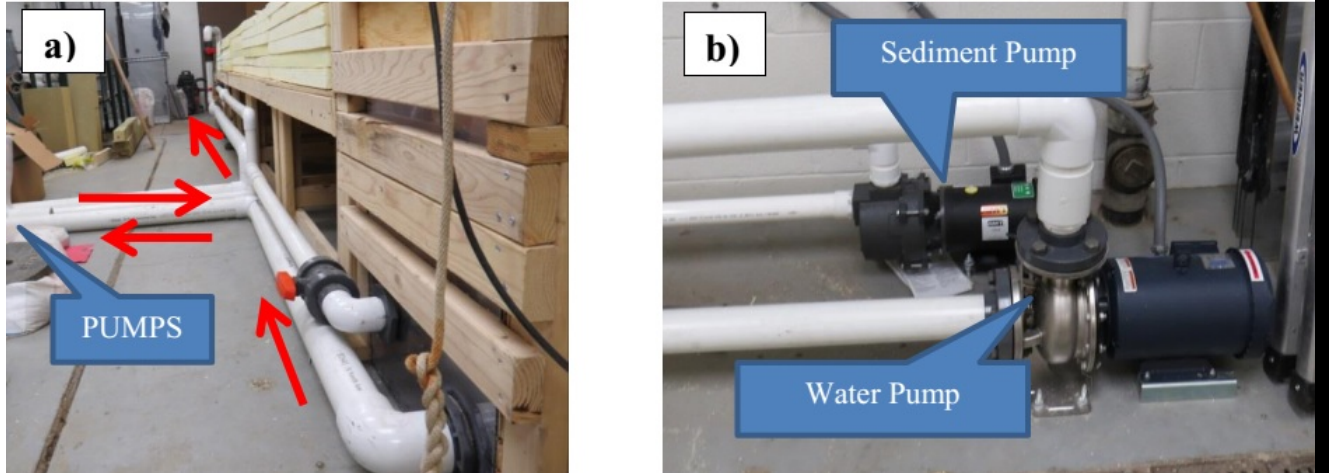


Figure B3: Piping System. (a) Pipeline connecting the tail tank with the head tank. (b) Detail of the pumps for water and sediment.

the other hand, the sediment was pumped using a 2.2KW pump. To collect the sediment outflowing from the flume a sediment trap (see B7(c) and B7(e)) was constructed and placed inside the tail tank. At the head tank a sediment distribution structure (see B7(a) and B7(b)) was also placed in as shown in B7(d). The final piping layout is shown in Figure 3. The sediment will be recirculated using this piping system until the sediment rate will be constant. The sediment rate will be measured by collecting and weighing the sediment in the sediment trap. At this point the bed morphology will be considered in equilibrium.

B.5 FLUME BODY CONSTRUCTION AND PLANFORM DESIGN

The body of the flume was made out of insulation foam panels. Six layers of insulation foam panels of 48in by 48in were used for the body of the flume. The foam panels were arranged according to the layout shown in B5. These were shaped accordingly to resemble an anabranching river planform with one main channel and two secondary channels as shown in B5. The main anabranch planform was obtained by fitting a sinusoidal function for a

particular anabranching structure located in the Upper Amazon River Basin (see B6). The width of the main channel is about 0.3m and the height is 0.2m. On the other hand the secondary channels of the flume are straight contrary to the secondary channels found in the anabranching structure used for the main channel. The width of these channels is 0.1m. The planform was drawn on the foam top layer using coordinates obtained from a CAD drawing (see B6). Since the panels can be easily removed and replaced it is possible to change the straight secondary channels with meandering ones and in such a way study the effect of the sinuosity of the secondary anabranches in the bed morphology.

Then, the panels of the top layer were cut with a jigsaw separately following the drawn lines on them. After all the panels were cut five more layers were cut using the already cut panels as a template (see B4(a) to B7(c)). Finally the panels were glued vertically and horizontally using 3M Scotch Weld High Performance Plastic Adhesive 1099. However, it was noticed that this adhesive was burning out the foam and therefore RTV silicone sealant was used instead. It is suggested that for future foam flumes they should be glued only with RTV silicon sealant.

To impermeabilize the walls and bed of the flume two layers of Warren Environmental Inc M301-18 epoxy resin was used. Due to the thickness of the epoxy resin it was applied by hand and then leveled using a common finishing metal trowel (see B4 (d)). However, this methodology left at the wall surface some peaks of epoxy which increases the wall roughness. Because of that the walls were smoothed out by filing. For the bed one layer of System Three General Purpose Epoxy resin was used. This epoxy resin was less thick than the one use on the walls and thus it could be poured on the bed until it settled down by gravity forming a perfect leveled and smooth surface (see B7(e)). Finally, some small gaps and imperfections were fixed with RTV (see B7(f)). The estimated time of drying of M301-18 epoxy resin depended on the amount of hardening used in the mix. If too much hardening was used then the drying time could last from a few days up to two weeks. However, most of the times the drying times were up to 3 days when building the body of the flume. On the other hand, the drying time for the General Purpose Epoxy resin was at most 24 hours.



Figure B4: Flume body construction procedure. (a) The main channel shape is drawn on the top layer foam. (b) the foam panels are cut following the lines drawn. (c) The foam panels are piled in six layers. (d) Application of Epoxic M301-18 for the channel walls. (e) Application of General Purpose Resin for the channel bed. (f) Sealing of bed and walls joints with RTV silicone.

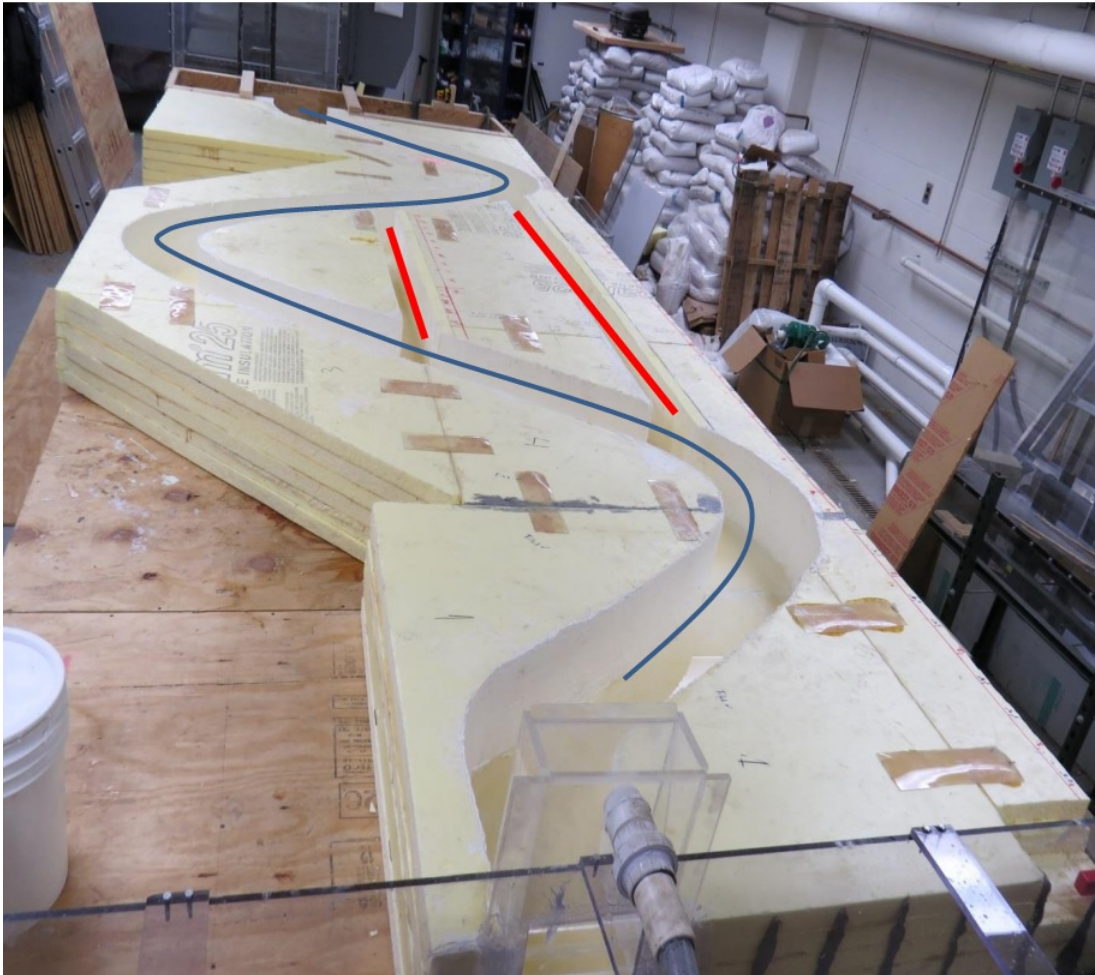


Figure B5: Actual layout of the Anabranching Flume. The blue line is the centerline of the main channel. The red lines are the centerlines for the secondary channels. The flow goes from the bottom to the top of the picture.

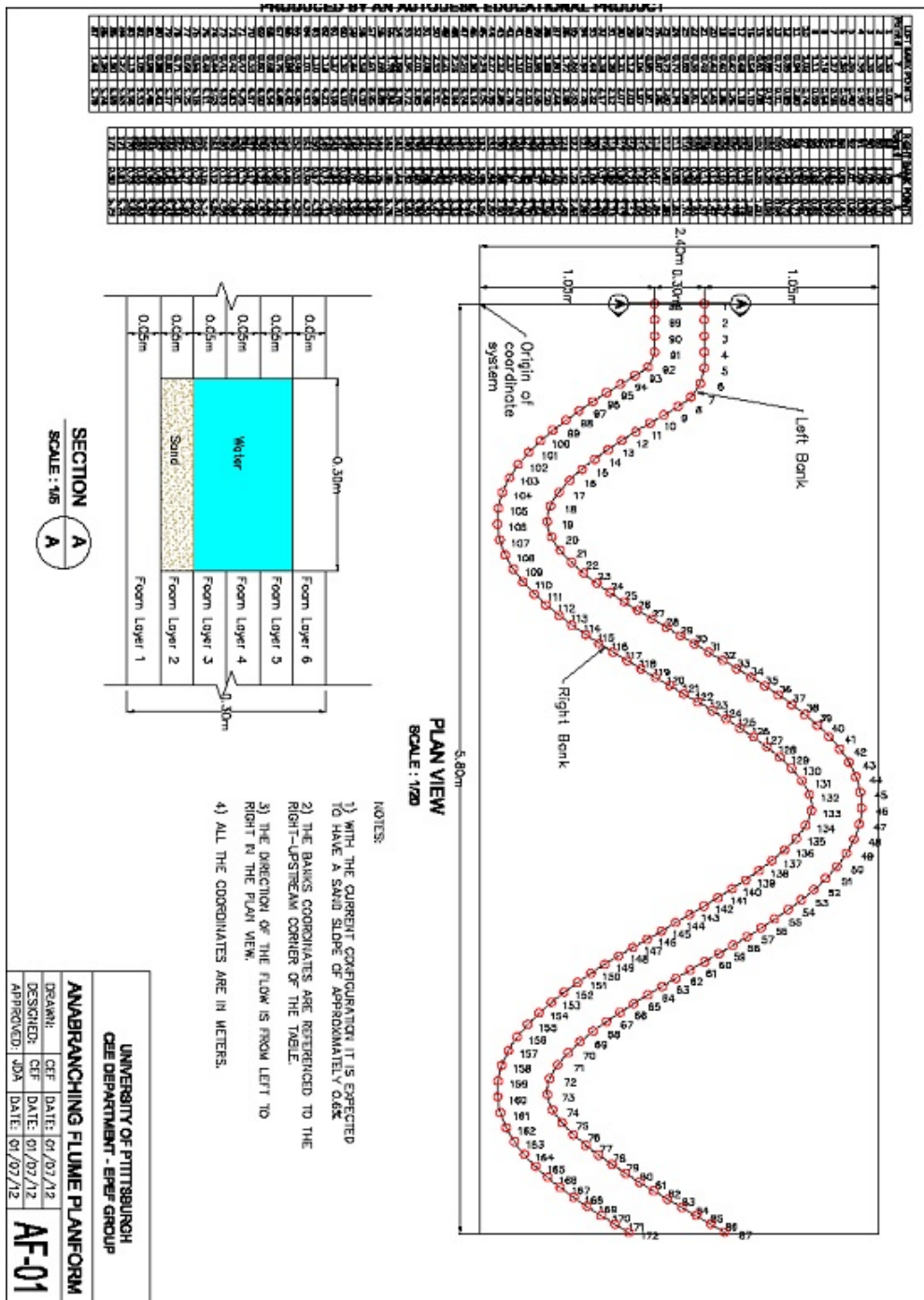


Figure B6: CAD drawing with the coordinates of the main channel.

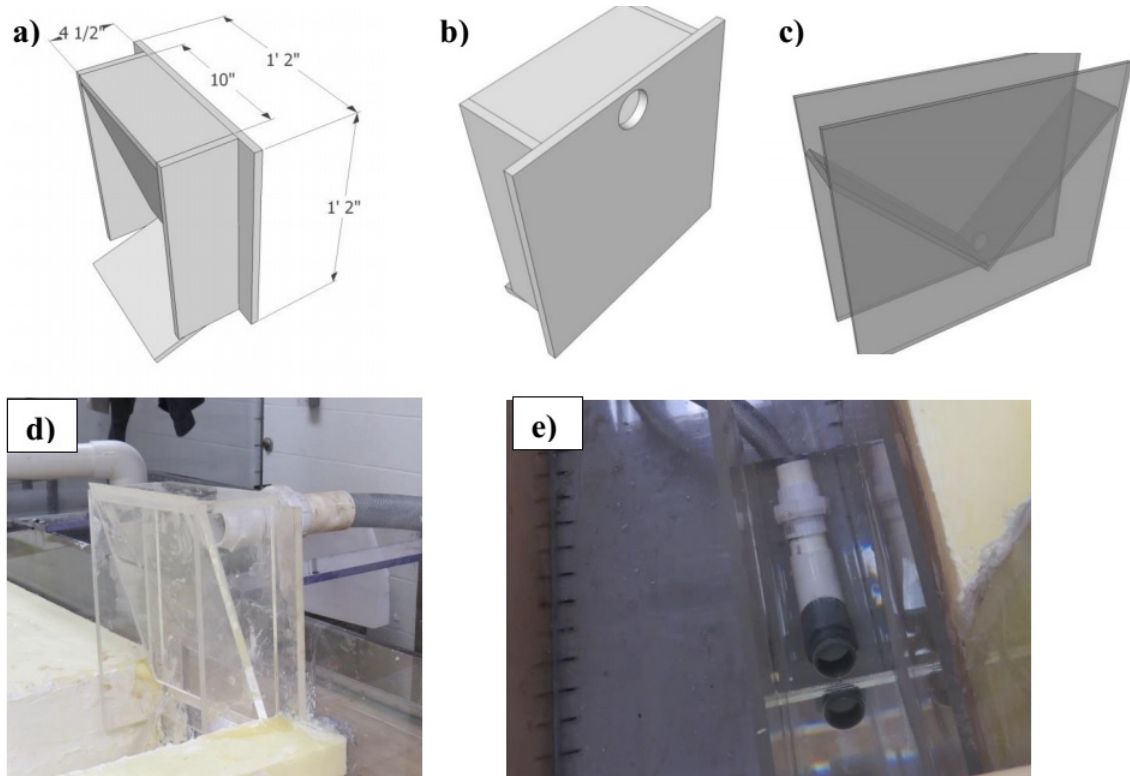


Figure B7: Sediment control structures. (a) Dimensions of the inlet sediment entrance structure. (b) Perspective view of the inlet sediment control structure. (c) Perspective view of the outlet sediment structure. (d) Actual view of the sediment entrance structure attached to the piping system. (e) Actual view of the sediment trap in the tail tank.

B.6 BED MORPHOLOGY MEASUREMENT

The bed morphology will be measured with a LJ-G200 Keyence Laser Profiler. For this purpose cross sections spaced every 5cm were located on the top of the channel. Also a mounting frame was built to fix the horizontal position of the laser profiler as shown in B8(a). The vertical position of the laser profiler was referenced to a datum located on the tail tank. A Bullseye Auto-Leveling Laser with AnglePro was located on top of the tail tank to define a horizontal plane at the datum elevation as shown in B8(b), B8(c) and B8(d). Also on top of the laser profiler mounting frame a bubble level was placed (see B8(a)). In such a way the vertical level will be maintained along the channel every time the mounting frame is moved horizontally from cross section to cross section.

B.7 CONCLUSIONS AND FUTURE WORK

A flume has been built and is ready for a leak detection test on the main body. After the leak detection test passes, sediment will be added and the base cases can start. The base cases to be run in the flume are:

- MoS1cS2c: only the main channel will be opened for water and sediment flow.
- MoS1oS2c: the main channel and one secondary channel will be opened for water and sediment flow.
- MoS1oS2o: all the channels will be opened.

All the cases will be run for a shallow water depth of 5cm (H5cm) and a high full channel water depth of 20cm (H20cm). Therefore six final cases will be used MoS1cS2c-H5cm, MoS1cS2c-H20cm, MoS1oS2c-H5cm, MoS1oS2c-H20cm, MoS1oS2o-H5cm and MoS1oS2o-H20cm. It is expected that the bed morphology obtained on this flume will answer the following questions:

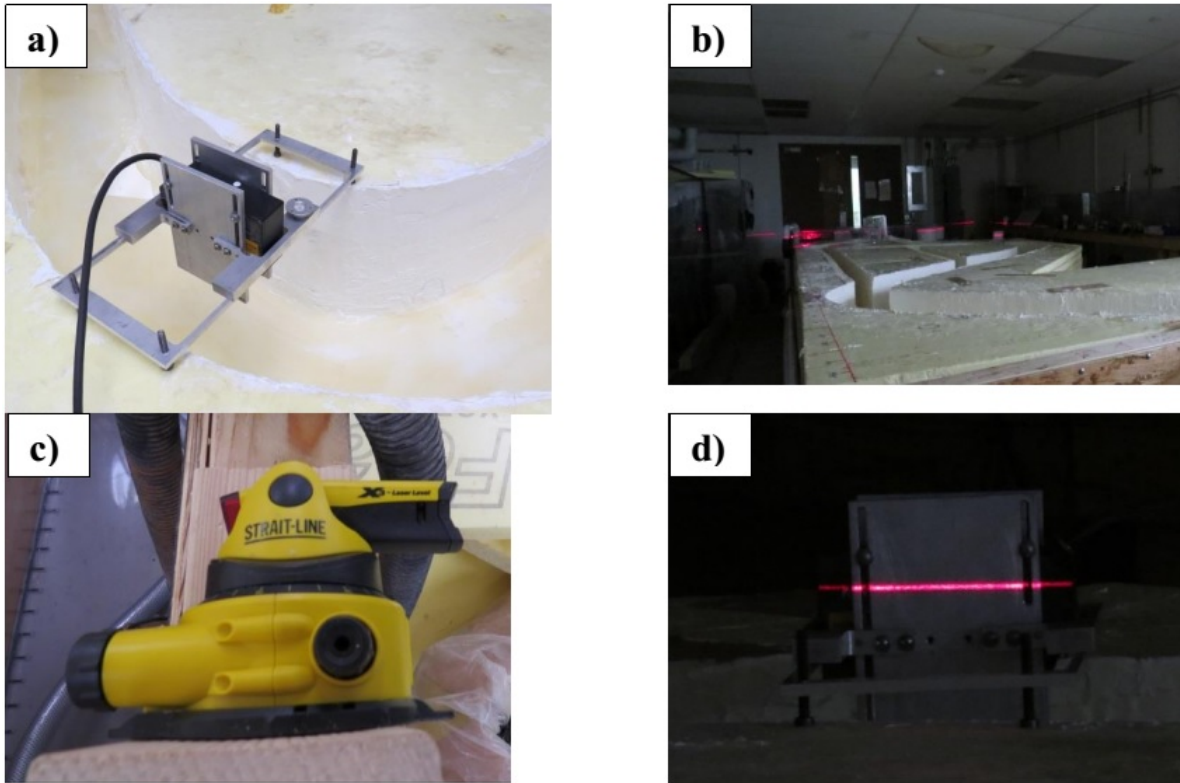


Figure B8: Methodology used to measure the bed morphology. (a) A Keyence Laser Profiler is mounted on an aluminum frame every 5cm along the channels. (b) An horizontal plane to control the vertical position of the laser profiler is obtained with a laser level. (d) Detail of the laser level located on top of the tail tank. (e) Line drawn by the laser level on one of the sides of the laser profiler aluminum frame.

- What is the bed forms scale on the main channel respect to the secondary channels?
- Is the bed forms migration rate in the main channel the same when secondary channels are active?
- How are the bed forms average amplitude and wavelength in the main channel modulated by the existence of secondary channels?
- How far downstream the effect of the recirculation zone at the confluence affects the bed morphology in main and secondary channels?

As future work a Large Eddy Simulation (LES) numerical model of one of the bed morphology cases is proposed. This research will enlighten the role of the turbulence coherent structures in anabranching structures. Since on this experimental flume no velocity data will be obtained the LES model will be validated by comparison with a RANS model of the Kinoshita flume [5]. It is expected that by investigating the turbulent coherent structures bed load and re-suspension of sediment patterns will be found and associated with the migration of the planform.

APPENDIX C

PLANFORM DYNAMICS OF AN ANABRANCHING STRUCTURE NEAR IQUITOS. IMPLICATIONS ON THE LARGEST CITY IN THE PERUVIAN AMAZON RAINFOREST.

C.1 INTRODUCTION

The Peruvian Amazon rainforest occupies 76% of the total area of Peru [48]. However, most of the Peruvian cities in the Amazon rainforest do not have the same level of development as their counterpart cities located in the highlands or coastal regions in the country. Such is the case of Iquitos, the largest city in the Peruvian Amazon rainforest, [97]. Up to date, Iquitos does not have any main road that allows communication with the main cities of the country such as Lima, the capital of Peru. Thus, the main means of transportation for the city are fluvial and aerial. Iquitos city is surrounded by three rivers: Itaya, Nanay and the Amazon; from them the most morphodynamically active in the zone is the Amazon River, as will be shown in this study. Previous studies such as [77, 127, 173, 126, 34, 152, 129] have shown the importance of the multi-temporal satellite imagery to assess the migration of rivers in the Amazon rainforest, where little or no field data is available. In the case of the Amazon River at Iquitos city, [77] explained how the river used to be located next to Iquitos city and migrated in such a way that now the river next to Iquitos is the Itaya River (the smallest of the three rivers surrounding Iquitos). This has had implications for the transportation of goods to and from the city; in other words, the economy of Iquitos city is strongly related to the migration of the Amazon River and its tributaries at that location. Previous research

such as [77, 173] attempted to study the migration of the Amazon River at Iquitos using water levels, satellite imagery and some subjective field information such as interviews to the city dwellers. However, most of these studies, despite the valuable conclusions obtained from them, omit a very important component of the Amazon river migration, which is the hydrodynamics and bed morphodynamics of the river. In the last decade researchers such as [53, 67, 117, 81, 13, 28, 182] have investigated the relation between sediment transport and discharge in the Amazon River; with that aim, several field campaigns to measure velocities and sediment discharge were carried out between 2003 and 2012. Peruvian government agencies such as the Peruvian Navy and the SENAMHI (Servicio Nacional de Meteorología e Hidrología) have collected velocity measurements as shown in [50],[156],[51],[157] for several locations along the Amazon River including Iquitos city. However, the data do not have enough spatial resolution to allow a characterization of the flow dynamics in the Amazon River near Iquitos city. One way to overcome this issue is to use a numerical model and solve the hydrodynamics for the region of interest. Due to the planform complexity presented in the Amazon River a good approach is to use a two dimensional numerical model. The planform of the Amazon River is of the anabranching type, which is a characteristic of mega rivers ($Q_{mean} > 17,000m^3/s$) [135, 95, 118]. Anabranching rivers alternate from one single channel planform to a multichannel river planform along the valley with certain periodicity. Thus, in this planform a main channel, that behaves as a meandering river, is observed. It is well known that the bank displacement in meandering rivers is strongly related to the shear stresses [9]. Up to date several models have been developed to simulate the migration of meandering rivers. There are analytical models such as [96, 107, 190, 159, 4, 131, 132] and numerical models such as [113, 102]. On the other hand, [134, 100, 169, 140] attempted to develop numerical models for multichannel rivers. [100] developed a branches model, it uses an object based approach that considers the multichannel network as a set of meandering rivers; in the network, morphodynamic processes such as mid-bar channel formation and channel widening are modeled. The processes simulated in the branches model resemble the processes observed from satellite imagery in the anabranching structures of the Amazon River very well. However, the branches model, despite the use of physical equations for meandering migration, lack validation to be used in the Amazon River. [134, 140, 139] used

a cellular based approach in which the floodplain is modeled using a rectangular mesh with wet and dry cells; the wetting-drying process is controlled by solving a simplified set of the St. Venant Equations in which the momentum terms have been dropped. Although, the [139] model produces very realistic results when compared to actual planform of multichannel river networks, it lacks validation for the case of the Amazon River.

Since the state of the art for numerical modeling of multichannel river networks is still in the validation phase, research should be focused in filling this gap. Herein an analysis relating the historical water levels and satellite imagery with the results of a numerical model for one year is presented as a means to gain understanding on the Amazon River migration near Iquitos city. This analysis uses satellite imagery from the United States Geological Service (USGS) and field data collected in collaboration with the Peruvian Navy. The satellite imagery is utilized to analyze the planform evolution of anabranches and to compute the lateral migration. In addition, velocity profiles and bathymetry transects were collected during June 2011 field campaign. The data was utilized for calibrating a two dimensional model of the anabranching structure in the aim to analyze the correlation of migration with the hydrodynamics. Additionally, a 35 year period of water levels data was used from a gaging station located at Iquitos. The aim is to show the possible interaction historical variation of water levels with geometrical parameters on the anabranches, and with the planform migration.

C.2 SITE DESCRIPTION

The Digital Elevation Model (Figure C1 left) shows the floodplain of the Amazon River near Iquitos city, which helps to define the area where the river is able to migrate. This anabranching structure is located about 75 *km* to the North of the confluence of Ucayali River and Marañón River, where the Amazon River has its origin; also it is the third anabranching structure in the 75 *km* reach. To the southwest of the anabranching structure is located Iquitos (see Figure C1 right), which was located along the left margin of the Amazon River until the early 90's. Because of the dynamics of the anabranching structure, the Amazon

River in that region migrated to the North. And now, just a lake is left in front of Iquitos City, fed by the discharge of Itaya River which is connected to the Amazon River by a channel that used to be the Amazon River itself. The annual average discharge on the Amazon River at Iquitos City is $30,700 \text{ m}^3/\text{s}$ according to the values reported in [35] from a hydrometric gauging station placed 41 km downstream Iquitos. In the same report, the charts show that the discharge varies between $10,000$ and $55,000 \text{ m}^3/\text{s}$.

In addition, the average slope of the valley, computed from the Digital Elevation Model shown in Figure C1 is 0.018% . Also it can be observed, the valley is approximately 20 km wide in the area of the anabranching structure and the main anabranch averages a channel width of 1.3 km . From this image, it is clear to identify the areas where the channels are able to migrate.

C.3 HISTORICAL ANALYSIS

The analysis is divided into three sections. First the morphodynamic stages observed in the anabranches are described from the observations done using Landsat images; a description of the historical evolution of geometrical parameters is shown. Next, an analysis of water variation is done and a correlation analysis is carried out to find what parameters may affect the migration of the anabranches. Finally the results of a two dimensional hydrodynamic model (based on field measurements) are analyzed.

C.3.1 Planform evolution stages

Landsat images from the period between 1980 and 2012 were used for this analysis. The anabranch structure at Iquitos has five identifiable branches along the studied period. Figure C2 shows the planform evolution over a 32 year period, where the dynamics of each anabranch are observed; their temporal evolution is described next.

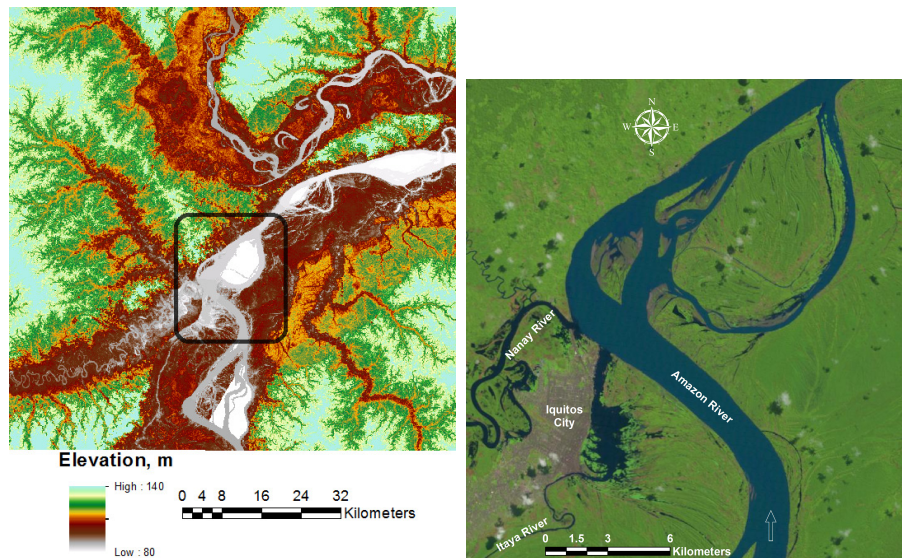


Figure C1: Left: Digital Elevation model in the surroundings of Iquitos anabranching structure. The Digital Elevation Model data was downloaded from Jet Propulsion Laboratory website. Right: Iquitos anabranching structure, located at geographical: Latitude $3^{\circ}42'S$, Longitude $73^{\circ}9'W$. Landsat image taken on June, 2011 (courtesy of USGS). Flow is from south to north.

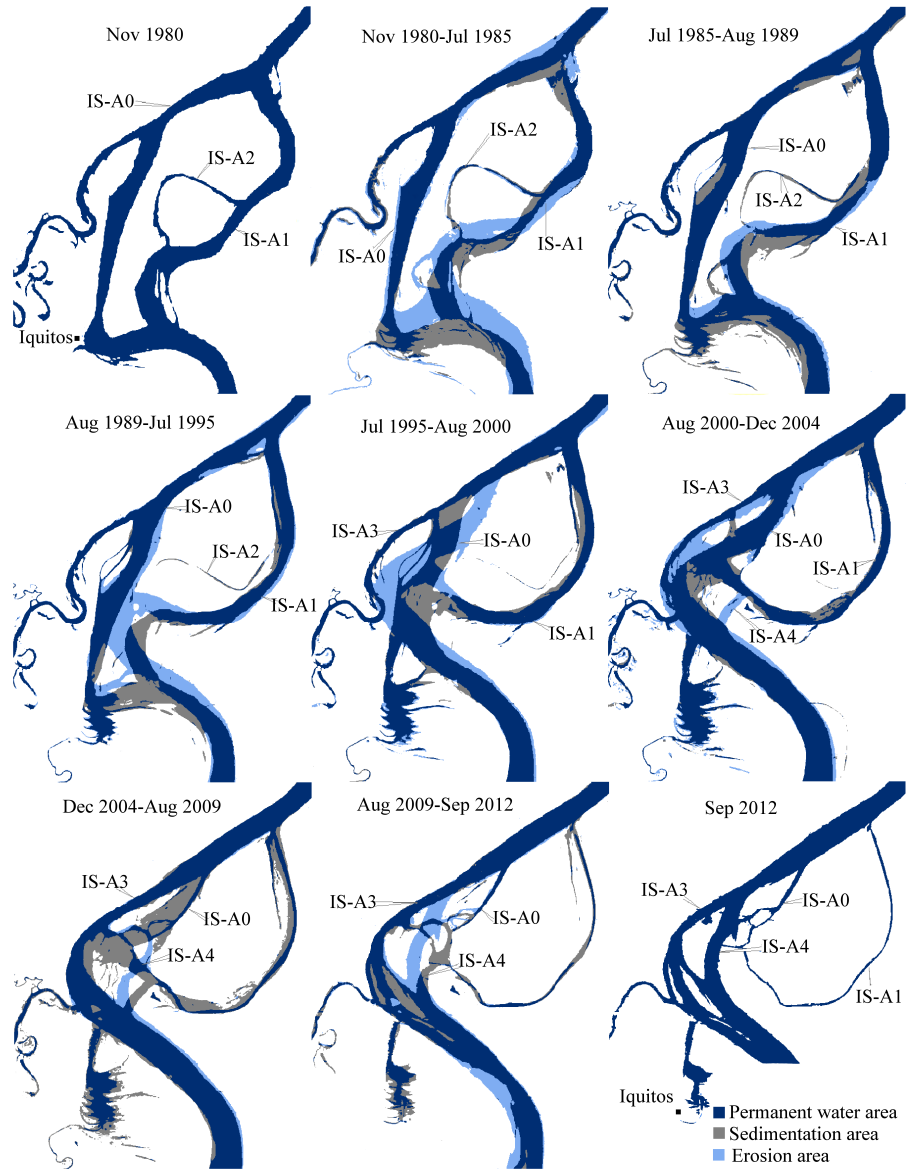


Figure C2: Planform evolution of Iquitos anabranching structure. Image at left top is the form of the anabranching in 1980 and the Image at right bottom in 2012. Intermediate images show the planform evolution on intervals of 5 years, dark blue are areas of permanent water during the analyzed period, light blue areas are erosion zones and grey areas represent deposition zones.

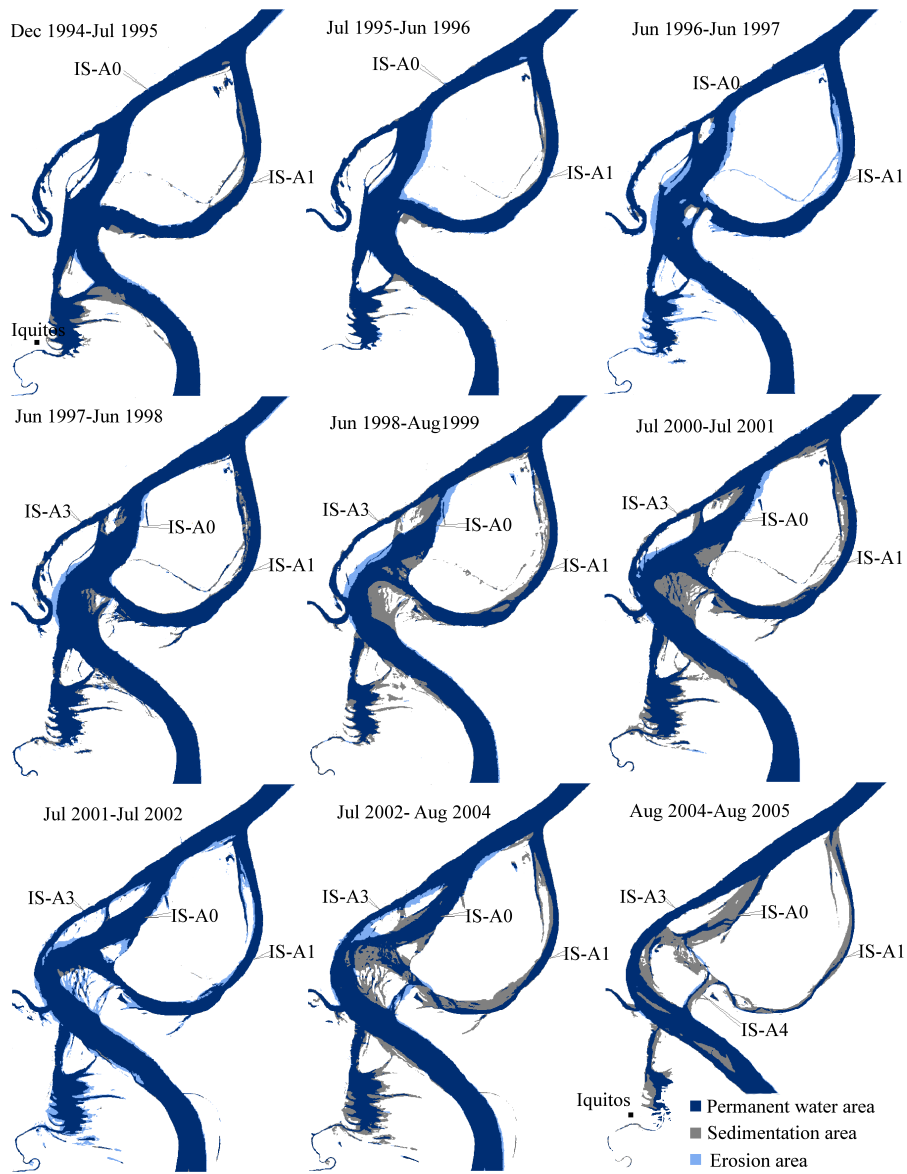


Figure C3: More detailed migration for the period 1995 through 2005. Dark blue represents zones of permanent water, light blue are zones of erosion, and gray are zones of deposition.

C.3.1.1 Anabranh IS-A0 *1980-1994*, during this period it is hard to define the main anabranh, since IS-A0 and IS-A1 have similar widths (see the first four images shown in Figure C2). The structure maintains the same topology, with the bifurcation point of the Amazon River into anabranches IS-A0 and IS-A1 migrating laterally to the North. It can be observed that the migration of IS-A0 is a consequence of the migration of the bifurcation point of IS-A0 and IS-A1. Notice that IS-A0 is closer to the valley boundaries (see Figure C1) than IS-A1, thus, IS-A1 has more freedom to migrate laterally.

1995-1998, an important event is observed by 1995, the migrating anabranh IS-A1 has reached IS-A0. This period is very active for the anabranh since two important events are observed; first the old initial reach which had Iquitos in its left margin, has abandoned and it remains until present day as a lake fed by the discharges of Itaya River. This can be observed clearly in Figure C3 left; also, the new planform of IS-A0 given by the collision of anabranh IS-A1 induces migration toward the left bank which produces the collision of the anabranh with the ending reach of the Nanay River.

1999-2004, during this period no important changes are observed in the anabranh, the migration rate is low, but continuous.

2005-2012, the anabranh starts a process of narrowing, as may be observed in the image for Aug-2004 - Aug-2005 shown in Figure C3. During this period the interaction with the newly developed anabranh IS-A4 is complex, producing a process in the anabranh to become shorter and narrower.

C.3.1.2 Anabranh IS-A1 *1980-1994*, the behavior during this period is similar to the one observed for anabranh IS-A0, the main migration processes are caused by the migration of the bifurcation node of Amazon River into anabranches IS-A0 and IS-A1.

1995-2004, after the collision with anabranh IS-A0 in 1995, IS-A1 has its starting point where the cutoff with anabranh IS-A0 happened. The main planform change during the period is the displacement of the bifurcation point of anabranches IS-A0 and IS-A1 caused by a growing point bar in the right margin of Amazon River at the beginning of anabranh IS-A1.

2004-2009, by the middle of 2004 a chute cutoff of 1.5 km long is developed between the Amazon River and anabranch IS-A1. A narrowing process starts to develop in the anabranch. An interesting process is observed in the reach contained between the bifurcation point where IS-A1 starts at IS-A0 and the confluence point of new anabranch IS-A4 with IS-A1. Landsat images show that during floods, the flow goes from northwest to southeast in that reach, however during droughts the flow is inverted, coming from the confluence of IS-A4 with IS-A1 through the bifurcation point of IS-A0 and IS-A1.

2009-2012, the anabranch IS-A4 is widening, and the former reach, defined earlier from nodes of bifurcation of IS-A0 and IS-A1 and confluence point of IS-A4 and IS-A2, is now part of anabranch IS-A4. At this point anabranch IS-A1 starts from the right margin of anabranch IS-A4 (see images after 2009 in Figure C2).

C.3.1.3 Anabranch IS-A2 *1980-1989*, this anabranch shows very low migration, it is mainly visible for the period 1980-1985 (see Figure C2), it keeps narrowing slowly and by 1989 the anabranch is abandoned since its initial point is no longer connected to anabranch IS-A1. An earlier study [77] shows a schematic of the structure for the 1960's, where IS-A2 is wider and part of anabranch IS-A1, by that time, there is just a narrow chute cutoff that latter would be part of anabranch IS-A1, while IS-A2 has just started a narrowing process.

C.3.1.4 Anabranch IS-A3 *1998-2003*, this anabranch is not self developed, it becomes part of the structure after the anabranch IS-A0 migrates to the left and collides with the final 6 km reach of Nanay River by 1998. The new island between IS-A0 and IS-A3 is eroded on its Southwest extreme during this period (see image for Aug 2000 - Dec 2004 in Figure C2). A slight process of widening is also observed.

2004-2012, the narrowing process observed in IS-A0 has its counterpart in IS-A3, which starts a widening process by 2004. After 2005 it is clear that the main anabranch is IS-A3. An interesting observation for this anabranch is its low migration rate, in fact its main planform changes are related to the widening process. This may be explained by the location

of the anabranch with respect to the floodplain; Figure C1 shows that the anabranch is in the left boundary of the geologic valley, and cannot migrate in that direction any more.

C.3.1.5 Anabranch IS-A4 2000-2005, by 2000 a chute cutoff starts to develop from the Amazon River through anabranch IS-A1; this is the origin of anabranch IS-A4 (see pictures of Jul 2000-Jul 2001 and Jul 2001-Jul 2002 from Figure C3). A widening process is observed during the period.

2006-2012, The first 2 km of the initial part of anabranch IS-A1 becomes part of anabranch IS-A3 by 2006, the interesting part is that the flow in that reach goes in the opposite direction (see images for Dec 2004-Aug 2009 and Aug-2009-Sep 2012 in Figure C2) of when the reach was part of IS-A1, this for low discharge conditions. Important migration processes are observed during this period, and the anabranch keeps widening. As will be shown later with the historical analysis of widths, this anabranch becomes the main channel after 2006.

Before concluding the descriptive analysis based on Landsat images it is important to remark that the images utilized were the ones with best quality (low coverage of clouds), and that the level of water on the river is not always the same, in particular for 2005 there was a drought in the region [62], that is the cause of the low levels in the water observed in that year as can be seen on the Figure C3, image for Aug 2004-Aug 2005.

C.3.2 Planform evolution and migration

Landsat images allowed a geo-referenced analysis of the historical geometric evolution of anabranches. The images that had enough quality were utilized for estimating the planform evolution and are listed in Table C1 with the corresponding water level recorded on the hydrometric station in Iquitos for that date. The process for getting the geometrical parameters and migration consists of four stages: 1) The banks for all anabranches are digitalized for all the images listed in table C1. 2) The centerline is computed as the geometrical center

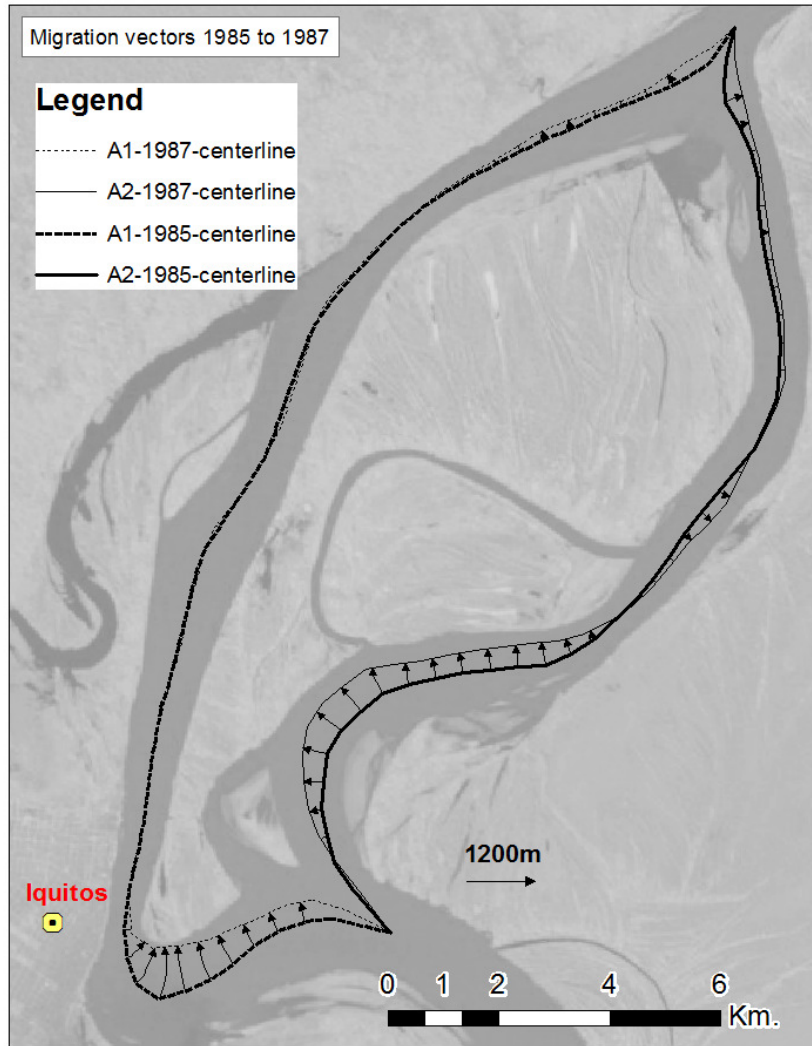


Figure C4: Migration rate is obtained by calculating the displacement of nodes from one centerline to its next stage in time. The analysis was performed using the NCED Stream Restoration Toolbox [119]

of the banks 3) Sinuosity is computed from centerlines, width of the channel is computed as the area between left and right margin, divided by the length of the centerline. 4) Migration rate is computed by calculating the distance when the centerline moves between two consecutive dates, Figure C4 shows the process of this last stage. Figure C5 shows the historical evolution of the surface elevation (A), channel width (B) and sinuosity (C) for the anabranches; it may be observed that the variations of width are linked to the stages described for each anabranch in the previous subsections. It should be noted that there are variations in width caused by the water level variations, this is expected since the banks of the river are not vertical, however despite the noise caused by using banks that correspond to different water levels, the general tendencies on channel width and sinuosity are clear in the charts. The evolution stages of the anabranches also can be classified by changes in the width as described next based on the trends shown in Figure C5B.

1980-1995, anabranches IS-A0 and IS-A1 have similar widths, averaging 1200 m; anabranch IS-A2 is detached from the structure by 1989.

1995-1998, collision of anabranches IS-A0 and IS-A1 (see image Aug 1989-Jul 1995 in Figure C2), anabranch IS-A0 gets wider since that event, up to 2000 m by 1998; on the other hand IS-A1 starts a narrowing process; the apparent cause of both processes is the reconfiguration of the structure that redirects a larger percentage of the flow by IS-A0 (see images from 1995 to 2000 on Figure C3).

1998-2000, the new anabranch IS-A3, which was originally part of the final reach of Nanay River (see image for Jun 1997-Jun 1998 in Figure C3), is developed and starts a widening process. Anabranch IS-A0 appears to reach an equilibrium state for the width during this short period; anabranch IS-A1 continues narrowing.

2000-2003, after the development of anabranch IS-A4 by 2000 it is observed that IS-A0 starts a narrowing process. IS-A1 maintains the narrowing process started in 1995 and is approximately 620 m wide by the time, while IS-A3 and IS-A4 maintain the widening process.

2003-2006, anabranch IS-A3 doubles its width in 2003 compared with its original width by 2002, this may be observed in Figure C3, the areas of widening are the inlet and outlet

Table C1: Dates for migration analyses, with the period in days between Landsat images processed and water elevation on the river.

Date	Period (days)	Water Level (m.a.s.l)
1980-11-08	0	84.01
1985-06-12	1677	84.21
1986-06-15	368	85.65
1987-09-06	448	79.55
1989-08-26	720	80.85
1991-09-17	752	78.2
1994-06-21	1008	87.06
1995-07-10	384	81.93
1996-06-26	352	81.33
1997-06-29	368	83.58
1998-06-18	354	82.23
1999-12-28	558	84.38
2000-07-14	199	85.16
2001-05-31	321	86.14
2002-07-21	416	84.03
2003-08-25	400	80.56
2004-12-24	487	84.28
2005-06-19	177	83.14
2006-02-14	240	85.53
2007-03-21	400	84.82
2008-04-08	384	86.25
2009-08-17	496	80.98
2010-12-07	477	80.34
2011-06-20	195	84.33
2012-09-18	456	77.7

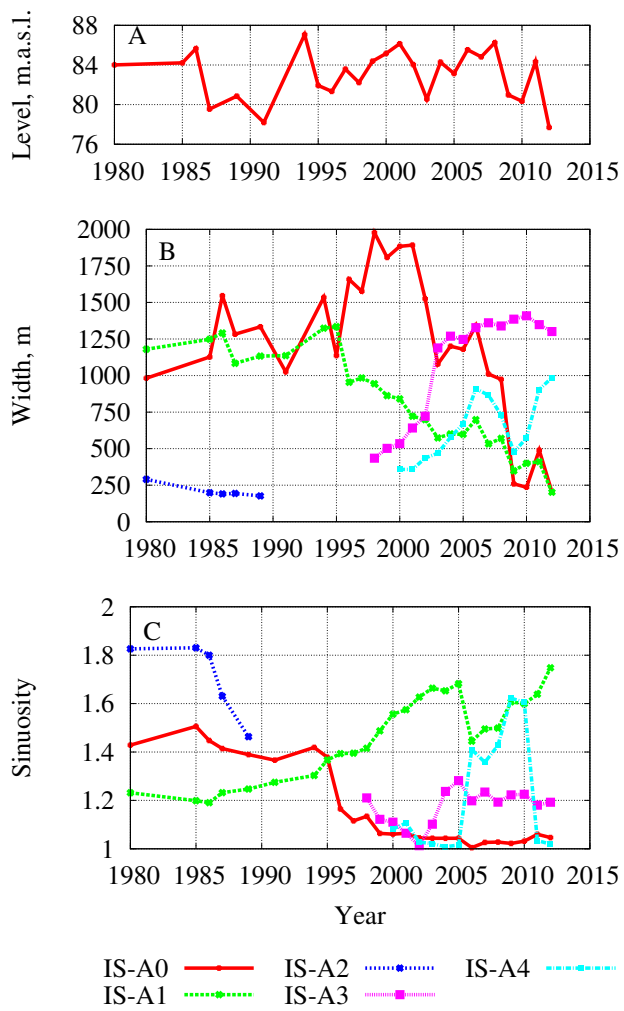


Figure C5: Historical evolution of channel width and sinuosity of the anabranches. Upper chart shows the water surface level in the river during the date of the Landsat utilized for the analysis. These measurements are at the Iquitos station.

of the anabranch. Also Figure C5 shows a widening process for IS-A0 in the period, having a similar width to IS-A3.

2006-2012, anabranch IS-A0 narrows faster, IS-A1 maintains the same pace and by 2012 both anabranches are around 200 *m* width; IS-A3 is clearly the main anabranch, and anabranch does not have a regular behavior, changing width constantly.

When comparing channel width versus sinuosity (Figure C6) for the anabranches of Iquitos structure, it is interesting to observe that there is a pattern of lower sinuosity for wider channels when the points for all anabranches are plotted. In the case of individual anabranches, the evident trend is observed in anabranch IS-A1, where width and sinuosity are clearly anticorrelated, for the other anabranches points are scattered. Also it may be observed that anabranch IS-A2, which averages 200 *m* width has the highest sinuosity of all anabranches; anabranch IS-A0 has the most irregular behavior, since it has similar sinuosity for the cases when it is wider or narrowest, however it has a subset of points with that resemble the behavior of IS-A1, in the sense that width and sinuosity are anticorrelated; the same behavior is observed for IS-A4. Anabranch IS-A3 does not show any clear pattern in Figure C6, however it should be noted that it does not migrate freely since is constrained on the left by the valley's boundary (see Figure C1). It should be remarked that for this anabranching structure the displacement of the bifurcation and confluence points is constant and considerable when is compared to the lateral migration of the channels; since the sinuosity is the relation of length along the channel to the valley distance from the start to the end of the anabranch, changes in sinuosity in this case are produced by two processes: the lateral migration of the channel, and the migration of beginning and ending points of the anabranch. This can be particularly noticed on anabranch IS-A2, which has a very low migration rate but an important change in sinuosity, as may be observed in Figure C6, caused mainly by the migration of its starting point.

Migration is computed by the displacement of the centerlines, as explained before. For the analyses, the average migration is used, which is computed as

$$AM = L^{-1} \int_0^L |M| dx \quad (C.1)$$

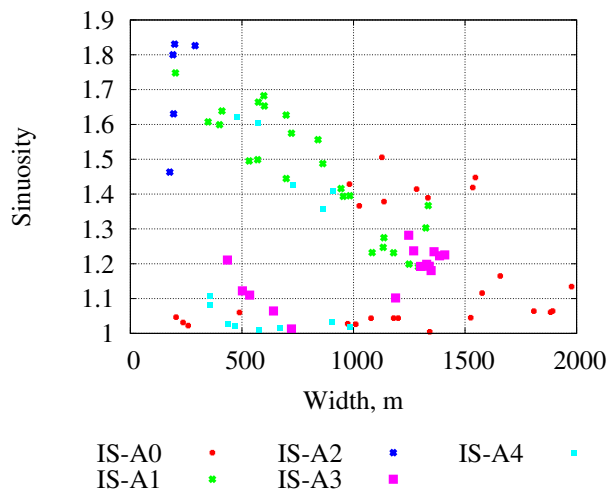


Figure C6: Channel width versus sinuosity observed in Iquitos Anabranching structure.

where AM is the average migration for the anabranch in m , L the length of the anabranch in m , and M the pointwise migration as shown in Figure C4 with the vectors of displacement. Since there are important changes in the anabranching structure over the period of time considered for the analysis, migrations were computed for every anabranch in the cases when there was not discontinuities in the shape of the anabranches (i.e. development of new anabranches). Dates of images utilized in the analysis of migrations are shown in table C1, Migrations are computed between the consecutive dates shown there. The values computed for cases where there is important differences in water surface elevation from initial to final Landsat images are omitted. After filtering out such dates, the values kept for further analysis.

C.3.3 Variation of water surface elevations

Variation on the water surface elevation on the river has been identified as a strong component of migration processes, mainly linked to bank failure since rapid drops in the water level may produce bank failures [114, 115, 116, 131]. Herein, our interest is to identify the linkage between water level variations and migration rates. This is possible since there are daily

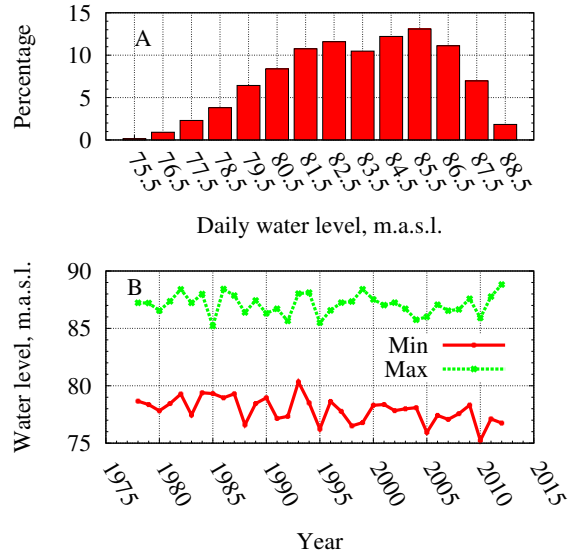


Figure C7: Histogram of daily historical water surface elevations recorded in Iquitos Hydrological station. Lower chart shows the minimum and maximum levels recorded per year.

records of water surface elevation for the 32 years utilized for the analysis. The historical water levels recorded in the Iquitos gaging station have the temporal distribution shown on the histogram in Figure C7A; it may be observed that the water level has variations about 10 *m* over the year. Figure C7B shows the maximum and minimum levels since 1978, it should be noted that the maximum levels have maintained a constant average of about 86.5 *m.a.s.l.* while the minimum values have a permanent decreasing trend over the years (an average rate of 5% per year). Lowering in annual minimal levels in the Amazon River is explained by a consistent decrease in the height of precipitation which is translated to a decrease in the discharges on the river. This is observed in historical records from the period 1970-2004 by [62], and they explain that the origin of this phenomena is caused by global climatic variations.

The first approach consists on linking the statistical characteristics of water surface elevation with the migration parameters such as the maximum, minimum, average, and standard deviation of daily water levels. Thus, these parameters are computed within the

periods of consecutive Landsat images utilized for computing the migration, in that way, statistical parameters and computed migration are for the same period of time. Three approaches are utilized to represent the migration, the first is the average migration computed with Eq. (C.1); the other is the average migration rate, which is computed as

$$AMR = AM/Period \quad (C.2)$$

where AM in m is the average migration computed with Eq. (C.1), and $Period$ is the number of days between the two Landsat images utilized to compute the migration. The other metric utilized is the normalized average migration which is computed as

$$NAM = AM/B \quad (C.3)$$

where NAM has units of m/m , and B is the channel width in m . These three approaches are plotted in Figure C8.

Correlations for the statistical parameters of water level, sinuosity and channel width were computed for the five anabranches and the results are shown in Figure C9 for both, average migration and normalized average migration. The correlations computed using the average migration rate, AMR resulted in very low values of correlation and are omitted for the rest of the analyses. Figure C9 shows correlations of different parameters versus average migration and normalized average migration, we can see correlations of different signs for channel width and sinuosity, thus no clear pattern was found; and the only parameter that shows a more consistent pattern at almost all the correlations with positive sign is the maximum elevation recorded in the period (the only anabranch with negative correlation is IS-A3, the one located on the limit of the valley). A second analysis consists on computing the maximum variation observed on water levels DE . Variations DE were separated in positive $DE(+)$ and negative values $DE(-)$, under the hypothesis that the migration linked to them may have different physical processes. An important parameter to define is the adequate period of time to compute the water level variations since they should be long enough to allow the interaction of the flow with the banks or the development of mechanical processes on the bank material. Since it is not known *a priori* the adequate period of time, DE , water variations were computed for different periods of time, and the correlation analyses

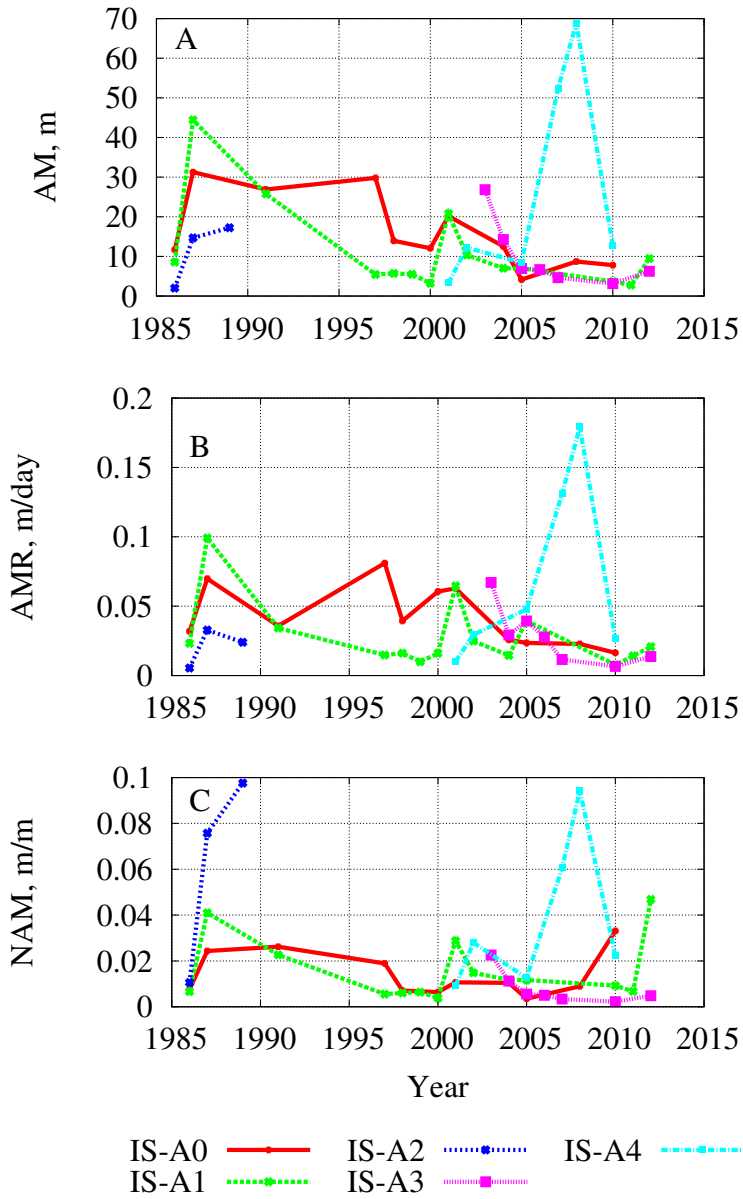


Figure C8: Migration computed with displacements of centerlines. AM: averaged migration, AMR: averaged migration rate, NAM: normalized migration rate

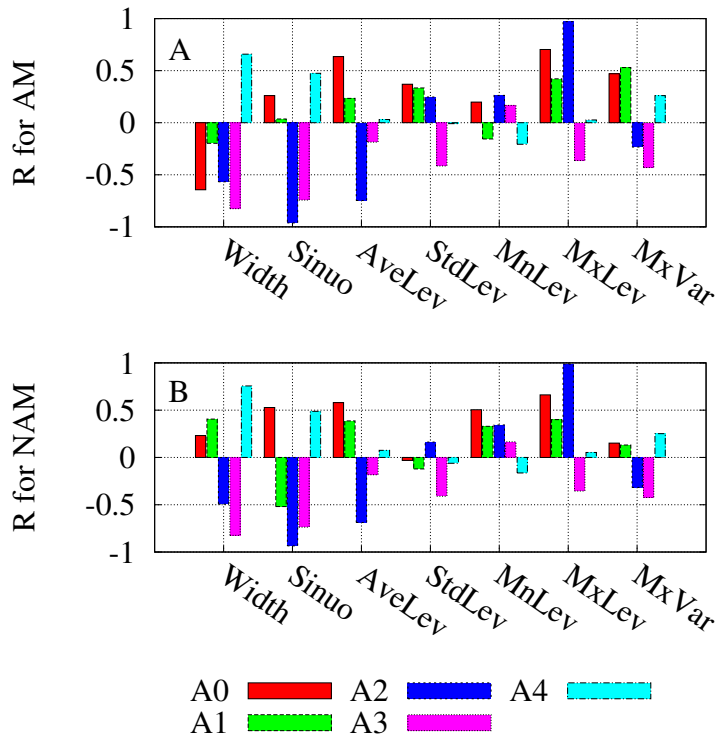


Figure C9: Correlation of average migration (AM) and normalized average migration (NAM) versus channel width (Width), sinuosity (Sinuo), average elevation (AveLev), standard deviation of daily water level variation (StdLev), minimum water level (MnLev), maximum water level (MxLev), maximum water level variation in the period (MxVar), all computed with the daily water level recorded between the dates of the two Landsat images utilized for computing the migration.

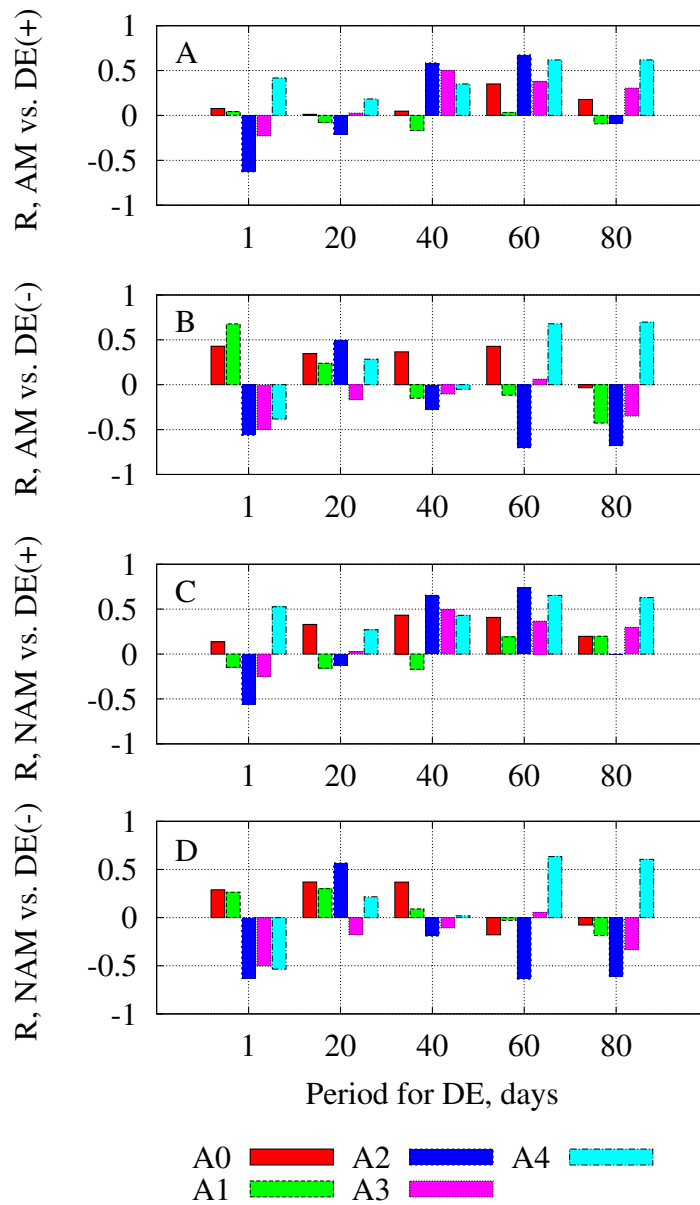


Figure C10: Correlation, R , for migration versus maximum water level variation (DE) negative and positive computed for different intervals of time, in the plots AM stands for average migration and NAM for normalized average migration.

were computed for all of them versus the average migration, average migration rate and normalized average migration. Again, the average migration rate was the parameter with the poorest correlation values. Highest correlation values are obtained for positive values of water variation, $DE(+)$, in periods of 60 days, as can be observed in Figure C10 for both migrating parameters, average migration and normalized average migration, however as can be seen in Figure C10C, the highest values are obtained for normalized average migration.

Figure C11A shows the histogram of water level variation (DE) observed in periods of 60 days, it shows that the probability of occurrence for higher positive water variations decreases faster than for the case of negative variations (recession), and this effect is reflected in the annual maximum variation as is observed also in Figure C11B and Figure C11C.

C.3.4 Field Measurements and Two-dimensional Shallow Water Model

During June, 2011, we have collected bathymetry and velocity data in this anabranching structure (see Figure C12). Velocity profiles were measured with an acoustic Doppler current profiler (aDcp), for sections with labels starting with 14, data was collected on June 14th, sections labeled starting with 15 where collected during June 15th (Figure C12). Bathymetry data was obtained by means of a single beam echo sounder in transversal sections every 500 meters [50]. Two dimensional modeling of free surface flow is a valid approach when the vertical scale is orders of magnitude lower than horizontal scales; in such cases the Navier-Stokes equations are simplified by the St. Venant hypotheses, which involves the consideration of hydrostatic distribution of pressure, negligible vertical accelerations [92, 3]. Those assumptions lead to the St. Venant Equations:

$$\frac{\partial h}{\partial t} + \vec{U} \cdot \nabla h = 0 \quad (\text{C.4})$$

$$\frac{\partial U}{\partial t} + \vec{U} \cdot \nabla U = -g \frac{\partial z}{\partial x} + S_{fx} + \frac{1}{h} \nabla (h \nu_t \nabla U) \quad (\text{C.5})$$

$$\frac{\partial V}{\partial t} + \vec{U} \cdot \nabla V = -g \frac{\partial z}{\partial y} + S_{fy} + \frac{1}{h} \nabla (h \nu_t \nabla V) \quad (\text{C.6})$$

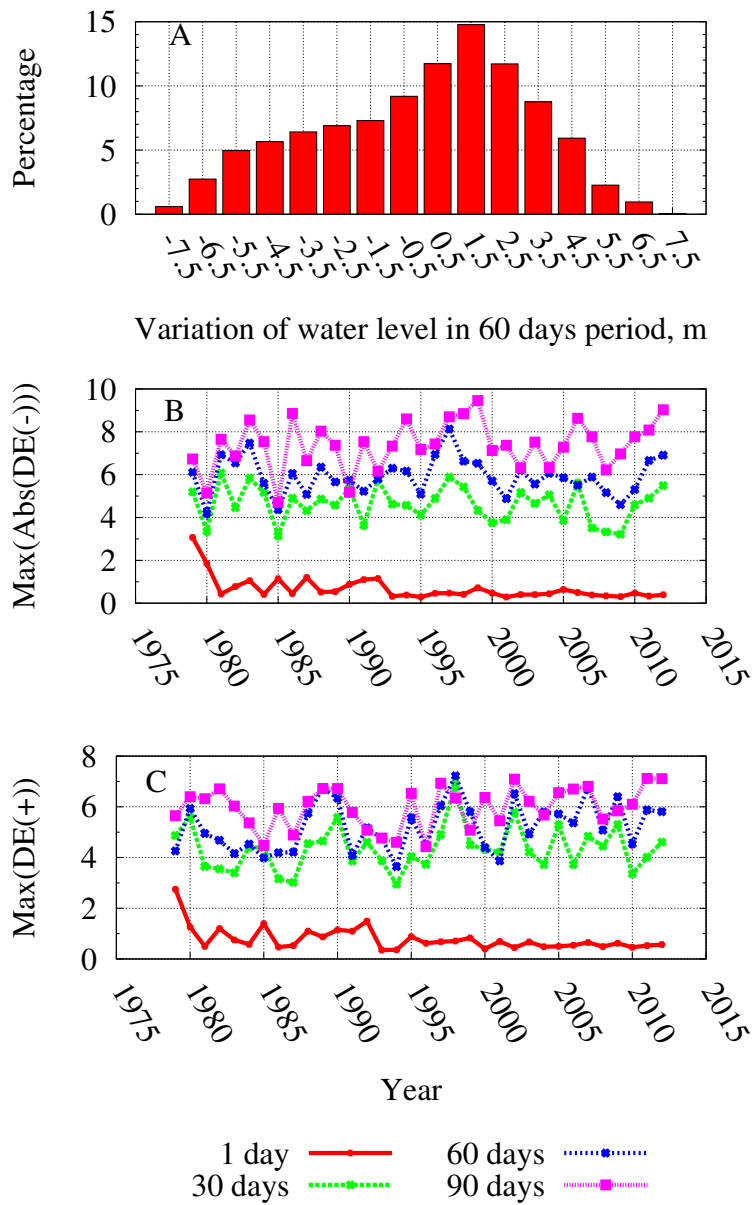


Figure C11: A. Histogram of water level variation (DE) in periods of 60 days. B. Maximum negative variation on water level observed (recession) per year. C. Maximum water level increase observed per year.

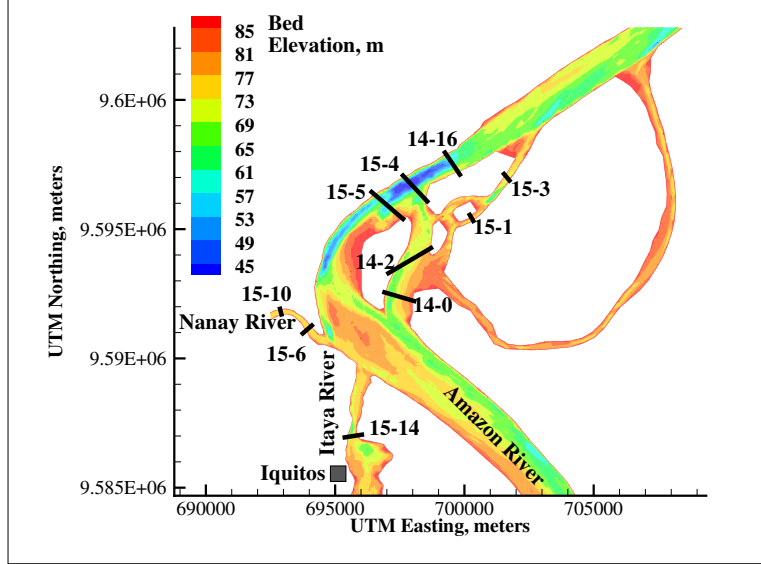


Figure C12: Transversal sections for velocity profiles and bathymetry collected during June 2011

where h is the water depth in m , U and V the depth averaged velocity along axis x and y respectively, in m/s , z the elevation of the bed, in m and ν_t the turbulent viscosity, in m^2/s , S_{fx} and S_{fy} are sink terms of momentum, in m/s and for the case modeled herein applies for bed friction.

The velocity profiles obtained during the 2011 campaign are utilized to calibrate a two dimensional model for the anabranching structure. The goal of modelling the flow with St. Venant Equations is to obtain the hydrodynamic characteristics of the flow in the anabranching structure and compare it with the planform evolution of the anabranches to define possible cause-effect links. For this purpose we utilized Telemac-2D, which solves the St. Venant Equations (C.4)-(C.6) with the Finite Element Method in a irregular mesh, [92, 149].

For the numerical simulation, a mesh formed by 106,202 triangular elements is created, steady flow conditions were modeled. The discharges on Amazon, Itaya, and Nanay Rivers are imposed to $33,443 m^3/s$, $242 m^3/s$ and $1,675 m^3/s$ respectively. Velocities measured with aDcp were compared to the modeled ones, and the model was calibrated by adjusting the bed friction coefficient, the friction stress was computed with Manning equation; the coefficient

applied to the entire domain for reproducing the measured velocities was $n = 0.03$. This is not completely valid, since each anabranch may have different bedforms and thereby, different friction coefficients. However since the topography data is not fine enough to detect the height of dunes, the best approximation is to calibrate with constant Manning coefficient for the entire region. Figure C13 shows the comparison of measurements versus the modeled for vector velocities and their magnitude in some of the sections. It is observed that the flow patterns are captured well by the numerical model, in the sections shown plots of velocity magnitude measured versus modeled have different degrees of dispersion, but all of them follow the identity line tendency.

The hydrodynamic results obtained from the simulation with Telemac-2D are contrasted with the areas where morphologic changes are developed after June, 2011 in the anabranching structure. Figure C14A shows the planform evolution observed during the period from August 2011 through September 2012, and the flow characteristics computed by the two dimensional model: velocity field on Figure C14B, bed shear stresses on Figure C14C, and water depth on Figure C14D. Table C2 shows the water surface elevation for the dates of Landsat images utilized in the comparison; for the image of August 2011 water surface elevation was 80.35 m.a.s.l. meanwhile for image of September 2012 the water surface elevation was 77.75 m.a.s.l. , 2.6 m lower, that explains the presence of the islands on anabranch IS-A3 in front of the outlet coming from Itaya River; nevertheless, it is observed that the main migration is given on anabranch IS-A4. Figure C14 shows that even if the velocities are above the average on IS-A4, they are not the highest in the domain. Also the dried areas shown in Figure C14 may not be directly associated to bank advance due to deposition since images shown were taken for flow conditions where the water level has a difference of 2.6 m and the shallower areas of the bed are exposed; however, the fact that the area dried during the recession of water level indicates that it is a zone of deposition, and numerical simulation shows that it is linked to zones of lower velocities, this may be observed in the entrance of anabranch IS-A1 and in the confluence of anabranches IS-A3 and IS-A4, where the northern part of the island has displaced narrowing anabranch IS-A3.

Regarding the migration caused by fluvial erosion, a complementary process that can enhance the migration, according the observations based on Landsat imagery for dates in

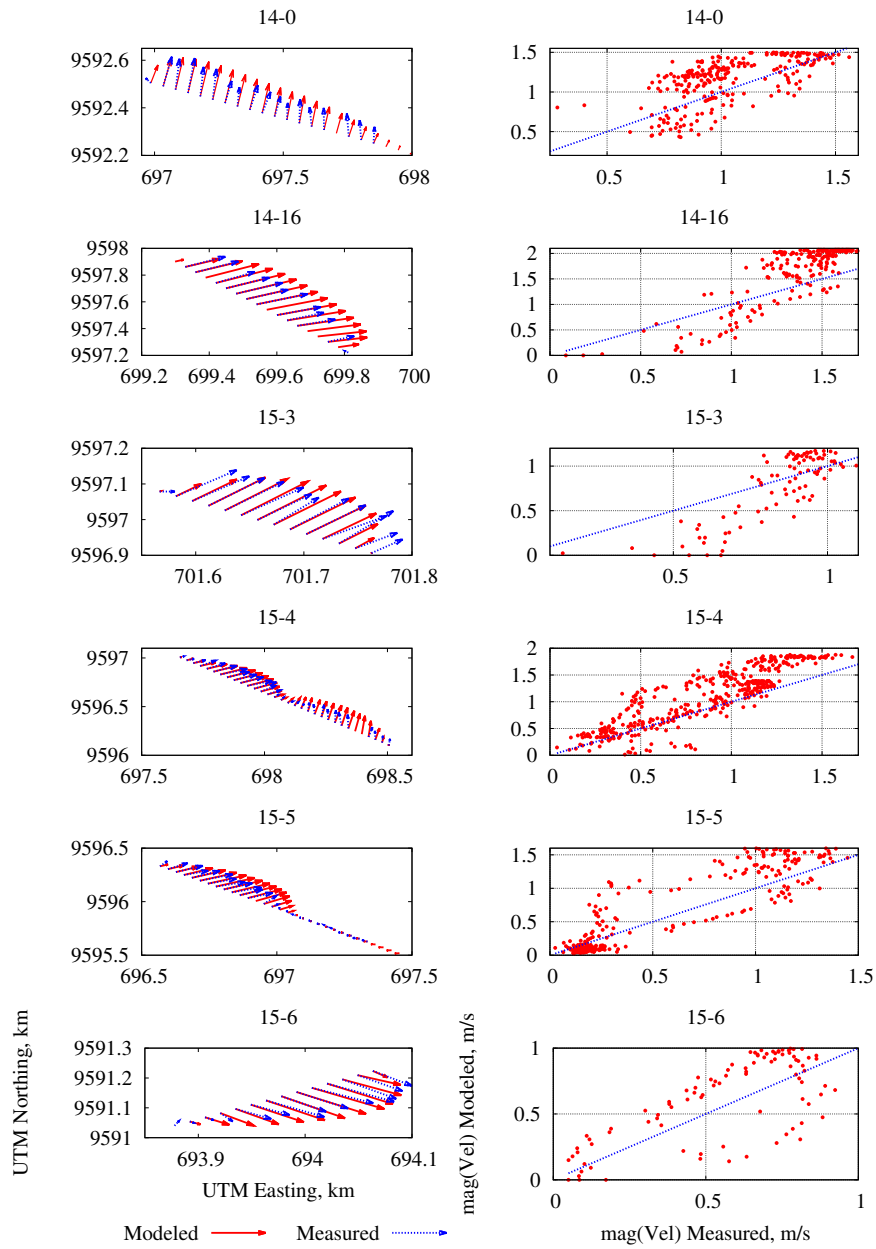


Figure C13: Comparison of velocities measured versus modeled for some of the sections shown in Figure C12. In the left plots show the modeled and measured velocity field and in the right the comparison of velocity magnitude.

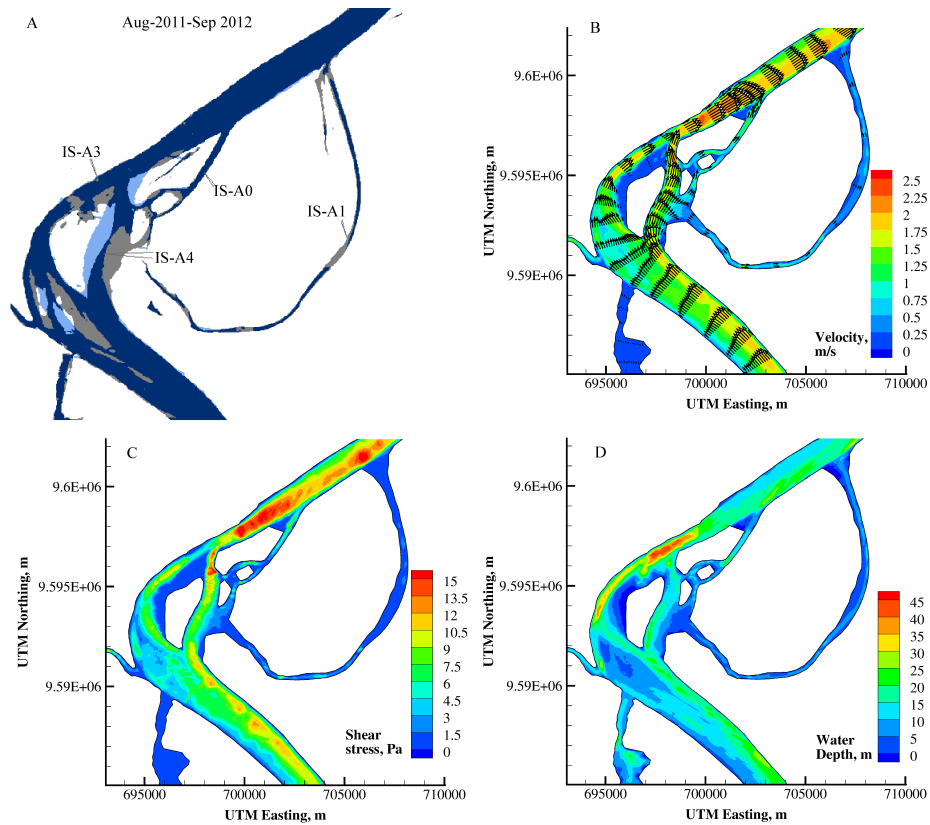


Figure C14: Planform migration compared with the hydrodynamics. A. Migration of anabranch IS-A4 since the initial condition on 2011. B. Velocities computed with Telemac-2D with the hydraulic conditions on June, 2011. C. Computed shear stress in the bed. D. Computed water depth.

both dry and wet season, is the variation of water surface levels. Figure C15 shows the migration over the period from June 2011 through September 2012. It shows a process of wetting and drying caused by the variations of water levels which depend on the seasonality of the flow; in the period from June through August 2011 there is a drop in the water level of 3.9 m, a couple of islands emerge and the shallower bed areas at the entrance of anabranch IS-A1 are exposed; no important signs of erosion are visible; the left bank of anabranch IS-A4 remains in the same position, which may indicate either that the bank is vertical or that the migration produced in the bank is not visible because of the decrease of 3.9 m on water level. The next image compares the bank position evolution for the period from August 2013 through January 2012; water level has an increase of 5.9 m, the shallow bed areas exposed at the beginning of the period are flooded again, and a displacement of the left bank of IS-A4 is observed; for the period January - March 2012 the water level increases another 1.5 m, (see table C2) and it may be observed that left bank of IS-A4 continues migrating. For the last period, from March to September 2012 there is a decrease in water level of 10.1 m and islands and shallow bed zones are dried again, also a small migration on the left bank of anabranch IS-A4 may be observed. The important aspect to remark upon here is that the highest migration was developed during high levels of water.

C.4 DISCUSSION

The Landsat images that cover the period 1980-2012 show that Iquitos anabranching structure is very dynamic, with anabranches developing and disappearing constantly. Digitalization of Landsat images allowed tracking of historically geometrical changes on anabranches. As may be observed in Figure C5, channel width is always changing rapidly for all anabranches, except for anabranch IS-A3, which is explained because is on the left limit of the valley (see Figure C1), which constrains its morphodynamic changes. Sinuosity is also changing in time, but we must be careful in the sense that not all the changes are caused by an increase or decrease of curvature in the channels, but also by the displacement of bifurcation and confluence points, and by the creation of new anabranches; that is the case of anabranch IS-A2

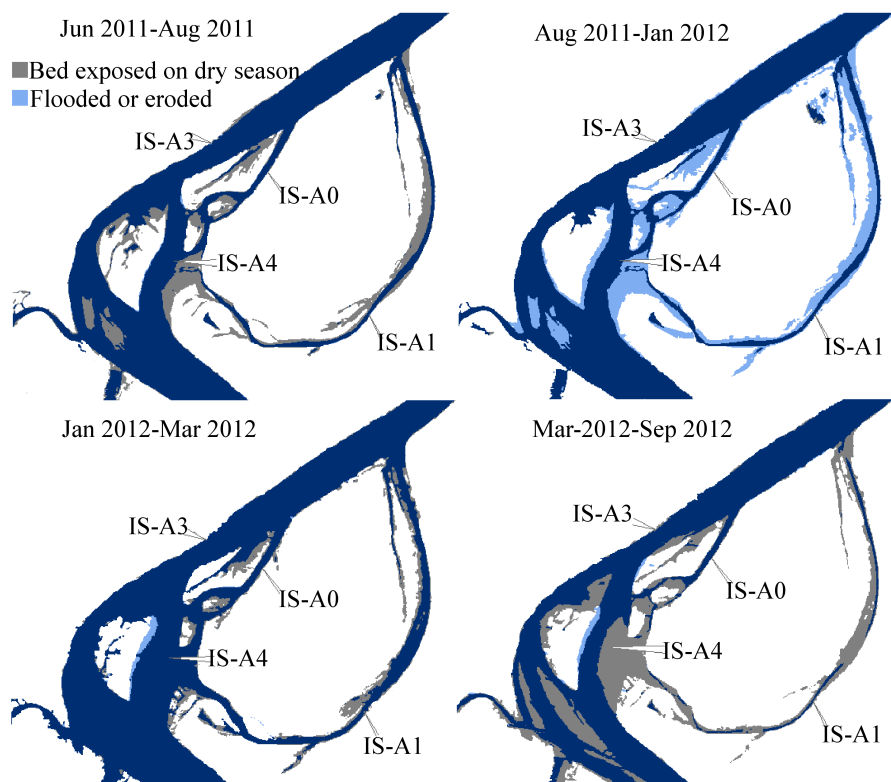


Figure C15: Migration from 2011 through 2012 and variation water levels. Images show the areas of bed exposed during dry season and the areas flooded and eroded during wet season.

Table C2: Water surface elevations in Iquitos after June, 2011 for Landsat images available until September, 2012

Date	Water surface elevation, m
2011-06-20	84.35
2011-08-07	80.45
2012-01-22	86.35
2012-03-26	87.85
2012-09-18	77.75

which shows important changes in sinuosity but is caused by the migration of the bifurcation point where it starts, caused by the migration of anabranch IS-A1. Analysis of widths make possible to define the main anabranch, which may not be clear at first sight for some periods of time, as is shown in in Figure C5B.

Migration analyses were focused on lateral displacement of anabranches; however it should be noted that there was also migration of bifurcation and confluence points, which in fact is the main process observed from 1980 through 1995, where the bifurcation of Amazon River into anabranches IS-A1 and IS-A1 is a continuous process until the collision of anabranch IS-A1 with IS-A0. At this point the anabranch structure is on the left limit of the valley as may be observed in the Digital Elevation Model shown in Figure C1, anabranch IS-A4 keeps migrating to the left and anabranches IS-A0 and IS-A1 started a narrowing process by 1998 and 1995, in 1995 because of the collision of both anabranches, and in 1998 by the collision of IS-A1 with the ending 6 *km* reach of Nanay River, which became anabranch IS-A3.

Correlation analysis show the highest values for normalized average migration versus maximum water level increase in 2 months. An interesting result observed in the analysis of correlation is the fact that from the different parameters of correlation computed with Eqs. (C.1), (C.2) and (C.3), from Landsat images, the average migration rate does not show high correlation when is compared to one observed with average migration. We can hypothesize that the reason of such behavior may be understood if we consider that the migration is episodic and triggered by specific events. The correlation analysis (see Figure C10) shows that the triggering event for lateral migration is a rapid increase in the water level, or most probably, an effect produced by it, as the increase of velocities due to a greater discharge in the river. Also, the normalized average migration, *NAM*, is the one that gets a greater correlation for positive water levels variation in periods of 2 months (see Figure C10C). We interpret that in the sense of migration being a function of the discharge, since it may be interpreted in general for an anabranching structure that the discharge is directly related to the channel width. A possible explanation for the migration to be correlated to fast increases of water level is that during high water levels the flow reconfigures the shape of anabranches beginning from the top of the banks, such changes are kept after the flood. This may be

confirmed by Landsat images shown in Figure C15, where the important migration processes are observed after a flood.

Also, we expected that negative variations of water may have a larger correlation with the lateral migration on anabranches since fast drop in water levels does not allow the banks to drain at the same rate and that can cause bank collapse and the implied migration of the bank, However it was not confirmed by the correlation analyses.

Numerical computations of the flow were done with steady flow conditions and fixed bed using bathymetric data collected during June 2011 by the Peruvian Navy. Results show, as expected, that erosion happens in zones where bed shear stress is greater than average, but the opposite condition is not held, meaning that not all the places of higher shear stress have high migration rates. Bank migration is then caused by a series of processes acting together. A future approach for modeling must include unsteady flow with bed evolution and bank migration with the aim of gaining an understanding of their complex interaction in anabranching structures.

At this point there are models that allow modeling unsteady flow and bed morphology but lack the process of bank migration. Our research group is working with the development team of Telemac-2D for incorporating on it a module for bank migration, so in the future it will be possible to model more complete morphologic process on anabranching structure with physical based approaches.

C.5 CONCLUSIONS

Iquitos anabranching structure shows a very dynamic planform behavior. Channel width on all anabranches exhibit a constant change; the only exceptions where low amounts of widening or narrowing occur are for anabranch IS-A0, on the period 1980-1995, and anabranch IS-A3 for the period 2003-2012 (see Figure C5), which may be explained by their position on the left boundary of the valley, constraining their evolution.

There are specific events that change the evolution trend of a channel, as is the case for anabranches IS-A0 and IS-A1 on 1995, when they collide and anabranch IS-A0 increases its

widening speed for some years and IS-A1 starts a narrowing process (see Figure C5). All the events that change the trend of channel width evolution are linked to reconfiguration of the channels caused by cutoffs. One of the usual metric parameters utilized in the analysis of anabranching structures is the sinuosity, we computed such parameter for different stages of the anabranching structure and found that the change is not only linked to lateral migration of the channels but to migration of bifurcation points where the anabranches start, modifying both parameters involved in the sinuosity: the straight distance between the initial and final point of the anabranch, and the length of the channel. Therefore, this process may alter the sinuosity magnitude without an observable lateral migration of the channel.

Morphodynamic processes observed in the anabranching structure involve lateral migration of the channels and migration of the bifurcation and confluence points. An analysis of correlation was carried out to identify geometrical parameters and variation of water levels as determining components on the magnitude of lateral average migration of anabranches. The process with highest correlation against lateral migration was the fastest increases of water level on periods of 2 months (see Figure C10). Three metrics were utilized to describe the migration: average migration, average migration rate, and normalized average migration (normalized by channel width). The most representative metric of migration was the normalized average migration, computed as is indicated by Eq. (C.3); the highest correlation values resulted for this parameter. We hypothesize that the reason why normalized average migration gives the highest correlation values is that migration is influenced by the discharge in the anabranch, which is represented in a certain way by the channel width.

Numerical modeling carried out for steady flow conditions shows coincidence with magnitude of shear stress and zones of erosion and deposition near the banks, in the sense that erosion is present in zones of high shear stress, and deposition in zones of low shear stress (see Figs. C14A and C14c). Also, for the case of erosion, results suggest that shear stress is just one of the components that triggers bank erosion, since lateral migration is linked to high shear stress zones, but the opposite statement is not held by the results of the modeling, it can be observed for example in the reach of Amazon River upstream the anabranching structure, it has the same magnitude of bed shear stress near the right bank that the one observed in anabranch IS-A4, but the only migration is present in such anabranch.

Migration is a constant in the anabranches, our analyses found support for the following hypotheses: 1) Numerical modeling shows that migration is linked to zones of higher shear stress, this is already known, but it is only one of the components that triggers migration. 2) There is a high correlation of migration with rapid increase of water levels; the physical interpretation for this finding may be the process of re-configuration the near bank zones flooded and then eroded when the water levels on the river are high. 3) Migration normalized by channel width, NAM , is the most highly correlated with water level variations. For this finding, our explanation is that migration process in the anabranching structure is also related to the magnitude of discharge, since channel width and discharge have some proportional relation, wider channels will have higher capacity of erosion of near bank areas during conditions of high water levels on the river. 4) Sinuosity is not a good parameter to be related to lateral migration on anabranching structures when the points of bifurcation or confluence are migrating constantly, since this parameter would be changing in time without having lateral migration present. Similar analyses of this type need to be done on other anabranching structures to confirm the patterns found in this research. Also numerical modeling may help to understand the importance of unsteady conditions of the flow; such modeling should include morphological evolution, as the bed evolution and lateral migration of the banks.

APPENDIX D

CHRISTIAN FRIAS BIO

D.1 RESEARCH EXPERIENCE

Graduate Research Assistant, Department of Civil and Environmental Engineering, University of Pittsburgh, Pittsburgh, PA, USA, August 2009-Present. As a Graduate Research Assistant my duties involved field data collection (aDcP, GPS surveys, bathymetry surveys) for rivers of multiple scale (from creeks to the Amazon River), construction of experimental flumes and large scale computational fluid dynamics modeling. Also I was in charge of high resolution modeling, such as Large Eddy Simulation for bed morphology and roots systems. As part of my work I had the chance to travel to countries such as Brazil, Peru and inside the USA for field data collection in several environments from deserts to rain forests.

D.2 ACADEMIC TRAINING

- PhD, Expected to graduate: Fall 2013, Department of Civil and Environmental Engineering, University of Pittsburgh, Pittsburgh, PA, USA
- M.Sc., 2011, Department of Civil and Environmental Engineering, University of Pittsburgh, Pittsburgh, PA, USA
- B.Sc. , 2003, Department of Civil Engineering, National University of Engineering, Lima, PERU

D.3 AWARDS

- 2011 Best TA, Department of Civil and Environmental Engineering, University of Pittsburgh
- International Student Fund Scholarship (Center for International Studies of the University of Pittsburgh, 2010) to carry out one-month field measurements in the Amazon River, Peru.

D.4 TEACHING EXPERIENCE

- Teaching Assistant, Fluid Mechanics (Fall 2009, Spring 2012)
- Teaching Assistant, Materials of Construction (Spring 2010, Fall 2010, Spring 2011 Fall 2011)

D.5 MENTORING EXPERIENCE

- 2011: Mentoring of undergraduate student Ross Volkwein in the use of two dimensional numerical models for ripple and pool shear stress characterization. His work won the Best technical paper, undergraduate competition and was presented at The World Environmental & Water Resources Congress, American Society of Civil Engineers, 2011 EWRI-ASCE.
- 2013: Mentoring of undergraduate student Adrian Garcia in the analysis of metrics for the Upper Amazon River Basin. His work was presented as part of the PITT Excel Summer Research Internship Program.
- 2013: Mentoring of the visitor faculty Leo Guerrero in the use of two dimensional numerical models for flood analysis. As part of his scholarship I trained him to use open source code and high performance computing from Feb 2013 to May 2013.

- 2013: FLUENT workshop: I was in charge of a workshop for the Earth Processes & Environmental Flows (EPEF) group on the use of the commercial software FLUENT.

D.6 RESEARCH AND TEACHING INTERESTS

Mechanics of Sediment Transport, River Mechanics and Morphodynamics, River Restoration, Open Channel Flow, Computational Fluid Dynamics, Transport and Mixing , Tropical Rivers, Amazonian Rainforest, High Performance Computing, Probabilistic Risk Assessment, Field and experimental techniques.

D.7 PUBLISHED/IN REVIEW/ IN SUBMISSION/ IN PREPARATION JOURNAL ARTICLES

1. Abad, J. D., Montoro, H., **Frias**, C. E. Anabranching structures in the upper Amazon River, a place for quasi-freely and non-developed meanders. In submission.
2. Mendoza, A. , **Frias**, C. E. , Dauer, K. , Abad, J. D., Paredes, J., Vizcarra, J.. Dynamics of the Amazonian anabranching structure near Iquitos City. In review, Geomorphology.
3. **Frias**, C. E. , Mendoza, A. , Dauer, K. , Abad, J. D., Montoro, H., Paredes, J. Morphodynamic stages of the anabranching in the upper Amazon River basin, in review, Water Resources Research.
4. **Frias**, C. , Abad, J. D. Large Eddy Simulation (LES) for superimposed bedforms in fluvial channels, in press, Water Resources Research
5. Abad, J. D., **Frias**, C., Garcia, M., Buscaglia, G. Modulation of the flow structure by progressive bedforms in the Kinoshita Meandering channel, in press, Earth Surface Processes and Landform.
6. **Frias**, C. E., Abad, J. D., Konsoer, K., Best, J., Rhoads, B., Simon, C., & Langendoen, E. (n.d.). Modulation of the bank shear stress due to bed forms on a field scale. The Wabash River case. In submission.

7. **Frias**, C. E. , Mendoza, A. , Dauer, K. , Abad, J. D., Bed forms dynamics on secondary anabranches of a anabranching river planform. Experiments. In preparation.
8. **Frias**, C. E. , Mendoza, A. , Abad, J. D., Turbulent coherent structures on secondary anabranches of a anabranching river planform. In preparation.
9. **Frias**, C. E., Abad, J. D., Langendoen, E., Modulation of the flow field hydrodynamics by river bank roots. In preparation.
10. **Frias**, C. E., Abad, J. D., Langendoen, E., Sensitivity analysis of single beam surveys resolution for two and three dimensional numerical modeling. In preparation.

D.8 CONFERENCE PROCEEDINGS

1. Langendoen, E., Abad, J., Motta D., **Frias** C., Wong M., Barnes B., Anderson C., Garcia M. Using Predictive Models to Inform River Management and Restoration , in AGU Fall Meeting, San Francisco, CA, USA.
2. **Frias**, C., Mendoza, A., Abad, J. D., Montoro, H., Paredes, J., Vizcarra, J., Dauer, K.(2013) Study of the anabranches dynamics for different sinuosity stages in the Upper Amazon River Basin, in AGU Fall Meeting, San Francisco, CA, USA.
3. Mendoza, A., **Frias**, C., Garcia, A., Abad, J., Vizcarra, J. (2013) Iquitos anabranching structure in the Peruvian Amazon River Bed Morphology Modeling , in International Conference on the Status and Future of the World's Large Rivers, Manaus, Brazil, July 2014.
4. Dauer, K., Abad, J. D., **Frias**, C., Paredes, J., Vizcarra, J., Holguin, C., (2013) Morphodynamics of the Ucayali River, in International Conference on the Status and Future of the World's Large Rivers, Manaus, Brazil, July 2014.
5. **Frias**, C., Garcia, A., Vizcarra, J., Paredes, J. (2013) On the characterization of the anabranching planform metrics of the Upper Amazon River Basin for modeling purposes , in International Conference on the Status and Future of the World's Large Rivers, Manaus, Brazil, July 2014.

6. **Frias**, C., Mendoza, A., Dauer, K., Garcia, A., Abad, J. D. (2013) Bed forms dynamics on secondary anabranches of a anabranching river planform. Experiments, in International Conference on the Status and Future of the World's Large Rivers, Manaus, Brazil, July 2014.
7. **Frias** C., Abad J.D., Montoro H., Paredes J., Holguin C., Vizcarra J. (2013) "On the interaction of flowmorphodynamics of the Upper Amazon anabranching structures", in 35th IAHR world congress, Chengdu, China, September, 2013.
8. **Frias** C., Abad J.D., Montoro H., Paredes J., Holguin C., Vizcarra J. (2013) "Modelling the effect of sinuosity in modern anabranching structures of the Upper Amazon Basin", 10th International Conference on Fluvial Sedimentology, Leeds, UK. July 2013
9. **Frias** C., Abad J.D., Montoro H., Paredes J., Holguin C., Vizcarra J. (2013) "Influence of the main channel sinuosity on the morphodynamics of the Upper Amazon anabranching structures", in 8th Symposium on River, Coastal and Estuarine Morphodynamics (RCEM), Santander, Spain, June, 09-13.
10. **Frias** C., Abad J.D., "On the turbulent flow structure of fluvial bedforms amalgamation processes", in 8th Symposium on River, Coastal and Estuarine Morphodynamics (RCEM), Santander, Spain, June 09-13
11. **Frias**, C., Abad, J. D. (2012). Large Eddy Simulation (LES) of the ripple-dune amalgamation process, implications for free surface and coherent flow structure interactions. Third International Symposium on Shallow Flows, University of Iowa, Iowa City, IA, USA, June 4-6.
12. **Frias**, C., Abad, J. D. (2012). Numerical flow field characterization of the ripple-dune amalgamation process. River Flow 2012, September 5-7, San Jose, Costa Rica.
13. **Frias**, C., Abad, J. D. (2012). Caracterization numerica del campo de flujo en el proceso de amalgamiento rizoduna. XXIV Congreso Latinoamericano de Hidraulica, San Jose, Costa Rica., September 9-12.
14. **Frias**, C., Abad, J. D. (2012). Numerical flow field characterization of the ripple-dune amalgamation process. Computational Methods in Water Resources, June 17-21, Urbana, IL, USA.

15. **Frias**, C., Abad, J. D. (2011). Large Eddy Simulation for superimposed bedforms in fluvial channels. ASCE EWRI conference, Palm Springs, CA, USA, May 22-26.

D.9 ABSTRACTS/TALKS/POSTERS

1. **Frias** C., Abad J.D. (2012). "Turbulence characterization on the ripple dune Amalgamation stage: importance for bed Morphodynamics patterns", in AGU fall meeting, San Francisco, USA. December 2012.
2. **Frias**, C., Abad, J. D. (2011). Turbulence characterization on the ripple-dune amalgamation stage: importance of bed morphodynamic patterns, AGU Fall Meeting, San Francisco, CA, USA.
3. **Frias**, C., and Abad, J. D. (2010). Comparacin de Modelos Numricos de Turbulencia LES. 2nd Congreso Nacional del Agua, National University of Engineering, Lima, PERU, April 7-9. In Spanish.

D.10 TECHNICAL REPORTS

1. **Frias** C., Abad J., Langendoen E. (2013) Progress Report: Numerical Simulation of the Effects of Existing Bank Erosion Control Structures along the Big Sioux River, SD on Stream Morpholog using CONCEPTS
2. **Frias** C., Abad J., Langendoen E. (2012) Technical Note: Topography for the CONCEPTS model, Big Sioux River,SD
3. **Frias** C., Abad J., Langendoen E. (2012) Progress Report: Numerical Simulation to Evaluate the location of Exiting and New Bank Erosion Control Structures in the Big Sioux River, SD
4. Motta D., **Frias** C., Abad J. (2012) Stability analysis and channel-migration simulations of the proposed meandering channel for the Red River Diversion Report to Barr Engineering Co. for the US Army Corps of Engineers

D.11 PROFESSIONAL SOCIETY MEMBERSHIPS

- American Geophysical Union (AGU)
- International Association for Hydraulic Engineering and Research (IAHR) Treasurer of the Pittsburgh Student Chapter 2012-2013 Treasurer of the Lima, Peru Student Chapter 2008-2009

D.12 PROFESSIONAL SERVICE: CONFERENCES

- **(Staff, LOC)**. 2015 River Coastal and Estuarine Morphodynamics (RCEM), Iquitos, Peru. This conference has been previously organized in Italy, Japan, Spain, USA, The Netherlands, and China.
- **(Staff, LOC)**. 2012 Tropical Rivers conference, International conference partially funded by UNESCO and organized by CREAR, August 8-11, Iquitos, Peru.
- **Student Volunteer**, 66th Annual Division of Fluid Dynamics Meeting, American Physical Society, Pittsburgh, PA, November 24-26, 2013.

D.13 PROFESSIONAL SERVICE: WEBSITE ADMINISTRATOR

- www.rvrmeander.org
- www.creamazonia.org
- www.creamazonia.org/tropicalrivers2012
- www.creamazonia.org/rcem2015
- www.creamazonia.org/education/crear-ed-spa

BIBLIOGRAPHY

- [1] *ArcGIS Desktop: Release 10*. ESRI, 2011.
- [2] J. Abad, H. Montoro, C. Frias, J. Paredes, and B. Peralta. The meandering ucayali river, a cyclic adaptation of cutoff and planform migration. *Third International Symposium on Shallow Flows -2012*, 2012.
- [3] J. D. Abad, G. C. Buscaglia, and M. H. Garcia. 2d stream hydrodynamic, sediment transport and bed morphology for engineering applications. *Hydrological Processes*, 22:1443–1459, 2008.
- [4] J. D. Abad and M. H. Garcia. Rvr meander: A toolbox for re-meandering of channelized streams. *Computers and Geosciences*, 32:92–101, 2006.
- [5] J. D. Abad and M. H. Garcia. Experiments in a high-amplitude kinoshita meandering channel. 1: Implications of bend orientation on mean and turbulent flow structure. *Water Resources Research*, 45, 2009.
- [6] J. D. Abad and M. H. Garcia. Experiments in a high-amplitude kinoshita meandering channel. 2: Implications of bend orientation on bed morphodynamics. *Water Resources Research*, 2009.
- [7] J. D. Abad, M. H. Garcia, and G. Parker. Secondary current of saline underflow in a highly meandering channel. part 1. experiments. *In review, Journal of Sedimentary Research*, 2008.
- [8] J. D. Abad, B. L. Rhoads, I. G. G. Guneralp, and M. H. Garcia. Flow structure at different stages in a meander-bend with bendway weir. *Journal of Hydraulic Engineering*, 138(8):1052–1063, 2008.
- [9] J.D. Abad, C.E. Frias, G.C. Buscaglia, and M.H. Garcia. Modulation of the flow structure by progressive bedforms in the kinoshita meandering channel. *Earth Surf. Process. Landforms*, 2013.
- [10] John B. Adams, Donald E. Sabol, Valerie Kapos, Raimundo Almeida Filho, Dar A. Roberts, Milton O. Smith, and Alan R. Gillespie. Classification of multispectral images

- based on fractions of endmembers: Application to land-cover change in the brazilian amazon. *Remote Sensing of Environment*, 52(2):137 – 154, 1995.
- [11] R.J Adrian, C.D. Meinhart, and C.D. Tomkins. Vortex organization in the outer region of the turbulent boundary layer. *Journal of Fluid Mechanics*, 422:1–54, 2000.
- [12] Ronald J. Adrian. Hairpin vortex organization in wall turbulence. *Physics of Fluids*, 19(4), 2007.
- [13] E. Armijos. Cuantificacion de flujos sedimentario de las cuencas amazonicas de peru. master’s thesis, Universidad Nacional Agraria La Molina, 2010.
- [14] B.J. Armitage and E.T. Rankin. An assessment of threats to the biological condition of the wabash river aquatic ecosystem of indiana. Technical report, The Nature Conservancy, Indiana Chapter, 2010.
- [15] Masahito Asai, Masayuki Minagawa, and Michio Nishioka. The instability and breakdown of a near-wall low-speed streak. *Journal of Fluid Mechanics*, 455:289–314, 2002.
- [16] P. E. Ashmore. How do gravel-bed rivers braid? *Canadian Journal of Earth Sciences*, 28:326–341, 1991.
- [17] P. E. Ashmore. Anabranch confluence kinetics and sedimentation processes in gravel-braided streams. In *Best and Bristow*, pages 129–146. 1993.
- [18] Phil Ashworth, Sean Benett, James Best, and Stuart McLelland. *Coherent Flow Structures in Open Channels*. John Wiley & Sons, 1996.
- [19] Philip J. Ashworth and John Lewin. How do big rivers come to be different? *Earth-Science Reviews*, 114:84–107, 2012.
- [20] David B. Baker, R. Peter Richards, Timothy T. Loftus, and Jack W. Kramer. A new flashiness index: Characteristics and applications to midwestern rivers and streams1. *JAWRA Journal of the American Water Resources Association*, 40(2):503–522, 2004.
- [21] S. J. Bennett and J. L. Best. Mean flow and turbulence structure over fixed ripples and the ripple-dune transition. In *Coherent Flow Structures in Open Channels*, edited by P. J. Ashworth, p. J. Bennett, J. L. Best and S. J. McLelland. Wiley, Chichester, pages 281–304, 1996.
- [22] J. Best. The fluid dynamics of river dunes: A review and some future research directions. *Journal of Geophysical Research*, 110:F04S02, 2005.
- [23] J. Best. Kinematics, topology and significance of dune-related macroturbulence: some observations from laboratory and field. In *Fluvial Sedimentology VII*, edited by M. D. Blum, S. B. Marriot and S. F. Leclair, 2005.

- [24] Jim Best. The fluid dynamics of river dunes: A review and some future research directions. *Journal of Geophysical Research*, 110, 2005.
- [25] G. Binder, S.Tardu, R.F. Blackwelder, M.Q Feng, and R.D Maestri. Unsteady turbulent flows in channels with parallel or diverging walls. Technical report, European Research Office of the U.S. Army, 1991.
- [26] C. M. Birkett, L. A. K. Mertes, T. Dunne, M. H. Costa, and M. J. Jasinski. Surface water dynamics in the amazon basin: Application of satellite radar altimetry. *Journal of Geophysical Research: Atmospheres*, 107(D20):LBA 26–1–LBA 26–21, 2002.
- [27] J. C. Blodgett and C. E. McConaughy. Rock riprap design for protection of stream channels near highway structures: Volume 2 – evaluation of riprap design procedures. Technical report, United States. Federal Highway Administration, 1986.
- [28] J. Bouchez, M. Lupker, J. Gaillardet, C. France-Lanord, and L. Maurice. Prediction of depth-integrated fluxes of suspended sediment in the amazon river: particle aggregation is a complicating factor. *Hydrological Processes*, 25(5):778–794, 2011.
- [29] K. F. Bradbrook, S. N. Lane, K. S. Richards, P. M. Biron, and A. G. Roy. Large eddy simulation of periodic flow characteristics at river channel confluences. *Journal of Hydraulic Research*, 38(3):207–215, October 2000.
- [30] K. S. Brown. Species diversity and abundance in jaru, rondonia, brasil. *News of the lepidopterists Society*, (3):45–47, 1984.
- [31] Mariano I. Cantero, S. Balachandar, and Marcelo H. Garcia. An eulerian-eulerian model for gravity currents driven by inertial particles. *International Journal of Multiphase Flow*, 2008.
- [32] Carling, Gözl, Orr, and Radecki-Pawlik. The morphodynamics of fluvial sand dunes in the River Rhine, near Mainz, Germany. I. Sedimentology and morphology. *Journal of Hydraulic Research*, 47(1):227–252, February 2000.
- [33] P.A. Carling, E. Gözl, Orr, and Radecki-Pawlik. The morphodynamics of fluvial sand dunes in the River Rhine, near Mainz, Germany. II. Hydrodynamics and sediment transport. *Journal of Hydraulic Research*, 47(1):253–278, February 2000.
- [34] D.S. Carneiro. Morfodinâmica fluvial do rio solimões, trecho tabatinga a benjamin constant am e suas implicações para o ordenamento territorial. master’s thesis, Universidade Federal Fluminense, 2009.
- [35] J. Carranza-Valle. Boletín extraordinario de la evaluación hidrológica y pluviométrica en la cuenca amazónica peruana. Technical report, IRD-Senamhi, Lima, Peru, 2012. <http://www.senamhi.gob.pe/>.

- [36] Matthieu J.B. Cartigny, Dario Ventra, George Postma, and Jan H. van den Berg. Morphodynamics and sedimentary structures of bedforms under supercritical-flow conditions: New insights from flume experiments. *Sedimentology*, pages n/a–n/a, 2013.
- [37] Alberto Carvalho. *Terras cadas e conseqncias sociais: Costa do Miracauera Paran da Trindade, Municipio de Itacoatiara*. PhD thesis, Universidade Federal do Amazonas, 2006.
- [38] Y.A. Catano-Lopera, J. D. Abad, and M. H. Garcia. Characterization of bedform morphology generated under combined flows and currents using wavelet analysis. *Ocean Engineering*, In press., 2009.
- [39] Yeon S. Chang and Alberto Scotti. Modeling unsteady turbulent flows over ripples: Reynolds-averaged navier-stokes equations (rans) versus large-eddy simulation (les). *Journal of Geophysical Research: Oceans*, 109(C9):n/a–n/a, 2004.
- [40] Yi-Ju Chou and Oliver B. Fringer. A model for the simulation of coupled flow bed form evolution in turbulent flows. *Journal of Geophysical Research*, 115, 2010.
- [41] C.C. Christensen. Indiana fixed station statistical analysis 1997. Technical report, Indiana Department of Environmental Management, Office of Water Management, Assessment Branch, Surveys Section, 1998.
- [42] S. Coleman and B.W. Melville. Initiation of bed forms on a flat sand bed. *Journal of Hydraulic Engineering*, 122(6):301–310, 1996.
- [43] Canadian Hydraulics Centre National Research Council. Preparation of a hydrodynamic model of st. clair river with telemac-2d to study the impacts of potential changes to the waterways. Technical report, Canadian Hydraulics Centre National Research Council, 2009.
- [44] Canadian Hydraulics Centre National Research Council. Preparation of a two-dimensional hydrodynamic model of the lower pembina river flood plains. Technical report, Canadian Hydraulics Centre National Research Council, 2009.
- [45] Canadian Hydraulics Centre National Research Council. Rainy river 2d hydrodynamic modelling study - phase ii. Technical report, Canadian Hydraulics Centre National Research Council, 2011.
- [46] K.S. Cummings, C.A. Mayer, and L.M. Page. Survey of the freshwater mussels (mollusca: Unionidae) of the wabash river drainage. phase ii: Upper and middle wabash river. Technical report, Indiana Department of Natural Resources Division of Fish and Wildlife, 1988.
- [47] Eugene de Villiers. *The Potential of Large Eddy Simulation for the Modeling of Wall Bounded Flows*. PhD thesis, Imperial College of Science, Technology and Medicine, 2006.

- [48] DGAS. *Hacia una gestión integrada de los recursos hídricos en el Perú*. Ministerio de Agricultura, Perú, 1995.
- [49] DHI. Mike 21c river morphology - a short description. Technical report, Danish Hydraulic Institute (DHI) Water and Environment, 2004.
- [50] DHN-SHNA. Monitoreo hidrográfico del río Amazonas entre las localidades de Tamshiyacu y Sinchicuy Iquitos y cercanías. Technical report, Dirección de Hidrografía y Navegación Servicio de Hidrografía y Navegación de la Amazonía, 2011.
- [51] DHN-SHNA. Levantamiento hidrográfico del área de frontera tripartita peruano-colombo-brasileño en el río Amazonas. Technical report, Dirección de Hidrografía y Navegación Servicio de Hidrografía y Navegación de la Amazonía, 2012.
- [52] R. L. Dinehart and J. R. Burau. Averaged indicators of secondary flow in repeated acoustic doppler current profiler crossing of bends. *Water Resources Research*, 41, 2005.
- [53] T. Dunne, L.A.K. Mertes, R.H. Meade, J. E. Richey, and B. R. Frosberg. Exchanges of sediment between the flood plain and channel of the Amazon river in Brazil. *GSA Bulletin*, 110:450–467, 1998.
- [54] EDF-DRD. *TELEMAC-2D Validation Document*. EDF-DRD, 2000.
- [55] EDF-DRD. *2D hydrodynamics TELEMAC-2D software Version 6.0 USER MANUAL*. EDF-DRD, 2010.
- [56] H. A. Einstein. The bed load function for sediment transportation in open channel flows. *U.S. Department of Agriculture, Soil and Conservation Service, Washington, D.C.*, 1950.
- [57] F. Engelund and J. Fredsøe. Transition from dunes to plane bed in alluvial channels. *Inst. of Hydrodyn. and Hydraul. Eng., Tech. Univ. of Den., Lyngby*, Ser. Pap. 4, 1974.
- [58] F. Engelund and J. Fredsøe. Sediment ripples and dunes. *Annual Review of Fluid Mechanics*, 14(1):13–37, 1982.
- [59] F. Engelund and E. Hansen. A monograph on sediment transport in alluvial streams. *Copenhagen: Danish Technical Press*, 1967.
- [60] Christian Escarriaza. *Three-dimensional Unsteady Modeling of Clear-Water Scour in the Vicinity of Hydraulic Structures: Lagrangian and Eulerian Perspectives*. PhD thesis, University of Minnesota, 2008.
- [61] Cristian Escarriaza and Fotis Sotiropoulos. Initial stages of erosion and bed form development in a turbulent flow around a cylindrical pier. *Journal of Geophysical Research*, 116, 2011.

- [62] J.H. Espinoza, Ronchail J., W. Lavado, W. Santini, P. Vauchel, R. Pomposa, M. Villacis, R. Carranza, J. Junquas, G. Drapeau, and J. Louguyot. Recent droughts in the peruvian amazonas basin: Climate origins and hydrological impacts. *Revista Peruana Geo-Atmosferica RPGA*, 3:63–72, 2011. www.senamhi.gob.pe/rpga.
- [63] J. J. Fedele and M. H. Garcia. *River, Coastal and Estuarine Morphodynamics*, chapter Alluvial roughness in steams with dunes: A boundary-layer approach, pages 37–60. Springer, New York, 2001.
- [64] R.I. Ferguson and D.R. Parsons. Flow in meander bends with recirculation at the inner bank. *Water Resour. Res.*, 39(11):1322, doi:10.1029/2003WR001965, 2003.
- [65] R. Fernandez, J. Best, and F. Lopez. Mean flow, turbulence structure and bedform superimposition across the ripple-dune transition. *Water Resources Research*, (42):948–963, 2006.
- [66] Rocio L. Fernandez. Caracterizacion de procesos turbulentos intervinientes en la transicion rizo-duna por amalgamiento. Master’s thesis, Universidad Nacional de Cordoba, 2001.
- [67] N. Filizola and J.L. Guyot. The use of doppler technology for suspended sediment discharge determinations in the river amazon. *Hydrological Sciences Journal*, 49(1):143–153, 2004.
- [68] B.E. Fisher. Current status of freshwater mussels (order unionoida) in the wabash river drainage of indiana. volume 115(2), pages 103–109, 2006. Indiana Academy of Science.
- [69] OpenFOAM Foundation. *OpenFOAM The OpenSource CFD Toolbox - User Guide*. OpenFOAM Foundation, 2011.
- [70] Elena Franzinelli and Paul Edwin Potter. Petrology, chemistry, and texture of modern river sands, amazon river system. *The Journal of Geology*, 91(1):23–29, 1983.
- [71] Christian Frias, Jorge Abad, Kory Konsoer, James Best, Bruce Rhoads, Cesar Simon, and Eddy Langendoen. Modulation of the bank shear stress due to bed forms on a field scale. the wabash river case. *In submission, Water Resources Research*, 2013.
- [72] Christian Frias, Alejandro Mendoza, Jorge Paredes, Kristin Dauer, Jorge Abad, and Hugo Montoro. Morphodynamic stages of the anabranches in the upper amazon river basin. *In review, Water Resources Research*, 2013.
- [73] Christian E. Frias and Jorge D. Abad. Mean and turbulent flow structure during the amalgamation process in fluvial bed forms. *Water Resources Research*, pages n/a–n/a, 2013.
- [74] P. F. Friend and R. Sinha. Braiding and meandering parameters. In *Braided Rivers*, volume 75, pages 105–111, 1993. Geological Society, London, Special Publication.

- [75] J. Fröhlich, C. P. Mellen, W. Rodi, L. Temmerman, and M.A. Leschziner. Highly-resolved large eddy simulation of separated flow in a channel with streamwise periodic constrictions. *Journal of Fluid Mechanics*, (526):19–66, 2005.
- [76] Sharon L. Gabel. Geometry and kinematics of dunes during steady and unsteady flows in the Calamus River, Nebraska, USA. *Journal of Sedimentology*, 40:237–269, 1993.
- [77] Joaquin Garcia and Nicole Bernex. *El rio que se aleja*. CETA-IIAP, 1994.
- [78] Joaquin Garcia and Nicole Bernex. *The Wabash River Ecosystem*. Cinergy Corporation, Eli Lilly and Company and DePauw University, 1998.
- [79] M. H. Garcia. Sediment transport and morphodynamics. *Chapter 2 in ASCE Manual of Practice 110. In Sedimentation Engineering: Processes, Measurements, Modelling and Practice. Edited by M. H. Garcia, ASCE, Reston, Va., 2008.*
- [80] Adrian Gaston. Analysis and identification of vortices within a turbulent channel boundary layer flow. Master’s thesis, Texas A&M University, 2005.
- [81] E. Gautier, D. Brunstein, P. Vauchel, J.M. Jouanneau, M. Roulet, C. Garcia Govea, J.L. Guyot, and M. Castro. Channel and floodplain sediment dynamics in a reach of the tropical meandering rio beni (bolivian amazonia). *Earth Surface Processes and Landforms*, 35(15):1838–1853, 2010.
- [82] A.H. Gentry. Tree species richness of upper amazonian forests. *Proceeding National Academy Sciences*, (85):156–159, 1988.
- [83] S. Giri and Y. Shimizu. Numerical computation of sand dune migration with free surface flow. *Water Resources Research*, 42, 2006.
- [84] A.J. Grass. Structural features of turbulent flow over smooth and rough boundaries. *Journal of Fluid Mechanics*, 50:233–255, 1971.
- [85] D. G. E. Grigoriadis, E. Balaras, and A. A. Dimas. Large-eddy simulations of unidirectional water flow over dunes. *Journal of Geophysical Research*, 114, 2009.
- [86] R. R. Gutierrez, J. D. Abad, D. R. Parsons, and J. L. Best. Discrimination of bed form scales using robust spline filters and wavelet transforms: methods and application to synthetic signals and bed forms of the rio parana, argentina. *Journal of Geophysical Research*, In press., 2013.
- [87] Ronald R. Gutierrez, Jorge D. Abad, Daniel R. Parsons, and James L. Best. Discrimination of bed form scales using robust spline filters and wavelet transforms: Methods and application to synthetic signals and bed forms of the ro paran, argentina. *Journal of Geophysical Research: Earth Surface*, pages n/a–n/a, 2013.
- [88] A. Gyr and K. Hoyer. *Sediment Transport*. Springer, 2006.

- [89] Robert Haimes and David Kenwright. On the velocity gradient tensor fluid feature extraction. Technical report, America Institute of Aeronautics and Astronautics, 1999.
- [90] Carlos Hartel and Leonhard Kleiser. Analysis and modelling of subgrid-scale motions in near-wall turbulence. *Journal of Fluid Mechanics*, 1998.
- [91] John Hertz, Anders Krogh, and Richard G. Palmer. *Introduction to the theory of neural computation*. Addison-Wesley Longman Publishing Co., Inc., Boston, MA, USA, 1991.
- [92] J. M. Hervouet. *Hydrodynamics of free surface flows, modelling with the finite element method*. Wiley Press, 2007.
- [93] M.A. Holdeman, S.C. Gibson, and C.C. Christensen. Trend analysis of fixed station water quality monitoring data in the upper wabash river basin 1998. Technical report, Indiana Department of Environmental Management, Office of Water Management, Assessment Branch, Indianapolis, Indiana, 1998.
- [94] Alan D. Howard, Mary E. Keetch, and C. Linwood Vincent. Topological and geometrical properties of braided streams. *Water Resources Research*, 6(6):1674–1688, 1970.
- [95] He Qing Huang and Gerald Nanson. Why some alluvial rivers develop an anbranching pattern. *Water Resources Research*, 43, 2007.
- [96] S. Ikeda, G. Parker, and K. Sawai. Bend theory of river meanders. part 1. linear development. *Journal of Fluid Mechanics*, 112:363–377, 1981.
- [97] INEI. Boletín de análisis demográfico no.36 “perú: Estimaciones y proyecciones de població’ 1950-2050’”. Technical report, INEI, Lima, Peru, 2009.
- [98] R. G. Jackson. Velocity-bed-form-texture patterns of meander bends in the lower wabash river of illinois and indiana. *Geological Society of America Bulletin*, 86:1511–1522, 1975.
- [99] R. G. Jackson. Depositional model of point bars in the lower wabash river. *Journal of Sedimentary Petrology*, 46(3):579–594, 1976.
- [100] Hendrik Reinhard Albert Jagers. Modelling planform changes of braided rivers, 2003.
- [101] Vikrant Jain and R. Sinha. Fluvial dynamics of an anabranching river system in himalayan foreland basin, baghmata river, north bihar plains, india. *Geomorphology*, 60:147–170, 2004.
- [102] C. L. Jang and Y. Shimizu. Numerical simulation of relatively wide, shallow channel with erodible banks. *Journal of Hydraulic Engineering*, 131(7):565–575, 2005.
- [103] John D. Jansen and Gerald C. Nanson. Anabranching and maximum flow efficiency in magela creek, northern australia. *Water Resources Research*, 40, 2004.

- [104] John D. Jansen and Gerald C. Nanson. Functional relationships between vegetation, channel morphology and flow efficiency in an alluvial (anabranching) river. *Journal of Geophysical Research*, 115, 2010.
- [105] D. Jerolmack. Conditions for branching in depositional rivers. *The Geological Society of America*, 35:463–466, 2007.
- [106] D. Jerolmack and D. Mohrig. Interactions between bed forms: Topography, turbulence, and transport. *Journal of Geophysical Research*, 110, 2005.
- [107] H. Johannesson and G. Parker. Linear theory of river meanders. *River Meandering. Edited by Syunsuke Ikeda and Gary Parker. Water Resources Monograph - American Geophysical Union.*, pages 181–213, 1989.
- [108] Jason W. Kean and J. Dungan Smith. Form drag in rivers due to small-scale natural topographic features: 2. irregular sequences. *Journal of Geophysical Research: Earth Surface*, 111(F4):n/a–n/a, 2006.
- [109] J. F. Kennedy. The formation of sediment ripples, dunes and antidunes. *Annu. Rev. Fluid Mech.*, 1:147–168, 1963.
- [110] C.J. Keylock, R.J. Hardy, D.R. Parsons, R.I. Ferguson, S.N. Lane, and K.S. Richards. The theoretical foundations and potential for large-eddy simulation (LES) in fluvial geomorphic and sedimentological research. *Earth-Science Reviews*, 71:271–304, August 2005.
- [111] Gerhard Klammer. The relief of the extra-andean amazon basin. In Harald Sioli, editor, *The Amazon*, volume 56 of *Monographiae Biologicae*, pages 47–83. Springer Netherlands, 1984.
- [112] W. C KRUMBEIN and ANTONY R ORME. Field mapping and computer simulation of braided-stream networks. *Geological Society of America Bulletin*, 83(11):3369–3380, 1972.
- [113] S. T. Lancaster. *A Nonlinear River Meandering Model and its Incorporation in a Landscape Evolution Model*. PhD thesis, Massachusetts Institute of Technology, September 1998.
- [114] E. J. Langendoen and C. V. Alonso. Modeling the evolution of incised streams. i: model formulation and validation of flow and streambed evolution components. *Journal of Hydraulic Engineering*, 134(6):749–762, 2008.
- [115] E. J. Langendoen and A. Simon. Modeling the evolution of incised streams. ii: stream-bank erosion. *Journal of Hydraulic Engineering*, 134(7):905–915, 2008.
- [116] E. J. Langendoen, R. R. Wells, R. E. Thomas, A. Simon, and R. L. Bingner. Modeling the evolution of incised streams. iii: model application. *Journal of Hydraulic Engineering*, 2008.

- [117] A. Laraque, I. Bernal, L. Bourrel, J. Darrozes, F. Christophoul, N. Armijos, P. Fraizy, R. Pombosa, and J.L. Guyot. Sediment budget of the napo river, amazon basin, ecuador and peru. *Hydrological Processes*, 23(25):3509–3524, 2009.
- [118] E. Latrubesse. Patterns of anabranching channels: The ultimate end-member adjustment of mega rivers. *Geomorphology*, 101:130–145, 2008.
- [119] Wesley Lauer. *NCED Stream Restoration Toolbox - Channel Planform Statistics And ArcMap Project*. National Center for Earth-Surface Dynamics (NCED), 2006.
- [120] C.W. Li and J.H. Wang. Large eddy simulation of dispersion in free surface shear flow. *Journal of Hydraulic Research*, 40(3):351–358, October 2002.
- [121] T.S. Luchik and W.G. Tiederman. Timescale and structure of ejections and bursts in turbulent channel flows. *Journal of Fluid Mechanics*, 174:529–552, 1987.
- [122] R. McDuffee. An assessment of pesticides in the lower wabash river basin and kankakee river basin. Technical report, Indiana Department of Environmental Management, Office of Water Quality, Assessment Branch, Surveys Section, Indianapolis, Indiana, 2002.
- [123] L. McFall, S. Martin, and C. Christensen. 1998. upper wabash river basin sampling sites and stream standard violations. Technical report, Indiana Department of Environmental Management, Office of Water Management, Assessment Branch, Indianapolis, Indiana, 2000.
- [124] Alejandro Mendoza, Christian Frias, Jorge Abad, Jorge Paredes, Kristin Dauer, and Jorge Vizcarra. Planform dynamics of iquitos anabranching structure on the amazon river. *In review, Geomorphology*, 2013.
- [125] F.R. Menter. Zonal two equation k- turbulence models for aerodynamic flows. *AIAA 24th Fluid Dynamics Conference*, 1993.
- [126] Leal A.K. Mertes and Thomas Dunne. *Large Rivers: Geomorphology and Management*, chapter Effects of Tectonism, Climate Change, and Sea-level Change on the Form and Behaviour of the Modern Amazon River and its Floodplain. Wiley, 2008.
- [127] Leal A.K. Mertes, Thomas Dunne, and Luiz A. Martinelli. Channel-floodplain geomorphology along the solimões-amazon river, brazil. *GSA Bulletin*, 108(9):1089–1107, 1996.
- [128] Leal A.K. Mertes and Robert H. Meade. Particle sizes of sands collected from the bed of the amazon river and its tributaries in brazil during 1982-1984. Technical report, U.S. Geological Survey, 1985.
- [129] Liubov V Meshkova and Paul A Carling. Discrimination of alluvial and mixed bedrockalluvial multichannel river networks. *Earth Surface Processes and Landforms*, 38(11):1299–1316, 2013.

- [130] Meredith Metzger, Berveley McKeon, and Enrique Arce-Larreta. Scaling the characteristic time of the bursting process in the turbulent boundary layer. *Physica D*, 239:1296–1304, 2010.
- [131] D. Motta, J. D. Abad, E. J. Langendoen, and M. H. Garcia. A simplified 2d model for meander migration with physically-based bank evolution. *Geomorphology*, 163:10–25, 2012.
- [132] D. Motta, E. J. Langendoen, J. D. Abad, and M. H. Garcia. Modification of meander migration by bank failures. *Journal of Geophysical Research*, 2013.
- [133] Charles Moulinec, Christophe Denis, C.-T. Pham, D. Rougé, Jean-Michel Hervouët, Emile Razafindrakoto, W. Barber, R., R. Emerson, D., and J. Gu, X. TELEMAC: An efficient hydrodynamics suite for massively parallel architectures. *Computers and Fluids*, 51(1):30–34, 2011.
- [134] Brad Murray and Chris Paola. A cellular model of braided rivers. *Letters to Nature*, 371(1), 1994.
- [135] Gerald C. Nanson and A. David Knighton. Anabranching rivers: their cause, character and classification. *Earth Surface Processes and Landforms*, 21:217–239, 1996.
- [136] J. M. Nelson, B. L. Logan, P. J. Kinzel, Y. Shimizu, S. Giri, R. L. Shreve, and S. R. McLean. Bedform response to flow variability. *Earth Surface Processes and Landforms*, 36(14):1938–1947, 2011.
- [137] Jonathan M. Nelson, Stephen R. McLean, and Stephen R. Wolfe. Mean flow and turbulence fields over two-dimensional bed forms. *Water Resources Research*, 29(12):3935–3953, 1993.
- [138] I. Nezu and H. Nakagawa. Turbulence in open channel flows. *IAHR, Balkema, Rotterdam, The Netherlands*, 1993.
- [139] Andrew Nicholas. Morphodynamic diversity of the worlds largest rivers. *Geology*, 41(4), 2013.
- [140] Andrew P. Nicholas, Steven D. Sandbach, Philip J. Ashworth, Mario L. Amsler, James L. Best, Richard J. Hardy, Stuart N. Lane, Oscar Orfeo, Daniel R. Parsons, Arnold J.H. Reesink, Gregory H. Sambrook Smith, and Ricardo N. Szupiany. Modelling hydrodynamics in the rio parana, argentina: An evaluation and inter-comparison of reduced-complexity and physics based models applied to alarge sand-bed river. *Geomorphology*, 169-170:192–211, 2012.
- [141] OpenFOAM-Foundation. *OpenFOAM, The Open Source CFD Toolbox User Guide*. OpenFOAM Foundation, 2012.
- [142] C. Paola and L. Borgman. Reconstructing topography from preserved stratification. *Journal of Sedimentology*, 38:553–565, 1991.

- [143] Chris Paola. Incoherent structure: turbulence as a metaphor for stream braiding. In *Coherent Flow Structures in Open Channels*, pages 705–723.
- [144] D. R. Parsons, J. L. Best, O. Orfeo, R. J. Hardy, R. Kostaschuk, and S. N. Lane. Morphology and flow fields of three-dimensional dunes, Rio Parana, Argentina: Results from simultaneous multibeam echo sounding and acoustic Doppler current profiling. *Journal of Geophysical Research*, 110, 2005.
- [145] Stephen B. Pope. *Turbulent Flows*. Cambridge University Press, 2000.
- [146] A. H. Rachoeki. *Alluvial Fans, An attempt at an empirical approach*. John Wiley & Sons, 1981.
- [147] C.G. Ramonell, M.L. Amsler, and H. Tonolio. Shifting modes of the parana river thalweg in its middle-lower reaches. *Zeitschrift fur Geomorphologie*, 129:129–142, 2002.
- [148] A.J. Raudkivi. *Loose Boundary Hydraulics*. Balkema, 1998.
- [149] EDF R&D. *Telemac modelling system: 2D hydrodynamics TELEMAC-2D software Version 6.0*. Laboratoire National D’Hydraulique Et Environnement, 2010.
- [150] R. E. Ricklefs. Community diversity: relative roles of local and regional processes. *Science*, (235(4785)):167–171, 1987.
- [151] J.F. Rodriguez, F.A. Bombardelli, M.H. Garcia, K. Frothingham, B.L. Rhoads, and J.D. Abad. High-resolution numerical simulation of flow through a highly sinuous river reach. *Water Resources Management*, 18:177–199, 2004.
- [152] Jos ’e Max González Roza and Carlomagno Soto Castro. Multitemporal analysis of the amazon river between corea island (colombia) and aramosa island (brazil). *Ingeniera Investigacin y Desarrollo*, 9(2):13–17, 2009.
- [153] Jim Ruppert. A delaunay refinement algorithm for quality 2-dimensional mesh generation. *Journal of Algorithms*, 18:548–585, 1995.
- [154] Yasuhiko Saka, Kouji Nagata, and Hiroki Suzuki. *Wind Tunnels and Experimental Fluid Dynamics Research*, chapter 24 - Relationships between Large-Scale Coherent Motions and bursting Events in a Turbulent Boundary Layer. InTech, 2011.
- [155] S. D. Sandbach, S. N. Lane, R. J. Hardy, M. L. Amsler, P. J. Ashworth, J. L. Best, A. P. Nicholas, O. Orfeo, D. R. Parsons, A. J. H. Reesink, and R. N. Szupiany. Application of a roughness-length representation to parameterize energy loss in 3-d numerical simulations of large rivers. *Water Resour. Res.*, 48, 2012.
- [156] W. Santini, J.M. Martinez, R. Espinoza Villar, J.C. Espinoza Villar, R. Huanaquiri, and W. Arimuya. Pe-83 iquitos informe de comisi3n. Technical report, Institut de recherche pour le d3veloppement - HYBAM, 2011.

- [157] W. Santini, A. Villacorta, R. Huanquiri, and Arimuya W. Pe-84 iquitos informe de comisi3n. Technical report, Institut de recherche pour le d3veloppement - HYBAM, 2012.
- [158] S. A. Schumm. Patterns of alluvial rivers. *Ann. Rev. Earth Planet Sci.*, 13:5–27, 1985.
- [159] G. Seminara. Meanders. *Journal of Fluid Mechanics*, 554:271–297, 2006.
- [160] Dan. H. Shugar, Ray Kostaschuk, James L. Best, Daniel R. Parsons, Stuart N. Lanes, Oscar Orfeo, and Richard J. Hardy. On the relationship between flow and suspended sediment transport over the crest of a sand dune, ro paran, argentina. *Sedimentology*, 57:252–272, 2010.
- [161] C. R. Smith and S.P. Meltzer. The characteristics of low-speed streaks in the near-wall region of a turbulent boundary layer. *Journal of Fluid Mechanics*, 129:27–54, 1983.
- [162] T.C. Stefanavage. Summary of harvest estimates and license sales for indianas inland river commercial fisheries, 2007. fish management report. Technical report, Fisheries Management Section, Indiana Department of Natural Resources, Division of Fish and Wildlife, 2009.
- [163] T. Stoesser, M.ASCE, C. Braun, M. Garc3a-Villalba, , W. Rodi, and M.ASCE. Turbulence structures in flow over two-dimensional dunes. *Journal of Hydraulic Engineering*, 134(1), January 2008.
- [164] T. A. Stone and P. Lefebvre. Using multi-temporal satellite data to evaluate selective logging in para, brazil. *Int. J. Remote Sensing*, 19(13):2517–2526, 1998.
- [165] Alexander N. Sukhodolov, Juan J. Fedele, and Bruce Rhoads. Structure of flow over alluvial bedforms: an experiment on linking field and laboratory methods. *Earth Surface Processes and Landforms*, 31:1292–1310, 2006.
- [166] R. Szupiany, M. Amsler, J. Best, and D. Parsons. Comparison of fixed- and moving-vessel flow measurements with an adcp in a large river. *Journal of Hydraulic Engineering*, 133(12):1299–1309, 2007.
- [167] Chris Paola Tao Sun and Gary Parker. Fluvial fan deltas: Linking channel processes with large-scale morphodynamics. *Water Resources Research*, 38(8), 2002.
- [168] J. Terborgh. *Five new world primates. A study in comparative ecology*. Princeton University Press, 1983.
- [169] R. Thomas, A.P. Nicholas, and T.A. Quine. Cellular modelling as a tool for interpreting historic braided river evolution. *Geomorphology*, 90:302–317, 2007.
- [170] C.R Thorne. *Processes and mechanisms of river bank erosion*, chapter Gravel-bed Rivers, pages 227–271. Wiley, 1982.

- [171] M.J. Van de Wiel T.J. Coulthard, D.M Hicks. Cellular modelling of river catchments and reaches: Advantages limitations and prospects. *Geomorphology*, 90:192–207, 2007.
- [172] Jean L.F. Tricart. Types de lit fluviaux en amazonie brsilienne. *Annales de Gographie*, 86(473):1–54, 1977.
- [173] E. Tuukki, P. Jokien, and R. Kalliola. Migraciones en el río amazonas en las últimas décadas, sector confluencia ríos marañon - isla de iquitos. *Folia Amazonica*, 8(1):111–130, 1996.
- [174] W. M. van Dijk, W. I. van de Lageweg, and M. G. Kleinhans. Experimental meandering river with chute cutoffs. *Journal of Geophysical Research: Earth Surface*, 117(F3):n/a–n/a, 2012.
- [175] van Rijn. Sediment transport, part i. bed load transport. *Journal of Hydraulic Engineering*, 110(10):1431–1455, 1984.
- [176] van Rijn. Unified view of sediment transport by currents and waves. i: Initiation of motion, bed roughness, and bed-load transport. *Journal of Hydraulic Engineering*, 133(6):649–667, 2007.
- [177] J.G. Venditti. Turbulent flow and drag over fixed two- and three-dimensional dunes. *Journal of Geophysical Research*, 112, 2007.
- [178] J.G. Venditti and S. J. Bennett. Spectral analysis of turbulent flow and suspended sediment transport over fixed dunes. *Journal of Geophysical Research*, 105:22035–22048, 2000.
- [179] J.G. Venditti, M. Church, and S. J. Bennett. On interfacial instability as a cause of transversal subcritical bed forms. *Water Resources Research*, 42, 2006.
- [180] J.G. Venditti and M. A. Church. Bed form initiation from a flat sand bed. *Journal of Geophysical Research*, 110:1–19, 2005.
- [181] D. C. Wilcox. *Turbulence Modeling for CFD*. DCW Industries Inc., La Cañada, CA, 1993.
- [182] H. Wittmann, F. Von Blanckenburg, L. Maurice, J.L. Guyot, N. Filizola, and P Kubik. Sediment production and delivery in the amazon river basin quantified by in situ produced cosmogenic nuclides and recent river loads. *Geological Society of America Bulletin*, 123((5-6)):934–950, 2011.
- [183] Anna L. Wood. *A geomorphological analysis of bank toe processes : the fate of failed blocks stored in the basal zone of incised channels*. PhD thesis, University of Nottingham, 2001.
- [184] S. Wright and G. Parker. Flow resistance and suspended load in sand-bed rivers: Simplified stratification model. *Journal of Hydraulic Engineering*, 130(8):796–805, 2004.

- [185] M.S Yalin. Geometrical properties of sand waves. *J. Hydraulic Div. am.Soc. Civ. Eng*, 90:105–109, 1964.
- [186] W. Yue, C-L Lin, and V. C. Patel. Coherent structures in open-channel flows over a fixed dune. *Journal of Fluid Engineering*, 127:858–864, 2005.
- [187] Wusi Yue, Ching-Long Lin, Virendra C. Partel, and M. ASCE. Large-eddy simulation of turbulent flow over a fixed two-dimensional dune. *Journal of Hydraulic Engineering*, 110, July 2006.
- [188] Wusi Yue, Ching-Long Lin, and Virendra C. Patel. Large eddy simulation of turbulent open-channel flow with free surface simulated by level set method. *Physics of Fluids*, 17, 2005.
- [189] J.A. Zinger, B.L. Rhoads, and J.L. Best. Extreme sediment pulses generated by bend cutoffs along a large meandering river. *Nature Geosci.*, 4(6):675–678, 2011.
- [190] G. Zolezzi and G. Seminara. Downstream and upstream influence in river meandering. part 1. general theory and application to overdeepening. *Journal of Fluid Mechanics*, 438:183–211, 2001.